University of Szeged

Faculty of Pharmacy

Doctoral School of Pharmaceutical Sciences

Institute of Pharmaceutical Analysis

Bioanalytical Applications of LC-MS Techniques

Ph.D. thesis

Zahraa Ali

Supervisor:

Dr. Róbert Berkecz

Szeged, Hungary

2026

Publications related to the subject of the thesis

This thesis is based on the following publications:

I. **Ali, Z.,** Frank, R., Körmöczi, T., Ilisz, I., Domoki, F., Weicznere, R., Bari, F., Farkas, E., Berkecz, R., (2024). UHPLC-MS/MS approach for following nimodipine saturation kinetics in acute rat brain slice. **Journal of analysis and testing** 8, 466–477 *https://doi.org/10.1007/s41664-024-00316-z*

IF 7.0 (D1)

II. Körmöczi, T., Barta, A., Bogár, F., **Ali, Z**., Bús, C., Hohmann, J., Domoki, F., Ilisz, I., Weiczner, R., Vasas, A., & Berkecz, R. (2025). Study of phenanthrenes from their unique mass spectrometric behavior through quantum chemical calculations to liquid chromatographic quantitation. **Talanta**, 281, 126799. *https://doi.org/https://doi.org/10.1016/j.talanta.2024.126799*

IF 6.1 (Q1)

Accumulative IF: 13.1

Publications not related to the thesis

I. Shao, Y., Chang, C., Huang, G., Yang, X., Hu, E., Ru, Y., **Ali, Z.**, Koch, M.A., Dernovics, M., Zhang, H. (2026) Critical review on the selenium speciation data reported for the Se-accumulator plant Cardamine violifolia/hupingshanensis /enshiensis: time to move beyond the myth of abundant selenocysteine/selenocystine content. **TrAC Trends in Analytical Chemistry**, in press

IF 12.0 (D1)

II. **Ali, Z.,** Lőrinczi, B., Simon, P., Cs. Fazakas, Cs., Wilhelm, I., Bogar, F., Ilisz, I., Vécsei, L., Szatmári, I., Berkecz**,** R., (2026) A comprehensive analytical approach for investigating the enhanced *in vitro* blood–brain barrier permeability of new kynurenic acid derivatives (**Talana**, under review)

PRESENTATIONS RELATED TO THE SUBJECT OF THE THESIS

Oral presentation

I. **Ali, Z.**, Frank, R., Körmöczi, T., Ilisz, I., Domoki, F., Weicznere, R., Bari, F., Farkas, E., Berkecz, R., Nimodipine saturation kinetics in acute rat brain slice. Spring Wind Conference 2024: International Multidisciplinary Conference, May 3-5. Budapest, 2024.

II. **Ali, Z.**, Berkecz, R. Bioanalytical LC-MS method development and applications for qualitative and quantitative analysis of exogenous and endogenous compounds. Three minutes PhD pitch, University of Alcala (UAH), Alcala de Henares, Spain September 2025.

Poster presentations

I. Berkecz R., Frank R., **Ali Z.**, Körmöczi T., Ilisz I., Domoki F., Farkas E. Monitoring rat brain slice nimodipine level using a new targeted UHPLC-MS/MS method. The 13th Balaton Symposium on High-Performance Separation Methods September 4-6, 2023, Hotel Azúr, Siófok, Hungary.

II. **Ali, Z.**, Frank, R., Körmöczi, T., Ilisz, I., Domoki, F., Weicznere, R., Bari, F., Farkas, E., Berkecz, R., Monitoring nimodipine level in brain using new targeted UHPLC-MS/MS method. The fourth Annual Summit of EUGLOH 2024: International Conference, June 11-14. Szeged, Hungary, 2024.

III. **Ali Z**, Frank R, Körmöczi T, Ilisz I, Domoki F, Weiczner R, Bari F, Farkas E, Berkecz R, Analytical Method Development and Application focusing on Nimodipine Kinetics in Rat Brain Tissue, First International Health Science Conference Szeged, Hungary, 29-31 May 2025

PRESENTATIONS NOT RELATED TO THE SUBJECT OF THE THESIS

Oral presentation

I. **Ali Z.**, Dávid Cs. Zs., Berkecz R. Combination of in silico and wet lab design in simultaneous analysis of stilbenes. Clauder Ottó Memorial Competition, November 13-14, Budapest, 2023.

II. **Ali Z.,** Dávid Cs. Zs., Vasas A., Ilisz I., Berkecz R. Simultaneous analysis of stilbenes, chromatographic design and application. 29th International Symposium on Analytical and Environmental Problems. November 16-17, Szeged, 2023.

III. **Ali Z;** Lörinczi B; Ilisz I; Szatmari I; Wilhelm I; Vécsei L, Berkecz R, Novel UHPLC-MS/MS method and permeability study of the brain penetrant neuroprotective agents: KYNA analogs—a critical step in drug development, 31th International Symposium on Analytical and Environmental Problems. October 13-14, Szeged, Hunagry,2025.

Poster Presentations

I. **Ali Z.,** Dávid Cs. Zs., Vasas A., Körmöczi T., Ilisz I., Berkecz R. Targeted UPLC-MS/MS method for the simultaneous determination of stilbenes derivatives in plant extract. The 13th Balaton Symposium on High-Performance Separation Methods September 4-6, 2023, Hotel Azúr, Siófok, Hungary.

II. **Ali Z**; Lörinczi B; Ilisz I; Szatmari I; Wilhelm I; Vécsei L, Berkecz R, *In vitro* permeability study of new KYNA analogues. The 14th Balaton Symposium on High-Performance Separation Methods September 7-9, 2025, Hotel Azúr, Siófok, Hungary.

TABLE OF CONTENTS

Abbreviations used in the thesis

aCSF	artificial cerebrospinal fluid
ACN	acetonitrile
AGC	automatic gain control
APCI	atmospheric pressure chemical ionization
APPI	Atmospheric pressure photoionization
aSAH	aneurysmal subarachnoid hemorrhage
ARRIVE	Animal Research: Reporting of *In Vivo* Experiments
BDE	bond dissociation energy
BEH	bridged ethyl hybrid
BSM	binary solvent manager
C30	triacontyl stationary phase
CE	collision energy
CH_2Cl_2	dichloromethane
CID	collision-induced dissociation
CNS	central nervous system
CV	coefficient of variation
DCI	delayed cerebral ischemia
DMSO	dimethyl sulfoxide
EDTA	ethylenediaminetetraacetic acid
ESI	electrospray ionization
EtOH	ethanol
EU	European Union
FA	formic acid
FDA	United States Food and Drug Administration
FWHM	full width at half maximum

H_2O	water
HCD	higher-energy collisional dissociation
HCl	hydrochloric acid
HESI	heated electrospray ionization
HILIC	hydrophilic interaction liquid chromatography
HPLC	high-performance liquid chromatography
HRMS	high-resolution mass spectrometry
HSV-2	herpes simplex virus type 2
ICH	International Council for Harmonisation
IPA	2-propanol
ISTD	internal standard
IT	injection time
LC	liquid chromatography
LC–MS	liquid chromatography–mass spectrometry
LC–MS/MS	liquid chromatography–tandem mass spectrometry
LLOD	lower limit of detection
LLOQ	lower limit of quantitation
LOD	limit of detection
logP	octanol/water partition coefficient
m/z	mass-to-charge ratio
MeOH	methanol
MID	middle concentration level
MRM	multiple reaction monitoring
MS	mass spectrometry
MS/MS	tandem mass spectrometry

N_2O	nitrous oxide
NaOH	sodium hydroxide
NMD	nimodipine
NMD-D7	deuterium-labeled nimodipine
NPLC	normal-phase liquid chromatography
PBS	phosphate-buffered saline
pH	potential of hydrogen
PLNO	partial loop needle overfill
PFP	pentafluorophenyl
pg	picogram
ppm	parts per million
PRM	parallel reaction monitoring
QC	quality control
Q Exactive	quadrupole-Orbitrap hybrid mass spectrometer platform
q2	collision cell in triple quadrupole MS
Q1	first quadrupole
Q3	third quadrupole
QqQ	triple quadrupole
R^2	coefficient of determination
RCF	relative centrifugal force
RF	radio frequency
RP	reversed phase
RP-LC	reversed-phase liquid chromatography
RT	retention time
SAH	subarachnoid hemorrhage

SIM	selected ion monitoring
S/N	signal-to-noise ratio
SRM	selected reaction monitoring
t_{max}	time to maximum concentration
TOF	time-of-flight
UHPLC	ultra-high-performance liquid chromatography
UHPLC–HRMS/MS	ultra-high-performance liquid chromatography–high-resolution tandem mass spectrometry
UHPLC–MS	ultra-high-performance liquid chromatography–mass spectrometry
UHPLC–MS/MS	ultra-high-performance liquid chromatography–tandem mass spectrometry
VGCC	voltage-gated calcium channel
v/v	volume per volume

1. Introduction

Bioanalysis is a branch of pharmaceutical science focused on the qualitative and quantitative determination of trace-level analytes in complex biological matrices. The analytes of interest may include endogenous compounds produced by living organisms, such as metabolites, biomarkers, and naturally occurring bioactive compounds (for example, phenanthrenes), as well as exogenous compounds of synthetic origin, such as drugs (e.g., nimodipine), synthetic derivatives, and other target substances. Biological matrices commonly include plasma, urine, blood, plants, microorganisms, and tissues of human or animal origin [1,2]. Bioanalytical data are essential for understanding the behavior of compounds in living systems and for supporting decision-making in pharmacokinetics, pharmacology, biotransformation studies, drug discovery, natural product research, and therapeutic monitoring [2–5]. Nevertheless, one of the major challenges in bioanalysis lies in the complexity of biological matrices, as numerous matrix components, including proteins, phospholipids, salts, amino acids, sugars, lipids, and endogenous metabolites, may interfere with analyte extraction, chromatographic separation, and detection. Therefore, bioanalysis extends beyond the simple measurement of a compound in a biological sample; it involves the development of a reliable analytical strategy capable of distinguishing and quantifying the analyte with adequate confidence. A suitable bioanalytical method must provide sufficient sensitivity, selectivity, precision, accuracy, and robustness, while also considering analyte stability, sample volume, and the intended biological application [1,4,5].

Liquid chromatography coupled with mass spectrometry (LC–MS) is one of the most important and widely used techniques in quantitative bioanalysis because of its high sensitivity, selectivity, reproducibility, and suitability for complex biological samples [1,3–5]. The following sections summarize the fundamental principles of liquid chromatography, mass spectrometry, and their combination, as a hyphenated technique, including the related general LC–MS workflow relevant to this thesis. Subsequently, two bioanalytical LC–MS methods, along with the related sample preparation techniques and data evaluation, are presented in this thesis to support pharmacokinetic studies, nimodipine monitoring, and the bioactivity-guided investigation of plant secondary metabolites, particularly phenanthrenes.

1.1 Liquid chromatography (LC)

Chromatographic separation is widely used in bioanalysis to separate analytes of interest from complex biological samples. In chromatography, sample components are distributed between a mobile phase and a stationary phase, and separation is achieved according to differences in their physicochemical properties and interactions with the stationary phase. Liquid chromatography

(LC), in which the stationary phase is packed into a column, and the mobile phase is a liquid flowing under pressure, is among the most used analytical techniques in this field [6]. Retention of targeted analytes depends on the chemical properties of the compounds, such as polarity, hydrophobicity, and ionization state, as well as the applied chromatographic parameters, including column chemistry, mobile-phase composition, flow rate, temperature, and gradient conditions [6]. Modern bioanalytical laboratories mainly employ high-performance liquid chromatography (HPLC) and ultra-high-performance liquid chromatography (UHPLC). Compared with conventional HPLC, UHPLC uses smaller particle sizes and higher operating pressures, enabling faster analyses, improved efficiency, narrower peaks, and lower solvent consumption. These features are especially advantageous in LC–MS workflows [7,8].

In bioanalysis, LC not only separates analytes from matrix components but also supports identification by retention time (RT) and reduces ion suppression of retained analytes entering the ion source. Thus, chromatography contributes to both analyte separation and in-line clean-up within the analytical workflow [6,8]. Liquid chromatographic methods may also be classified according to the polarity relationship between the stationary and mobile phases into normal-phase liquid chromatography (NPLC), reversed-phase liquid chromatography (RP-LC), and hydrophilic interaction liquid chromatography (HILIC). Among these, RP-LC is the most widely used mode in pharmaceutical and bioanalytical analysis and is also the principal separation mode applied in the studies included in this thesis [6,8].

1.1.1 Reversed-phase liquid chromatography (RP-LC)

In RP-LC, the stationary phase is relatively nonpolar or hydrophobic, commonly based on C18 or C8 bonded phases, whereas the mobile phase is relatively polar and usually consists of water mixed with an organic solvent such as acetonitrile or methanol, often containing volatile additives. Retention is mainly governed by hydrophobic interactions, so less polar analytes are generally retained longer, while more polar compounds elute earlier [6].

The C18 phases are the most commonly used stationary phases in RP-LC because of their broad applicability. Alternative phases such as C30, phenyl, biphenyl, and pentafluorophenyl may provide improved selectivity for specific analyte classes, particularly aromatic compounds and structurally related isomers [6]. In LC–MS methods, mobile phase modifiers such as formic acid, acetic acid, ammonium formate, and ammonium acetate are frequently used to improve chromatographic performance while maintaining compatibility with mass spectrometric detection [6,8]. Gradient elution is often preferred because it allows compounds with a wide range of hydrophobicities to be analyzed within a single run and helps reduce the accumulation of late-eluting matrix components on the column. Column temperature is another important parameter, as it affects solvent viscosity,

backpressure, mass transfer, peak shape, and selectivity [6,7]. RP-LC is especially well suited to LC–MS analysis because it provides broad analyte coverage, good compatibility with electrospray ionization, and flexible control of selectivity through adjustment of the stationary phase, mobile-phase composition, pH, and gradient profile [6,8]. Although chromatographic techniques provide efficient separation, they are often insufficient on their own for reliable identification and accurate quantitation in complex biological matrices. Since compounds with similar chromatographic behavior may exhibit similar retention times and baseline separation is not always achievable, a more selective detection technique, such as mass spectrometry (MS), is required [8].

1.2 Mass spectrometry (MS)

Mass spectrometry (MS) is an indispensable analytical technique in bioanalysis because of its high sensitivity, selectivity, low detection limits, and ability to provide molecular and structural information. In MS, analytes are detected as ions based on their mass-to-charge ratio (*m/z*), thereby providing selectivity beyond chromatographic retention. This is particularly important in complex biological matrices, where compounds with similar or identical retention behavior can still be distinguished by their mass spectra. For this reason, the coupling of liquid chromatography with mass spectrometry (LC–MS), as a hyphenated technique, has become one of the most powerful analytical approaches for the reliable identification and sensitive determination of analytes in bioanalytical applications [8].

1.2.1 Principle of MS

The basic principle of mass spectrometry involves three main steps: ion formation, ion separation, and ion detection. First, neutral molecules are converted into gas-phase ions in the ion source. These ions are then transferred to the mass analyzer, where they are separated according to their mass to charge ratio (*m/z*) values. Finally, the separated ions are detected and recorded as a mass spectrum, in which ion intensity is plotted as a function of *m/z* [8].

1.2.2 Basic scheme of mass spectrometry

A mass spectrometer consists of an ion source, a mass analyzer, and a detector, together with a vacuum system and data-processing software. Following sample introduction and ionization, the generated ions are separated in the analyzer and subsequently detected as electrical signals. In most instruments, the analyzer and detector operate under vacuum, whereas the ion source may operate either under vacuum or at atmospheric pressure, depending on the ionization technique (**Fig. 1**)[8].

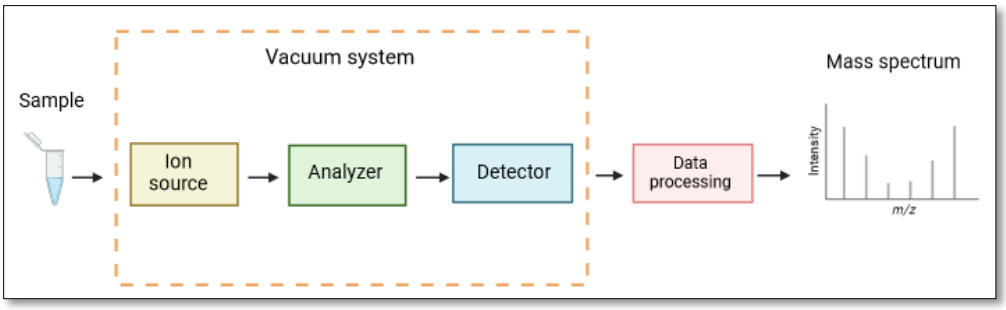

Fig. 1. Basic scheme of mass spectrometry

1.2.3 Electrospray ionization (ESI)

Among ionization techniques compatible with liquid chromatography, electrospray ionization (ESI) is among the most widely used and particularly relevant to the analytical methods presented in this thesis. ESI is well-suited for polar and moderately polar compounds and typically generates intact protonated or deprotonated molecular ions. Because fragmentation at the ion-source level is moderated, ESI is regarded as a soft ionization technique [9,10]. In ESI, the sample solution is introduced through a heated capillary held at high voltage, typically 3–5 kV. Under the influence of the electric field, a Taylor cone is formed at the capillary tip, from which charged droplets are emitted. As the solvent evaporates with the assistance of drying and nebulizing gases, the droplets decrease in size until gas-phase ions are produced. Ion formation in ESI is commonly explained by the charge-residue model and the ion-evaporation model. The latter is more often applied to lower-molecular-weight compounds, whereas the charge residue model is generally considered more suitable for larger molecules [9,10]. The ions remaining after nebulization are then introduced into the analyzer, which operates under high vacuum, through an orifice and ion optics (**Fig. 2**) [10]. Other atmospheric-pressure ionization techniques, such as atmospheric pressure chemical ionization (APCI) and atmospheric pressure photoionization (APPI), are also used in LC–MS, particularly for less polar compounds. Compared with APCI, which generally produces singly charged ions, ESI may also generate multiply charged ions.

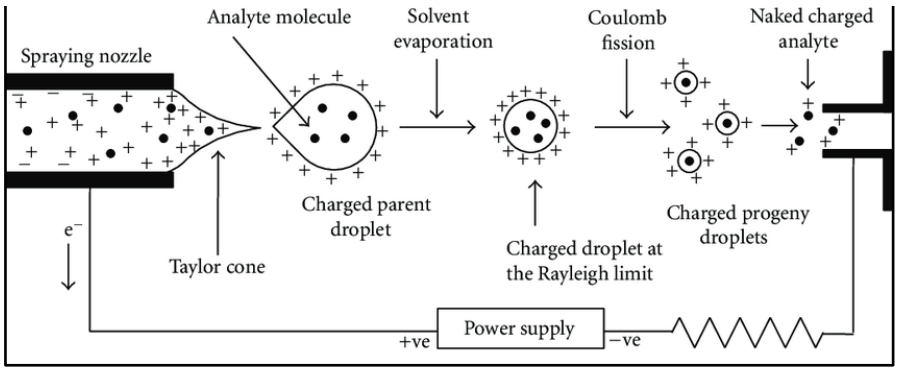

Fig. 2. Electrospray ionization process

1.2.4 Mass analyzers and detectors

Once formed, ions enter the mass analyzer, where they are separated according to their *m/z* values. Different analyzer types are used in modern mass spectrometry, including quadrupoles, ion traps, time-of-flight (TOF), and Orbitrap analyzers. These differ in key performance characteristics such as mass range, mass accuracy, resolution, and scan speed. Mass accuracy describes how closely the measured mass of an ion matches its theoretical value and is commonly expressed in Daltons or parts per million (ppm). Resolution describes the ability of the analyzer to distinguish between ions of similar *m/z* values and is typically defined using the full width at half maximum (FWHM) of a peak [11–13]. In general, quadrupole and ion trap analyzers provide high sensitivity but limited resolution, whereas TOF, FT-ICR, and Orbitrap analyzers offer high resolving power and accurate-mass capability. Accordingly, triple quadrupole instruments are most commonly used for targeted quantitative analysis, while high-resolution analyzers such as TOF and Orbitrap systems are particularly valuable for comprehensive analysis, analyte confirmation, and the study of structurally related compounds [11–13].

For accurate recording of ion signals, a reliable detector is also required. Common detector types include electron multipliers, microchannel plates, photodiodes, and Faraday cups. The detector records the signal intensity of the separated ions and generates the mass spectrum, in which the most intense ion is referred to as the base ion and its corresponding peak as the base peak [8]. In this work, two instruments were used: a Thermo TSQ Fortis triple quadrupole mass spectrometer and a Thermo Q Exactive Plus Hybrid Quadrupole-Orbitrap mass spectrometer. Therefore, the triple quadrupole and Orbitrap analyzers are presented in more detail in the following sections.

1.2.5 Tandem mass spectrometry (MS/MS)

Tandem mass spectrometry (MS/MS) refers to mass spectrometric analysis involving at least two stages of mass selection separated by a fragmentation step. In this approach, a selected precursor ion is first isolated, then fragmented, usually by collision-induced dissociation (CID), and the resulting product ions are subsequently analyzed. This process provides additional structural information and substantially increases analytical selectivity [12]. The main advantage of MS/MS is that it allows analytes to be distinguished more effectively from co-eluting matrix components than single-stage MS. Compounds may share similar retention times or even similar precursor ions, but their fragmentation patterns often differ. This added level of selectivity is one of the main reasons why LC–MS/MS has become a central analytical strategy in bioanalysis [8,12].

1.2.6 Triple quadrupole mass spectrometry and multiple reaction monitoring (MRM)

A quadrupole mass analyzer consists of four parallel rods to which combined direct current and radiofrequency voltages are applied (**Fig.3**). Only ions with stable trajectories under a given set of

electrical conditions can pass through the quadrupole, while others collide with the rods and are removed [11]. In a triple quadrupole (QqQ) instrument, two quadrupoles (Q1 and Q3) function as mass filters, whereas the intermediate quadrupole (q2) serves as a collision cell in which fragmentation occurs, typically by CID using nitrogen or argon as collision gas (**Fig.3**) [12].

Triple quadrupole instruments can be operated in several acquisition modes, including full scan, selected ion monitoring (SIM), product ion scan, precursor ion scan, neutral loss scan, and multiple reaction monitoring (MRM), also referred to as selected reaction monitoring (SRM). Among these, MRM is the most important and widely used mode in quantitative LC–MS/MS bioanalysis because of its high sensitivity and selectivity in complex matrices [8,12]. In MRM mode, Q1 selectively transmits the precursor ion of the analyte, fragmentation occurs in q2, and Q3 monitors a selected product ion. Because only predefined precursor-to-product ion transitions are recorded, background noise and matrix interference are greatly reduced, resulting in improved signal-to-noise ratio and enhanced analytical sensitivity. Multiple transitions can be monitored during a single chromatographic run, enabling the simultaneous quantitation of analytes and internal standards. For reliable identification in quantitative bioanalysis, at least two transitions are commonly monitored: one quantifier ion for quantitation (Quan) and one qualifier ion for confirmation (Qual) [8,12]. The use of internal standards, ideally stable isotope-labeled analogues, further improves robustness by compensating for sample preparation losses, ionization variability, and instrumental drift [8,12].

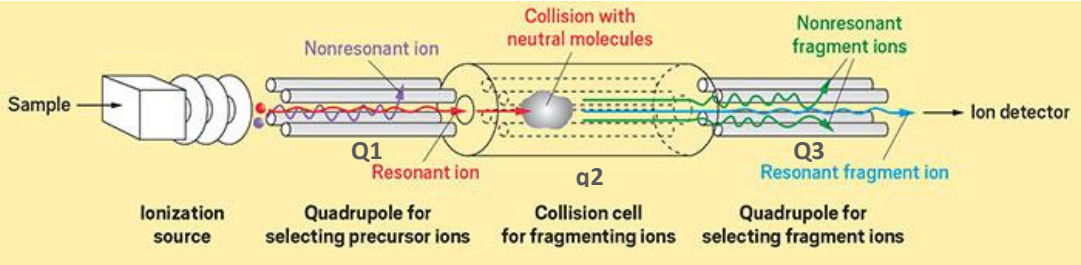

Fig.3. Triple quadrupole scheme

1.2.7 Orbitrap mass spectrometry, high-resolution MS, and parallel reaction monitoring (PRM)

The Orbitrap is a high-performance mass analyzer that traps ions in an electrostatic field and determines their *m/z* values from the frequency of ion oscillation. It provides high resolution, high mass accuracy, and excellent selectivity, making it especially useful for the analysis of complex samples and structurally related compounds. In Q Exactive-type instruments, a quadrupole placed before the C-trap enables precursor-ion selection, while the higher-energy collisional dissociation (HCD) cell allows fragmentation. The resulting ions are then transferred to the Orbitrap analyzer, where the image current produced by ion motion is measured and converted into a mass spectrum by Fourier transformation (**Fig.4**) [13]. High-resolution mass spectrometry (HRMS) is particularly

valuable when analytes are structurally similar, when matrix background is substantial, or when exact-mass fragment data are needed to strengthen analyte confirmation [1315]. Parallel reaction monitoring (PRM) is a targeted HRMS acquisition mode commonly used on Orbitrap instruments. As in MRM, a defined precursor ion is first selected. However, instead of monitoring only one selected product ion, PRM records the full fragment-ion spectrum of the selected precursor in the high-resolution analyzer. This allows quantifier and qualifier ions, besides additional fragment ions, to be extracted after acquisition with accurate-mass selectivity, thereby increasing flexibility and confidence in analyte confirmation (**Fig.5**) [14,15]. PRM offers several advantages. Because all fragment ions are acquired together, it provides more detailed fragment-level information than a single low-resolution transition. In addition, accurate-mass extraction reduces the probability of interference, and fragment ions can be selected or refined during data processing if required. These features make PRM particularly useful for analytes in chemically complex matrices and for structurally related compounds [14,15].

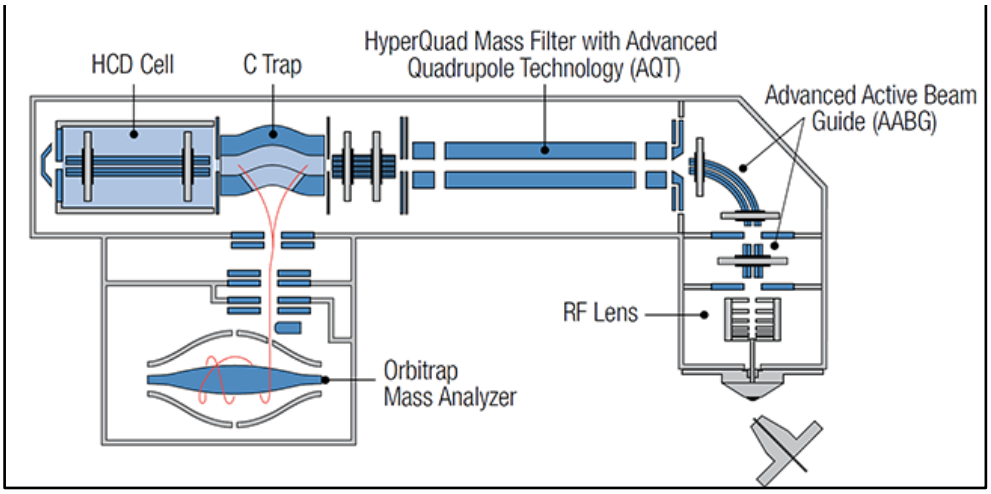

Fig. 4. Q-Exactive Hybrid Plus instrument

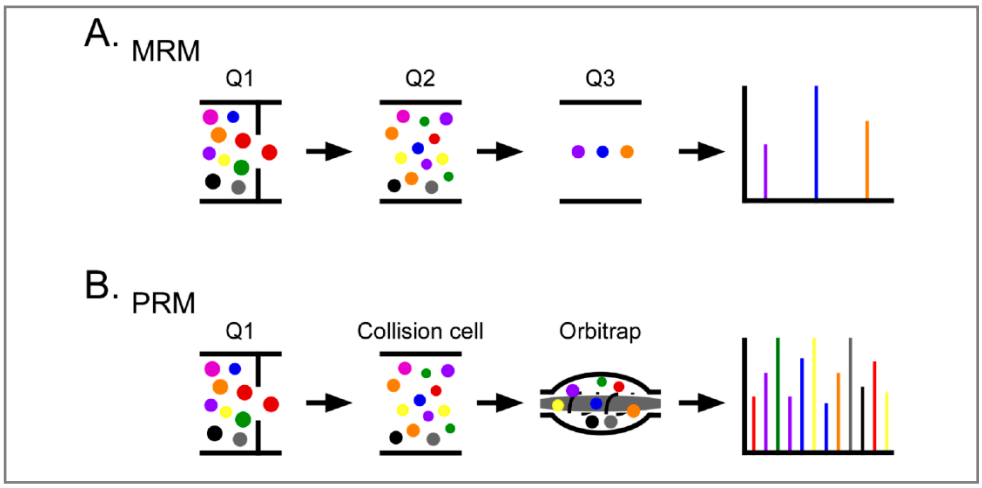

Fig. 5. (A) MRM and (B) PRM

1.2.8 LC-.MS workflow

LC–MS workflow (**Fig. 6**) starts with biological sample collection, including plant-derived materials and other biological matrices. Since such samples are chemically complex, sample preparation is a critical step and may involve homogenization, extraction, centrifugation, filtration, and clean-up prior to analysis. The prepared samples are then analyzed by UHPLC–MS or UHPLC–MS/MS, during which both chromatographic and mass spectrometric conditions are optimized to achieve suitable selectivity, sensitivity, and analytical performance. For quantitative applications, method validation is performed to confirm the reliability of the developed procedure [16]. Finally, the generated data are processed and statistically evaluated to support analyte quantitation and interpretation of results.

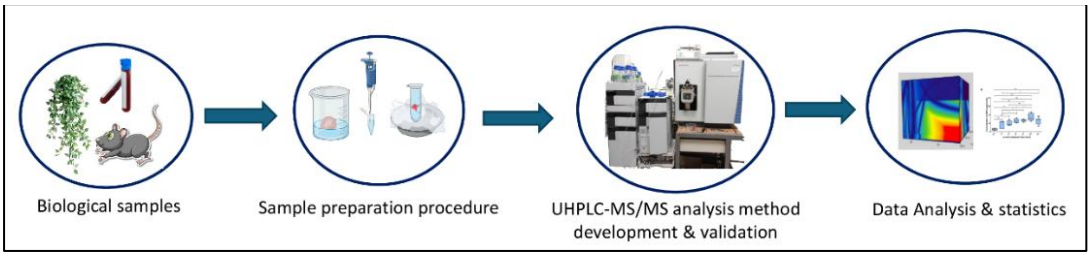

Fig. 6. General workflow of LC-MS analysis

1.3 Nimodipine (NMD)

Nimodipine (**NMD**) is a second-generation 1,4-dihydropyridine derivative and an L-type voltage-gated calcium channel (VGCC) blocker (**Fig. 7**). It was approved by the United States Food and Drug Administration (FDA) in 1988 for the management of vasospasm following aneurysmal subarachnoid hemorrhage (aSAH) [17].

Subarachnoid hemorrhage (SAH) refers to the accumulation of blood in the subarachnoid space, located between the arachnoid membrane and the pia mater surrounding the brain, and is associated with high mortality and morbidity [18]. Approximately 80% of SAH cases are caused by rupture of an intracranial aneurysm. Following aSAH, neurological deterioration may occur during the subsequent weeks, and delayed cerebral ischemia (DCI) represents one of the most common complications [19]. To date, **NMD** remains the cornerstone therapy for the prevention of DCI in patients with aSAH and is therefore administered as soon as the diagnosis is established [17].

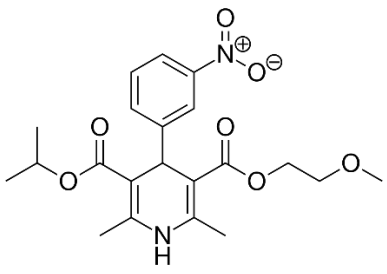

Fig. 7. Chemical structure of nimodipine

The primary target of **NMD** is the cerebrovascular smooth muscle cell, where blockage of L-type VGCCs promotes vasorelaxation through inhibition of Ca^{2+} influx [17]. Acute brain slice preparations are inherently devoid of cerebral circulation and therefore provide a suitable reductionist model for investigating the direct action of nimodipine on nervous tissue independently of its vascular effects [20]. Recently, several studies have shown that the properties of injurious insults in brain slices can be modulated by pharmacological interventions [21]. Nevertheless, the direct effect of nimodipine on nervous tissue at risk of injury has not yet been investigated in detail. For this reason, the design of an acute brain slice experiment and the investigation of **NMD** tissue saturation kinetics can provide valuable insights, particularly under different pH conditions. Tissue pH is a highly relevant physiological factor in ischemic brain injury. During ischemic stroke, marked tissue acidosis occurs in the brain, typically within a pH range of 6.5–6.8, while interstitial brain pH may even fall below 6.0 during severe ischemia in adults or asphyxia in neonates [22-25]. In contrast, the penumbra region in focal cerebral ischemia has been reported to become mildly alkaline, with an average pH of 7.32, whereas reperfusion after ischemia may induce more pronounced tissue alkalosis, with an average pH of 7.63 (**Fig. 8**) [22,26,27]. These pH changes are functionally important because mild acidosis reduces neuronal excitability, whereas alkalosis increases it. More importantly, marked or persistent acidosis has been recognized as a significant pathomechanism of neuronal injury [27–29]. Since drug pharmacokinetics may also be influenced by pH, this factor should be considered when characterizing tissue saturation. In the present work, it is therefore essential to determine whether nimodipine, as a compound with potential neuroprotective relevance, can be effectively taken up by tissues at risk of injury under pH conditions outside the physiological range.

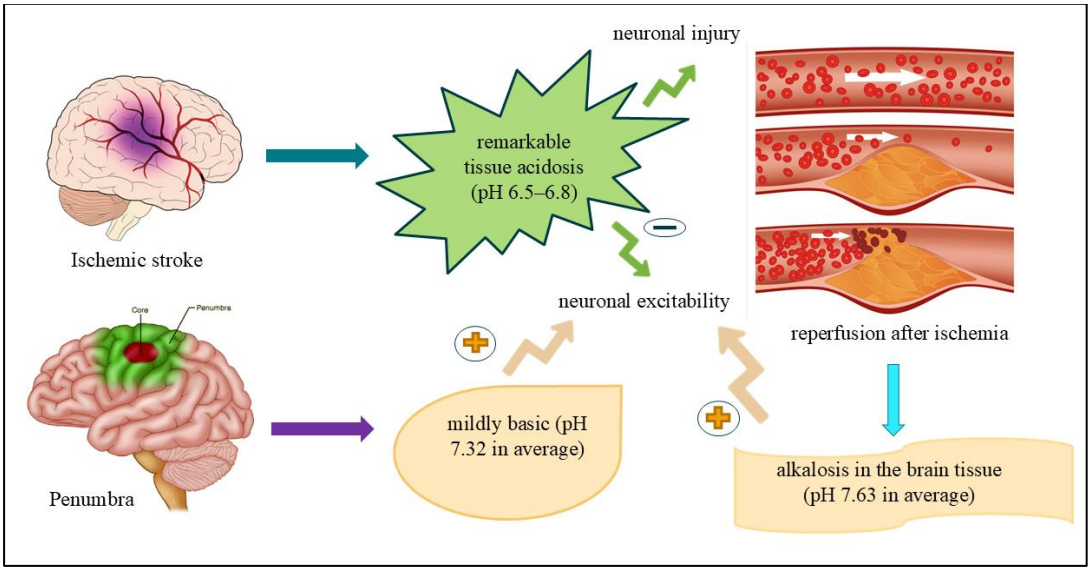

Fig. 8. pH changes in the tissues of the brain in different conditions

For decades, **NMD** has been determined in urine and plasma samples using gas chromatographic methods in combination with various detection techniques, requiring a time-consuming, complex sample preparation procedure [30,31,32]. With the development and expansion of liquid chromatography (LC), new achiral and chiral LC methods also appeared in the literature of **NMD** analysis. These methods employed isocratic reversed-phase or normal-phase separation with amperometric or UV detection, typically at 358, 254, or 237 nm, but generally provided relatively high limits of detection, such as 15 ng/mL in plasma and 100 ng/g in tissues [33–38]. Because biological matrices are inherently complex, more selective and sensitive hyphenated analytical techniques are required for reliable quantitative determination of nimodipine. Owing to **NMD's** lipophilic character, it has also been analyzed by supercritical fluid chromatography coupled with mass spectrometry. This approach enabled fast analysis within 2 min at a flow rate of 1.5 mL/min and achieved a limit of detection of 0.5 ng/mL in dog plasma [39,40]. At present, however, tandem mass spectrometry using electrospray ionization is among the most frequently used analytical methods for **NMD** determination in animal and human samples. In particular, LC–MS/MS provides efficient chromatographic separation and sensitive, selective detection, achieving limits of detection as low as 0.1 ng/mL in plasma while requiring smaller sample volumes than LC–UV methods [37,41–44].Although several analytical methods have been reported for determining nimodipine in biofluids such as plasma and cerebrospinal fluid, only a limited number of studies have addressed its quantitation in brain tissue, mainly using LC separation combined with spectrophotometric detection [34,35,45,46]. In addition, validation data were unavailable in most cases, and recovery in microdialysis-based applications depends strongly on the characteristics of the probe [34,35,45]. Therefore, a sensitive and reliable analytical method is needed to determine **NMD** concentrations directly at its site of action, namely the brain, and to study its saturation kinetics under physiologically relevant conditions.

1.4 Phenanthrenes

Phenanthrenes are a small but structurally diverse group of naturally occurring aromatic plant secondary metabolites. They possess a tricyclic phenanthrene skeleton, which may occur either in fully aromatic form or as 9,10-dihydrophenanthrene derivatives. Their structural diversity arises mainly from variation in the number, type, and position of substituents, such as hydroxyl, methoxy, methyl, and vinyl groups, as well as from oxidative coupling processes that may lead to more complex dimers or oligomeric structures. Accordingly, phenanthrenes are generally classified into mono-, di-, and triphenanthrenes, while further subclassification is based on the substitution pattern and the linkage between monomeric units (**Fig.9**) [47,48].

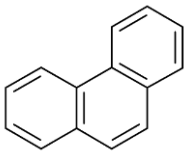

Fig. 9. Phenanthrene structure

Phenanthrenes are found prominently in the *Orchidaceae* and *Juncaceae* families. Species of the genus *Juncus* have attracted considerable interest as particularly rich sources of phenanthrene derivatives [47–49]. *Juncus compressus* Jacq. is a rhizomatous perennial species that grows in marshes, wet meadows, and other humid habitats, including mildly brackish environments, across temperate regions of Eurasia [50].

Interest in phenanthrene research has increased in recent years due to its broad range of biological activities, including antimicrobial, antioxidant, antiviral, anti-inflammatory, and cytotoxic properties, suggesting that phenanthrenes may represent promising pharmacologically relevant natural products [47,48]. Particularly, phenanthrenes isolated from *J. compressus* have demonstrated notable antiproliferative activity against HeLa cervical cancer cells and considerable antiviral activity against herpes simplex virus type 2 (HSV-2) [50]. Therefore, this metabolite class is biologically relevant and requires a reliable analytical approach for its characterization and quantification in plant matrices.

From an analytical perspective, phenanthrenes present several challenges. First, they often occur in low amounts in chemically complex plant extracts that contain numerous co-extracted endogenous compounds. Second, many phenanthrenes are closely related in structure and may differ only in the number or position of substituents. As a result, structurally related analogs and positional isomers may exhibit similar chromatographic behavior, making their separation and identification difficult. Third, the substitution pattern strongly affects ionization efficiency and fragmentation behavior, which, in turn, influence both detectability and selectivity in mass spectrometric analysis. These factors together make the development of selective and reliable methods for phenanthrene analysis particularly demanding [48,51]. LC–MS hyphenated techniques provide an especially suitable analytical platform for the investigation of phenanthrenes, and RP-LC is generally appropriate for these compounds due to their aromatic scaffold and moderate hydrophobicity, allowing efficient retention and separation, while MS detection provides an additional degree of selectivity beyond retention time alone. [48,51]. Despite the pharmacological and phytochemical relevance of phenanthrenes, their analytical investigation remains relatively limited compared with many other natural-product classes. Only a restricted number of studies have employed LC–MS or LC–MS/MS methods for their determination, and the available reports differ considerably in chromatographic mode, ionization polarity, and mass spectrometric strategy. In the case of Juncaceae species, LC–

MS approaches have previously been used to investigate selected phenanthrenes in biologically active extracts [51]. Nevertheless, broader mass spectrometric characterization of phenanthrenes remains insufficient, particularly for interpreting their fragmentation pathways [48,51].

Detailed knowledge of fragmentation behavior is especially important for phenanthrenes, as structurally similar compounds may yield related but not identical product-ion spectra. Therefore, fragmentation studies can provide valuable support for structural elucidation, analyte confirmation, distinction between closely related compounds, and the selection of suitable ions for targeted quantitative methods. This is particularly relevant in high-resolution mass spectrometric workflows, where accurate-mass fragment ions can strengthen confidence in identification in chemically complex matrices [48]. Moreover, compared with positive-ion measurements, the negative-ion fragmentation behavior of phenanthrenes has been much less systematically investigated. This represents an important analytical gap, because negative-ion MS and MS/HRMS may yield structurally meaningful fragment ions that improve both selectivity and confirmation, especially for substituted phenanthrenes co-occurring in complex plant extracts [48].

2. Aims and objectives

This work aimed to address biologically relevant questions through an analytical approach by developing, validating, and applying UHPLC-MS/MS and UHPLC-MS/HRMS methods for the qualitative and quantitative determination of targeted analytes. Novel sample preparation procedures, comprehensive fragmentation studies, state-of-the-art analytical methods, and full bioanalytical validation supported this endeavor.

Since the brain is the primary organ where **NMD** exerts its effect, and pH changes in the brain areas may influence **NMD** distribution in the CNS, we aimed to investigate the effects of pH changes on the saturation kinetics of **NMD** in acute rat brain slice preparations. For this purpose, a targeted UHPLC-MS/MS method was developed, validated, and applied for the quantitative measurement of **NMD** levels in brain tissue using a small sample quantity and a simple liquid-liquid extraction procedure with a short chromatographic run time. In the pharmacology aspect of the new analytical method application, to the best of our knowledge, this is the first attempt to report pharmacokinetic studies of **NMD** in acute rat brain slice preparations.

Another objective of our work was to address a gap in phenanthrene research by investigating its detailed fragmentation behavior in negative ionization mode, which had not been studied previously. To better understand this process, proposed fragmentation pathways were established based on MS/HRMS data. In addition, a targeted UHPLC–MS/HRMS method was developed and applied for the quantitative determination of phenanthrenes in *Juncus compressus*.

3. Experimental part

3.1 NMD saturation kinetics in acute rat brain slice

3.1.1 Tested materials

The internal standard of nimodipine (**NMD-D7**) [1,4-Dihydro-2,6-dimethyl-4-(3-nitrophenyl)-3,5-pyridinedicarboxylic acid and 3-(2-methoxyethyl) 5-(1-methylethyl-d7) ester] with a purity of >95% was obtained from Biosynth Carbosynth (Biosynth AG, Staad, Switzerland). Nimodipine (**NMD**) [3-(2-Methoxyethyl) 5-propan-2-yl 2,6-dimethyl-4-(3-nitrophenyl)-1,4-dihydropyridine-3,5-dicarboxylate] having higher than 98% of purity was obtained from Sigma-Aldrich (St. Louis, MO, USA).

3.1.2 Chemicals and standards for investigating NMD saturation kinetics in acute rat brain slice using UHPLC-MS/MS

For the pharmacological treatment and preparing the acute brain slice preparation, NaCl, KCl, $NaHCO_3$, $CaCl_2$ dihydrate, D (+)-sucrose, and Na_2HPO_4 dihydrate were purchased from Molar Chemicals Ltd. (Halásztelek, Hungary). $MgSO_4$ monohydrate was provided by Acros Organics (Thermo Fisher Scientific, Waltham, MA, USA) and KH_2PO_4, ethylenediaminetetraacetic acid (EDTA) disodium salt dihydrate were from Reanal Ltd. (Budapest, Hungary). D (+)-Glucose anhydrous, dimethyl sulfoxide (DMSO), NaH_2PO4 monohydrate, Reag. Ph. Eur. ethanol absolute (EtOH), LC-MS grade water (H_2O), methanol (MeOH), acetonitrile (ACN), 2-propanol (IPA), and formic acid (FA) were from VWR (Radnor, PA, USA).

3.1.3 Preparation of acute brain slices and their treatment with NMD

The experimental procedures were authorized by the National Food Chain Safety and Animal Health Directorate of Csongrád-Csanád County, Hungary, and performed in agreement with the guidelines of the Scientific Committee of Animal Experimentation of the Hungarian Academy of Sciences (updated Law and Regulations on Animal Protection: 40/2013. (II. 14.) Gov. of Hungary), following the EU Directive 2010/63/EU on the protection of animals used for scientific reason, and reported according to the ARRIVE guidelines [52].

The steps are detailed in **Figure 10** as male, young adult Sprague-Dawley rats (body weight: 250 g; n = 9) were used in this study. Animals were purchased from the Department of Pharmacodynamics and Biopharmacy at the University of Szeged (Charles River Laboratories breed). Tap water and standard rodent chow were supplied ad libitum. The animals were housed under constant humidity, temperature, and lighting circumstances (23 °C, 12:12 h light/dark cycle). The procedures of acute brain slice preparation were similar to those described previously [53]. The brains of the rats were removed under isoflurane anesthesia (5% isoflurane in N_2O:O_2; 2:1). Coronal brain slices (350 μm)

from both hemispheres anterior to bregma were cut with a vibrating blade microtome (Leica VT1000S, Leica, Germany) and collected in ice-cold artificial cerebrospinal fluid (aCSF). The composition of aCSF was in mM concentrations: 130 NaCl, 3.5 KCl, 1 NaH_2PO_4, 24 $NaHCO_3$, 1 $CaCl_2$, 3 $MgSO_4$, and D (+)-Glucose. Slices were transferred to an incubation chamber filled with carbogenated aCSF (differences in mM concentrations: 3 CaCl2 and 1.5 $MgSO_4$) and incubated at room temperature until **NMD** treatment.

NMD (Sigma-Aldrich, 10 μM in 0.01% DMSO) was dissolved in carbogenated aCSF. Slices were incubated in **NMD**-containing aCSF for different durations (0.5, 10, 20, 30, 40, 50, 60 minutes)[34]. Following incubation, each slice was washed with phosphate-buffered saline (PBS), weighed, and stored at –80°C until further analysis.

The kinetics of tissue saturation with **NMD** were characterized at three pH levels, achieved by adjusting the incubation medium with 1 M HCl or 1 M NaOH. The three conditions established were physiological (pH 7.38), acidic (pH 6.50), and alkaline (pH 7.57). pH 6.50 and pH 7.57 are moderately acidic and alkaline, respectively. However, these values represent a significant pH change in the brain from a physiological perspective. Thus, pH 6.50 and pH 7.57 are indicated as acidic and alkaline, respectively, in the following.

3.1.4 Sample preparation procedure for enrichment of NMD from brain slice

A matrix-matched external calibration method was applied using internal standard normalization by **NMD-D7** for the quantitative analysis. The weighed brain samples were placed into 1.7 mL microcentrifuge tubes, and an appropriate volume of homogenizing buffer was added to obtain 0.091 mg/μL concentration of each homogenate. The homogenizing buffer contained 5 mM EDTA in saline, and its final pH was adjusted to 5.5 with 1 M sodium hydroxide solution. The brain slice was individually sonicated with a BioLogics Model 150VT ultrasonic homogenizer (BioLogics Inc., Manassas, VA, USA) for 1 minute at 50% power using a micro-tip probe with 50% pulse on ice.

To enrich **NMD** and reduce the disturbing matrix effect of endogenous compounds in brain homogenate, a liquid-liquid extraction procedure was performed using 1.7-mL microcentrifuge tubes (Corning Inc., Corning, NY, USA). Before the extraction, 20 μL brain EDTA homogenate was spiked with 10 μL internal standard solution composed of 470 nM of **NMD-D7** in MeOH/IPA/water (3/1/0.1 v/v/v%). For *in vitro* samples, 10 μL of MeOH/IPA/water (3/1/0.1 v/v/v%) or 10 μL of the given calibration solution was added for calibration points, followed by vortexing. For spiked samples, 500 μL of toluene was added and vortexed, then shaken with Bühler Dual-Action Shaker KL Type 2 (Edmund Bühler GmbH, Bodelshausen, Germany) for 5 min. Upon 5 min of incubation at 4°C, the sample was centrifuged at 21,380 RCF for 15 min. After centrifugation, approximately 500 μL of the upper organic phase was collected into the 1.7-mL

microcentrifuge tube and dried under nitrogen at ambient temperature. For UHPLC-MS/MS measurements, the dried extracts were reconstituted in 100 µL of MeOH/IPA/water (3/1/0.1 v/v/v%) and transferred into a 250 uL conical insert.

Two extractions were performed from each homogenate of *in vitro* brain slices, and the extracts were analyzed twice. Thus, four measurements were taken for each brain slice (**Fig. 10**).

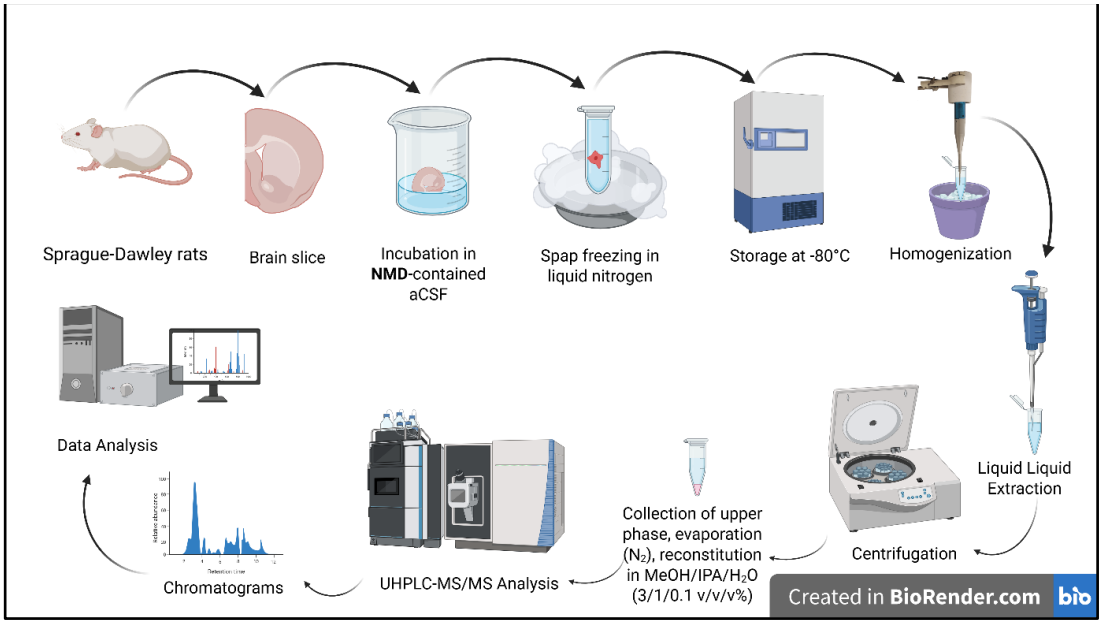

Fig.10. Workflow of **NMD** saturation kinetics investigation in acute rat brain slice using UHPLC-MS/MS approach

3.1.5 Targeted UHPLC–MS/MS parameters for NMD quantitation in acute rat brain slice

The targeted UHPLC–MS/MS analysis was performed using a Shimadzu Nexera (Kyoto, Japan) ultra-high-performance liquid chromatography (UHPLC) system connected via a 2-position, 6-port valve to a TSQ Fortis triple quadrupole tandem mass spectrometer (Thermo Scientific, Waltham, MA, USA). The Agilent 1100 HPLC pump (Agilent, Santa Clara, CA, USA) was used as an auxiliary pump.

UHPLC separations were performed using a Waters Acquity UPLC BEH C18 column (2.1 mm × 50 mm, 1.7 µm particles, equipped with a guard column, Milford, MA, USA). The column was thermostated at 50 °C during the analysis, and a flow rate of 0.4 mL/min was used. The composition of the A eluent was 0.1% FA in H2O, while 0.1% FA in ACN was used for the B eluent.

The final gradient program was the following: 0 min - 30% B, 1.5 min - 100% B, 3 min - 100% B, 3.1 min - 30% B, 5 min - 30% B. The injector needle was washed with ACN/H_2O/FA (60/40/0.1 v/v/v%) solution after each injection. The injection volume was 2 µL. The 2-position, 6-port divert valve was automatically controlled, and the UHPLC effluent was introduced into the MS only during 2–2.6 min. The ESI source was rinsed with ACN/H_2O (90/10 v/v%) eluent at a flow rate of

0.2 mL/min, and an auxiliary pump pumped the eluent to avoid contamination of the MS instrument. Atmospheric chemical ionization (APCI) settings were: the sheath gas flow of 45 a.u., the auxiliary gas flow of 5 a.u., sweep gas flow of 1 a.u., the capillary temperature of 300 °C, vaporizer temperature of 350 °C, and corona discharge current of 4 µA. For the final UHPLC-MS/MS method, electrospray ionization (ESI) mode was applied with the following parameters: the ion transfer tube temperature was set to 300 °C, the vaporizer temperature was 350 °C, the spray voltage was 4.5 kV, the sheath gas flow was 30 a.u., the sweep gas flow was 1 a.u., and the auxiliary gas flow was 14 in arbitrary unit. For the selected reaction monitoring (SRM) mode, the full width at half maximum (FWHM) was set to 2 for both Q1 and Q3 quadrupoles. For collision-induced dissociation (CID), the argon gas pressure was set to 1.5 mTorr. The determination of appropriate quantifier and qualifier ions for a protonated **NMD** and the optimization of ESI and MS/MS parameters were performed using a flow injection method. The UHPLC system was controlled by LabSolution Verison 5.97 SP1 (Shimadzu, Kyoto, Japan). Data acquisition, postprocessing, and quantitative evaluation of the MS/MS raw file were performed using Xcalibur 4.2 software (Thermo Fisher Scientific, Waltham, MA, USA).

3.1.6 Validation of the UHPLC-MS/MS targeted method for NMD

For the bioanalytical validation of the UHPLC-MS/MS method, the calibration series (n=5) was prepared by spiking **NMD**-free control brain homogenates with **NMD** standard solution, and the obtained concentrations were: 0, 0.023, 0.229, 1.146, 2.292, 11.462, 22.924, 114.621, and 229.241 µg/g brain. For calculating LOD, the standard deviation (n = 5) of the lowest calibration points with a 0.023 µg/g **NMD** concentration was divided by the mean slope of the five calibration curves, then multiplied by 3.3. The recovery, matrix effect, and process efficiency were determined according to the procedures of Matuszewski et al. and Trufelli et al. [54, 55]. To assess stability, bias, and precision, three concentrations were used: “LOW” (1.146 ng/g brain), “MID” (11.462 ng/g brain), and “HIGH” (114.621 µg/g brain). The stability of **NMD** in the autosampler was assessed by re-injecting the “LOW”, “MID”, and “HIGH” samples 24 hours after the first injection and comparing their concentrations with the original concentrations. Also, the stability of **NMD** in brain homogenate was determined in three concentrations (“LOW”, “MID”, “HIGH”) as compared to a sample stored at 4 °C for 3 days after sample preparation, and samples were measured immediately after sample preparation without storage. The long-term stability was determined as follows: *in vitro*-treated (for 30 min) brain slices at three different pH values were stored at -80 C for 1 year before being remeasured. The freeze-thaw stability was determined by subjecting the (“LOW”, “MID”, “HIGH”) samples to 3 freeze-thaw cycles. The bias values were calculated from data measured by injecting three individual samples five times in three concentrations (“LOW”, “MID”,

"HIGH"). For "LOW", "MID", and " HIGH" levels, within-run precision was determined from 3 individual samples in 3 individual analytical runs. To determine selectivity, individual brain homogenates from 6 different rat brains were prepared without the addition of **NMD** and **NMD-D7**. To investigate the carry-over in percentage, **NMD**-free control brain samples were injected after analysis of the highest calibration points (229.241 μg/g, respectively). The retention time stability of **NMD** was also assessed.

3.1.7. Data processing of NMD

For qualitative analysis, the obtained UHPLC–MS/MS raw files were processed manually, whereas the integrated processing setup in Xcalibur 4.2 was used for quantitative evaluation. GraphPad Prism 5.0 (GraphPad Software, San Diego, CA, USA) was used for ANOVA test, and BioRender was used to generate the algorithm figures. The maximum concentration (c_{max}) of **NMD** in the brain slice and the time to reach c_{max} (t_{max}) were determined from the concentration-time figure.

3.2 Pheneanethrenes

3.2.1 Chemicals and standards

The dried extracts of **Compound 1** (systematic name: 5-(1-methoxyethyl)-1-methyl-9,10-dihydrophenanthrene-2,7-diol), **Compound 2** (systematic name: 1-methyl-5-vinyl-9,10-dihydrophenanthrene-2,7-diol), **Compound 3** (systematic name: 1-methyl-5-vinylphenanthrene-2,7-diol), **Compound 4** (systematic name: 1,6-dimethyl-5-vinyl-9,10-dihydrophenanthrene-2,7-diol), **Compound 5** (systematic name: 1,1'-dimethyl-5,5'-divinyl-9,9',10,10'-tetrahydro-[3,3'-biphenanthrene]-2,2',7,7'-tetraol), **Compound 6**, **Compound 7** and the semi-synthetic **J3Z-13** (systematic name: 1,1'-dimethyl-5,5'-divinyl-9,9',10,10'-tetrahydro-[3,3'-biphenanthrene]-2,2',7,7'-tetraol, used as an internal standard, IS) (**Fig. 11**) were provided by the Department of Pharmacognosy, University of Szeged. All chemicals (LC-MS-grade water (H_2O), methanol (MeOH), acetonitrile (ACN), formic acid (FA), 2-propanol (IPA), dichloromethane (CH_2Cl_2), and hexane were from VWR (Radnor, PA, USA). Standard solutions, prepared in MeOH, were stored at –20 °C.

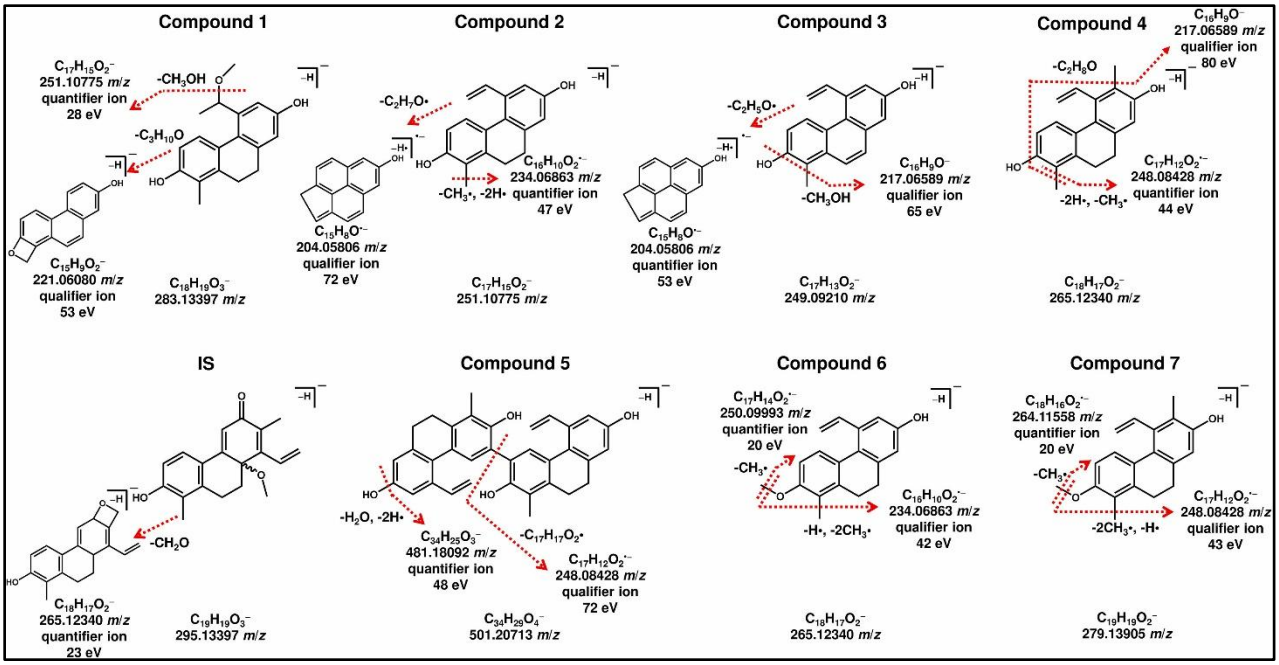

Fig.11: Assumed HESI-MS/HRMS fragmentation process of investigated phenanthrenes obtaining quantifier and qualifier ions.

3.2.2 Enrichment of phenanthrenes in *J. compressus*

At first, extracts (n = 3) were prepared from the aerial parts of *J. compressus*, collected in the flowering period in Hungary in June 2019. The plant sample was dried at room temperature and extracted with 5 × 100 mL MeOH by ultrasonication for 15 min. Then the extracts were filtered and evaporated under vacuum. The dried extracts were dissolved in MeOH–H_2O (50:50, v/v), and solvent–solvent partitions were performed with hexane (5 × 50 mL) and CH_2Cl_2 (5 × 50 mL). The crude MeOH and CH_2Cl_2 extracts were used for further analysis.

3.2.3 Preparation of calibration mixture and dry extracts for analysis

The 1.00 mg mL-1 stock solution of **Compound 1**, **Compounds 3-7**, **IS**, and 2.00 mg mL-1 stock solution of **Compound 2** were prepared in MeOH. The stock solutions were used to prepare working calibration standards. For eleven-point external calibration curves, the calibration points for each component were 0, 1, 10, 25, 50, 100, 250, 500, 1000, 2500, and 5000 nM in MeOH.

To obtain solutions at 0.1 mg mL-1, the dry extracts (MeOH and CH_2Cl_2) were dissolved in MeOH, then diluted tenfold and hundredfold. The 10 µL of **IS** (10 µM in MeOH) was added to 200 µL of both calibration points and *J. compressus* samples.

3.2.4 Direct MS/HRMS and UHPLC-HRMS/MS conditions

The MS/HRMS and UHPLC-MS/HRMS measurements were performed by Waters Acquity I-Class UPLC (Milford, MA, USA) and Thermo Scientific Q Exactive Plus Hybrid Quadrupole-Orbitrap (Waltham, MA, USA) mass spectrometer. The mass spectrometer was equipped with heated electrospray ionization (HESI) mode. The HESI parameters were set as follows: capillary temperature 220 °C, probe heater temperature 350 °C, S-Lens RF level 50, spray voltage 3.5 kV, sheath gas flow 48, spare gas flow 2.25, and auxiliary gas flow 11.25 in arbitrary unit. The MS/HRMS analysis was performed in negative-ion scheduled parallel reaction monitoring (PRM) mode with a resolution of 17,500 (FWHM). The AGC setting was set to 1×10^6 charges, and the maximum IT was set to 30 ms. For quadrupole isolation of precursor ions, ± 0.5 *m/z* mass range was used. The collision energies (CEs) were optimized for both the quantifier and qualifier ions of each component. For quantitation, the scheduled PRM was set to a 1.5–5 min retention time range. For the MS/HRMS study of phenanthrenes, the flow injection method was used, introducing the ACN–H2O (80:20, v/v) eluent and the standard phenanthrene solution (10 µM) at flow rates of 0.39 mL min-1 and 0.01 mL min-1, respectively, into the MS via mixing T. The MS/HRMS resolution was set at 70,000. For method development, the following chromatographic columns were studied: Acquity UPLC HSS C18 SB (2.1 × 100 mm, 1.8 µm), Acquity UPLC BEH C18 (2.1 × 100 mm, 1.7 µm), and Acquity UPLC HSS T3 (2.1 × 100 mm, 1.8 µm) from Waters (Milford, MA, UK). Kinetex Biphenyl (2.1 × 100 mm, 2.6 µm), Kinetex PFP (2.1 × 50 mm, 1.7 µm), and Kinetex C18 (2.1 × 100 mm, 2.6 µm) were from Phenomenex (Torrance, CA, USA). For the final UHPLC separation of phenanthrenes, the Accucore C30 column (150 × 2.1 mm, 2.6 µm) with an Accucore C30 guard column (10 × 2.1 mm, 2.6 µm) was selected from Thermo Fisher Scientific (Waltham, MA, USA). The UHPLC mobile phase A was H2O and mobile phase B was ACN. The gradient program started with 30% B, ramped to 100% B over 4.5 min, held it for 4 min, returned to initial conditions within 0.5 min, and equilibrated the column for 2 min. The flow rate and the injection volume were set to 0.4 mL min-1 and 2.5 µL. The column temperature and the autosampler were operated at 50 °C and 15 °C, respectively. To prevent sample cross-contamination during UHPLC injection, the Partial Loop Needle Overfill (PLNO) injection method was used and the 2-propanol–MeOH–H2O–FA (70:25:5:0.1, v/v/v/v) solution was used for weak and strong needle wash. To avoid the contamination of the HESI source, the UHPLC effluent was introduced into the MS via a 2-position, 6-port divert valve only in the 1.5–5 min time range. The HESI source was rinsed with ACN–H2O (90:10, v/v) eluent at a flow rate of 0.2 mL min-1 with an auxiliary pump in the remaining time. The final quantitative analysis was carried out in one batch, using an external calibration approach,

with each sample in three technical replicates. The peak areas were normalized to the IS peak area. The validation procedure was based on the U.S. Food and Drug Administration guidelines, using the calibration range as detailed in Section 2.3 [56]. The following three concentrations were used for the determination of stability, accuracy, and precision: “Low” (50 nM), “Mid” (500 nM), and “High” (2500 nM).

For controlling the UHPLC instrument, MassLynx 4.1 (Milford, MA, USA) software was used, while the HRMS data acquisition occurred by Xcalibur 4.4 software (Waltham, MA, USA).

3.2.5 Data processing

For quantitative evaluation of the UHPLC-MS/HRMS data, the raw files were processed using the Xcalibur software. The one-way ANOVA statistical analysis followed by Bonferroni’s post hoc test was performed by GraphPad Prism 5.0 (GraphPad Software, San Diego, CA, USA) software.

3.2.6 Computational method

Bond dissociation energies (BDEs) obtained from quantum chemical calculations were used to determine the initial steps of the fragmentation pathways of the investigated compounds, resulting in the obtained special distribution. Following the original definition, BDEs are calculated as the standard reaction enthalpy of the corresponding homolytic bond cleavage reaction [57]. The BDE characterizes the bond strength, provides insight into thermodynamically accessible reaction mechanisms, and helps identify dominant reaction pathways. It has many chemical applications, including the prediction of drug metabolism and fragmentation pathways in mass spectrometry [58–63]. The calculations presented here were performed with the MN15 density functional and the 6-31G+(d,p) basis set using the Gaussian 16 program [64–66]. Although this level of theory may not yield highly accurate BDE values, it is sufficient to estimate relative bond-cleavage probabilities.

4. RESULTS AND DISCUSSION

4.1 Nimodipine saturation kinetics in acute rat brain slice

4.1.1 Liquid chromatographic and mass spectrometric behavior of NMD

Based on the physicochemical properties of **NMD**, the theoretical pKa value (5.41) facilitates ionization in both negative and positive ESI modes [55, 67]. However, the MS detection of **NMD** in its deprotonated form is less reported in the literature [68–72]. Studying the ionization and fragmentation of protonated and deprotonated **NMD** demonstrated that precursor and fragment ion intensities were comparable in spectra recorded in both positive and negative ESI modes (**Figs. 12-16)**. The appropriate **NMD** transitions were selected from MS/MS scans using a CE ramp, and the related CEs were optimized in both ESI modes (**Fig. 12, Fig. S1-S3**) based on the intensity of given fragment ions. Preliminary LC runs showed that the presence of acid markedly improved the chromatographic peak shape of **NMD**. The significance of employing an acidic mobile phase further supported the detection of **NMD** in positive mode (**Fig. 14**). In case of the direct infusion method, the sodium adduct of **NMD** ([**NMD**+Na]$^+$) was predominant against protonated form ([**NMD**+H]$^+$) in positive mode (**Fig. 13**). For LC-MS analysis, using an isotope-labeled internal standard for the targeted compound can eliminate or minimize signal variability (resulting from sample preparation, LC injection, spray stability, etc.), especially in the analysis of biological matrices [73,74]. Therefore, deuterium-labeled **NMD** (**NMD-D7**) was selected as an internal standard for quantitative analysis [70, 75, 76]. By applying the flow injection technique, the formation of [**NMD**+H]$^+$ was significantly improved (**Fig. 14**) and can assist in the proper optimization of MS/MS parameters of protonated form. The standard **NMD** and **NMD-D7** solutions were introduced into the ESI source of the MS instrument at 5 µL/min through static mixing tee by mixing with the UHPLC mobile phase (ACN/H_2O/FA 90/10/0.1 v/v/v%) with a flow rate of 395 µL/min. For targeted UHPLC-MS/MS analysis, two transitions per compound were selected for quantitative analysis and qualitative confirmation within a related retention time window. The study of the fragmentation behavior of single-charged protonated **NMD** molecular ion [M+H]$^+$ at 419.2 *m/z* resulted in the production of two main fragment ions at 343.1 *m/z* and 301.1 *m/z* as the quantifier (for quantitation) and qualifier ion (for confirmation). For **NMD-D7**, 426.2 *m/z* –350.2 *m/z* and 426.2 *m/z* –302.1 *m/z* transitions were selected, and the corresponding CEs were optimized [41, 76–78]. The most abundant fragment ion, the quantifier ion, was produced by losing the 2-methoxyethyl group from the ester at the fifth position, yielding a resonance-stabilized acylium ion, and its resonance structures are shown in **Fig. 12** for both **NMD** and **NMD-D7**. For the qualifier ion, a further fragmentation process of the quantifier ion forms a free carboxyl group at the third carbon atom via cleavage of the ester bond [76, 77]. The full-scan mass spectrum of **NMD** revealed these fragment

ions, suggesting that **NMD** underwent source fragmentation during ionization (**Fig. 13-14**) despite maintaining a low cone voltage in positive mode.

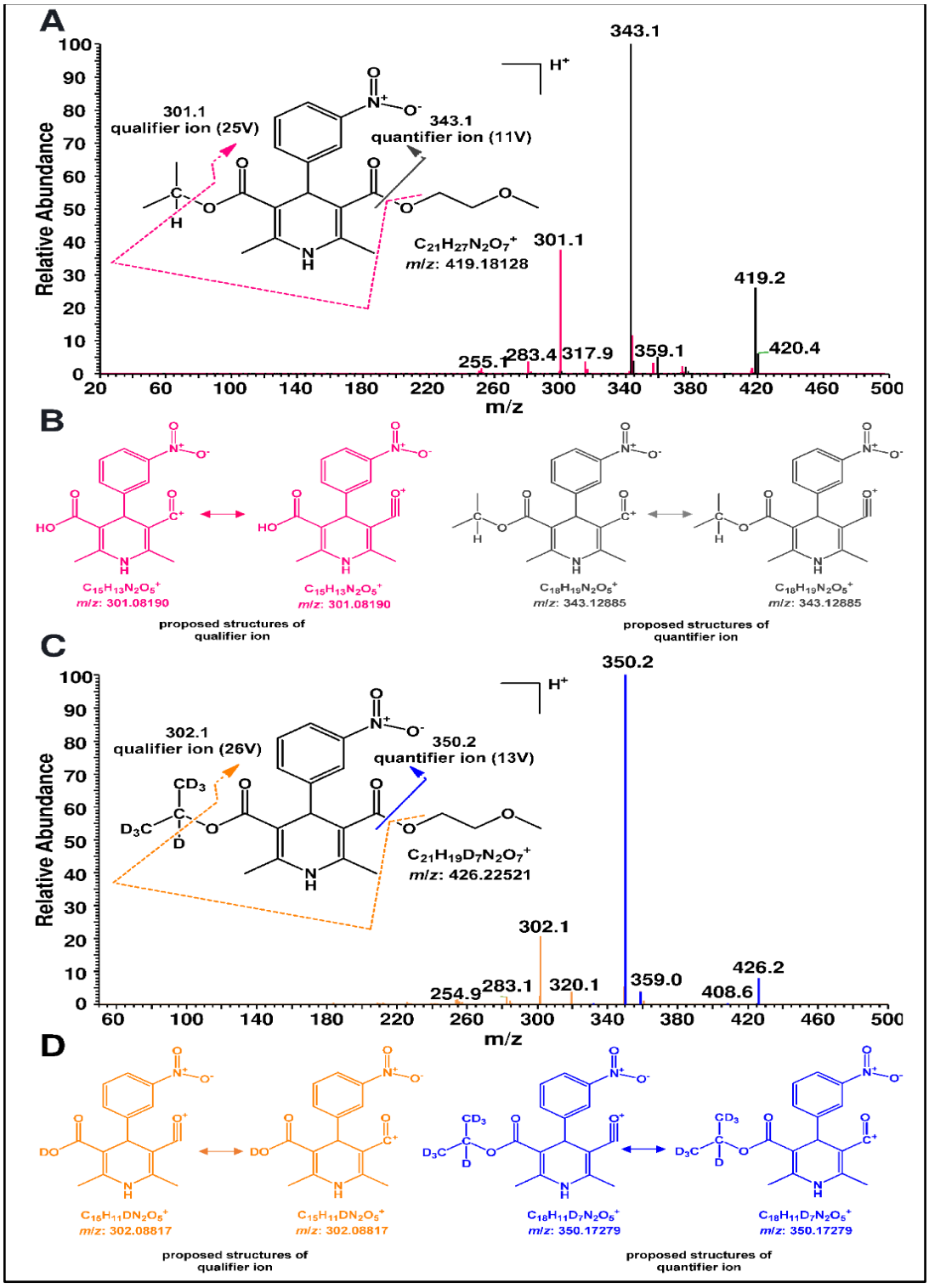

Fig. 12. (A) Overlayed MS/MS spectrum of **NMD** at optimized CE. (B) Proposed structure of quantifier (magenta) and qualifier ions (gray) of **NMD**. (C) Overlayed MS/MS spectrum of **NMD-D7** at optimized CE. (D) Proposed structure of quantifier (magenta) and qualifier ions (gray) of **NMD-D7**.

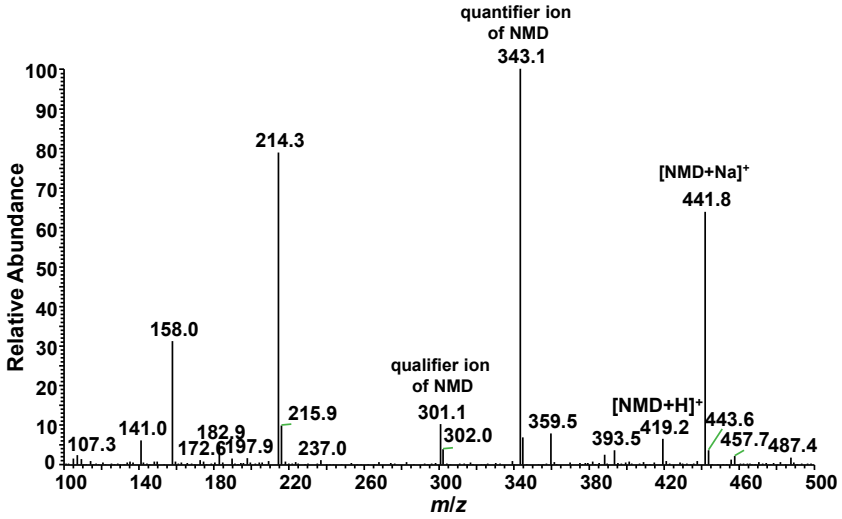

Fig. 13. Full spectrum of **NMD** in positive ESI mode using direct infusion method.

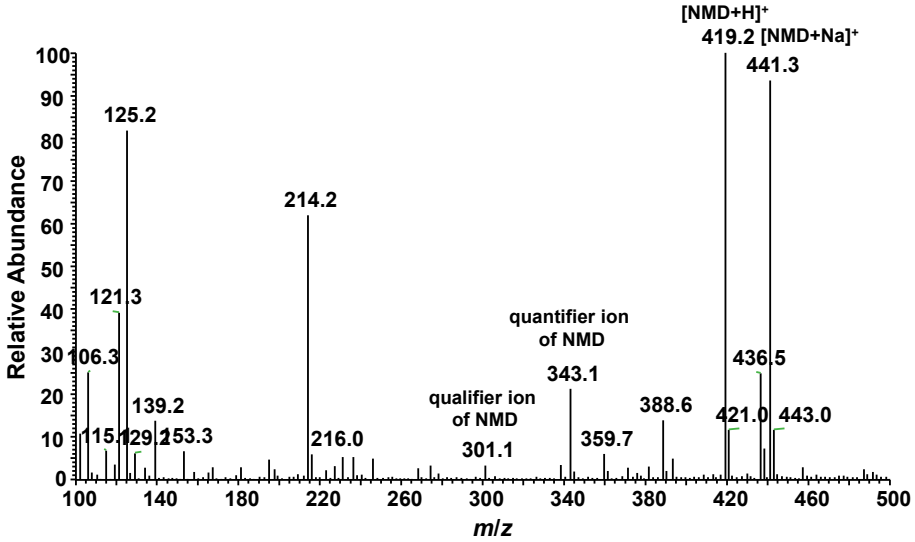

Fig. 14. Full spectrum of **NMD** in positive ESI mode using flow injection method.

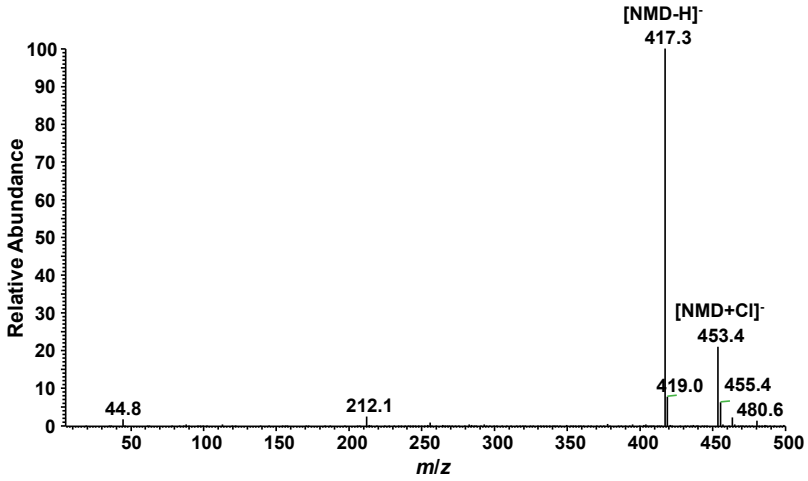

Fig. 15. Full spectrum of **NMD** in negative ESI mode using flow injection method.

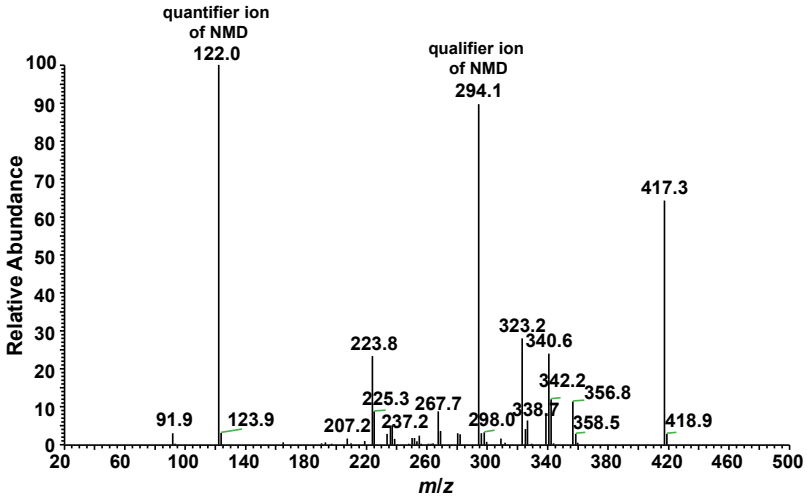

Fig. 16. MS/MS spectrum of **NMD** in negative ESI mode.

After selecting suitable transitions and optimizing MS/MS parameters, the LC conditions were further optimized. **NMD** can cross the blood-brain barrier due to its high lipophilicity (logP 3.41) [55, 79, 80], which supports its separation by reversed-phase liquid chromatography or supercritical fluid chromatography. In the literature, mainly the C18 solid phase and MeOH, ACN, and H_2O as mobile phases are used with modifiers (formic acid, ammonium formate, ammonium acetate) [41, 45, 68, 72, 76, 81–84]. Interestingly, several methods are based on isocratic separation in body fluids such as plasma, urine, and serum. In our case, the complexity of brain tissue, especially for its high phospholipid contents, requires gradient elution to avoid contamination of the reversed-phase chromatographic column [85]. Currently, a key requirement in the development of new analytical methods is minimizing total run time to enable high-throughput analysis. For gradient elution, the instrumental limitation is the delay volume, which is 410 µL in our UHPLC system. Regarding only a single targeted compound, selecting a short column is the proper approach for fast analysis. The application of BEH C18 column provided a symmetrical and narrow (<0.08 min) chromatographic peak for **NMD**, applying 0.1% FA in water as an A eluent and 0.1% FA in ACN as a B eluent (**Fig. 17**).

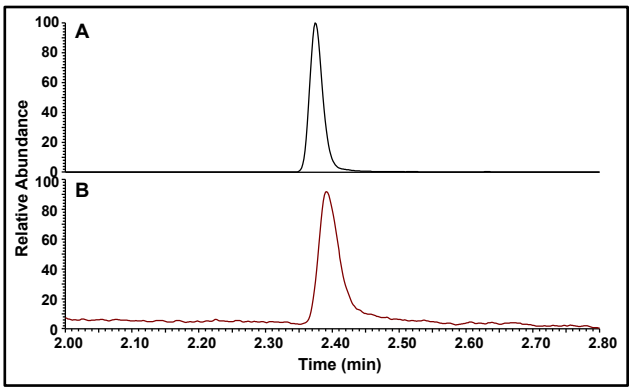

Fig. 17. Extracted ion chromatogram of quantifier ion of **NMD** (A) 0.1% FA in the mobile phase (B) without acid in the mobile phase.

Studying the contribution of organic solvent for chromatographic and mass spectrometric parameters of **NMD**, higher retention (2.74 min) and also higher pressure was observed for MeOH compared with ACN as expected. To avoid retaining brain lipids in the column during the washing period of the gradient program, ACN with higher eluent strength than MeOH was selected as the organic solvent of B eluent despite the observed higher peak area in the case of MeOH. The increased FA content in the mobile phase from 0.1% to 1% did not result in significant changes in peak retention time or peak area for both ACN and MeOH, indicating that the protonated form of **NMD** is dominant over this FA concentration range. The purpose of the gradient program optimization was to obtain satisfactory peak width, peak symmetry, and retention for **NMD** within a 5-minute total run time, which was comparable or better than earlier published LC methods to quantify **NMD** in biological samples [33, 35–38, 41, 42, 45, 46]. The application of a flow rate of 0.4 mL/min, a column temperature of 50 °C, and a linear gradient assisted in keeping the required chromatographic parameters. The application of the final UHPLC-MS/MS method yielded a symmetrical peak shape for **NMD** with a retention time of 2.35 min (**Fig. 18**).

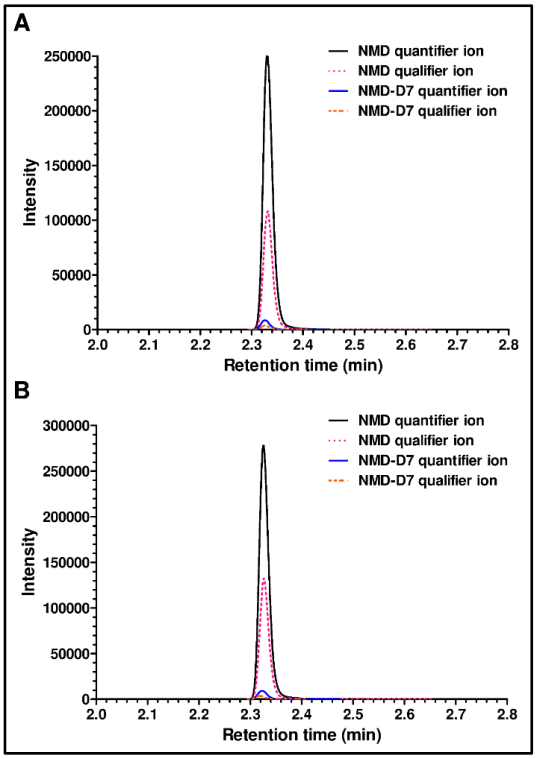

Fig. 18. (A) Extracted ion chromatogram of concentration calibration point (22.924 µg/g): **NMD** quantifier ion (black straight line), **NMD** qualifier ion (magenta dashed line), **NMD-D7** quantifier ion (blue straight line), **NMD-D7** qualifier ion (orange dashed line). (B) Extracted ion chromatogram of *in vitro* sample (pH: 7.38 , *in vitro* treatment time: 30 min): **NMD** quantifier ion (black straight line), **NMD** qualifier ion (magenta dashed line), **NMD-D7** quantifier ion (blue straight line), **NMD-D7** qualifier ion (orange dashed line).

After optimizing the chromatographic parameters, the applicability of APCI as an alternative to ESI was studied. Regarding atmospheric pressure ionization techniques, the literature reports conflicting results comparing ESI and APCI modes [41, 42, 86]. In our comparison of **NMD** peak areas obtained by UHPLC-APCI-MS/MS and UHPLC-ESI-MS/MS measurements of brain homogenate extracts, the ESI technique yielded significantly higher peak areas (**Fig. 19**).

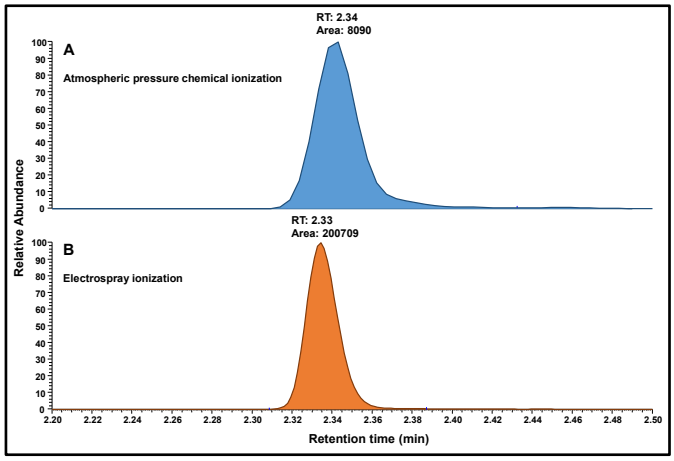

Fig. 19. For the 5. calibration point (11.46 ng/g brain), extracted ion chromatograms of **NMD** quantifier ion. Effect of ionization mode on **NMD** peak area: APCI mode (A, blue) and ESI mode (B, orange).

4.1.2 Enrichment of NMD in brain homogenate

The application of a proper sample preparation procedure is crucial for the enrichment of **NMD** and the reduction of negative matrix effects, mainly related to brain endogenous compounds. For **NMD**, liquid-liquid extractions and protein precipitation procedures for biofluids are widely reported in the literature. In the liquid–liquid extraction procedure, the lipophilic character of **NMD** facilitates its enrichment in the aprotic organic solvent [34, 42, 76, 80]. Therefore, we investigated the contribution of four organic solvents to the enrichment of **NMD** from brain homogenate. The highest peak area and signal-to-noise ratio (S/N) of **NMD** were observed with toluene (logP: 2.73) compared with hexane (logP: 3.90), ethyl acetate (logP: 0.73), and chloroform (logP: 1.97) (**Fig. 20**) [87-91]. The efficiency of toluene can be explained by its closer logP value to **NMD** than other investigated organic solvents' logP values, and its ability for the formation of further interactions (π– π stacking, π acid-base interaction) with the aromatic rings of **NMD**. Interestingly, the effect of different organic solvents resulting in different matrixes in the enriched samples was negligible on the retention and chromatographic peak symmetry of **NMD** (**Fig. 20**). Thus, toluene was selected for further study of the sample preparation parameters.

The application of toluene resulted in a high recovery of **NMD** in brain homogenate, accompanied by negligible matrix effects due to the more selective enrichment of **NMD** relative to coeluting brain endogenous compounds, such as brain phospholipids (**Table S1**) [85]. The two MS/MS transitions of **NMD** and **NMD-D7**, along with their ratios, were also monitored to exclude the apparent isobaric effect. The quantifier-to-qualifier ion ratios were 2.3 for **NMD** and 2.5 for **NMD-D7** in the analysis of brain samples. In biological assays, the available sample quantity is generally limited. Our analytical method requires only 20 µL of brain homogenate having 0.091 mg brain/µL homogenate concentration. In the literature, only a handful of papers are available on **NMD** analysis in the brain, and these methods require at least 80 µL of homogenate [34, 81]. The preparation of the stable brain homogenate is also a key factor in the sample preparation procedure. The stability of **NMD** for 3 days without any degradation was obtained in brain homogenate with the use of 5 mM EDTA solution at a pH of 5.5. Regarding the low solubility (2.3 µg/mL) and instability of **NMD** in an aqueous solution, the MeOH/IPA/water (3/1/0.1, V/V/V) mixture was selected for dissolving the dry extract, forming a stable homogenous solution without significant influence of chromatographic retention and peak shape of **NMD**.

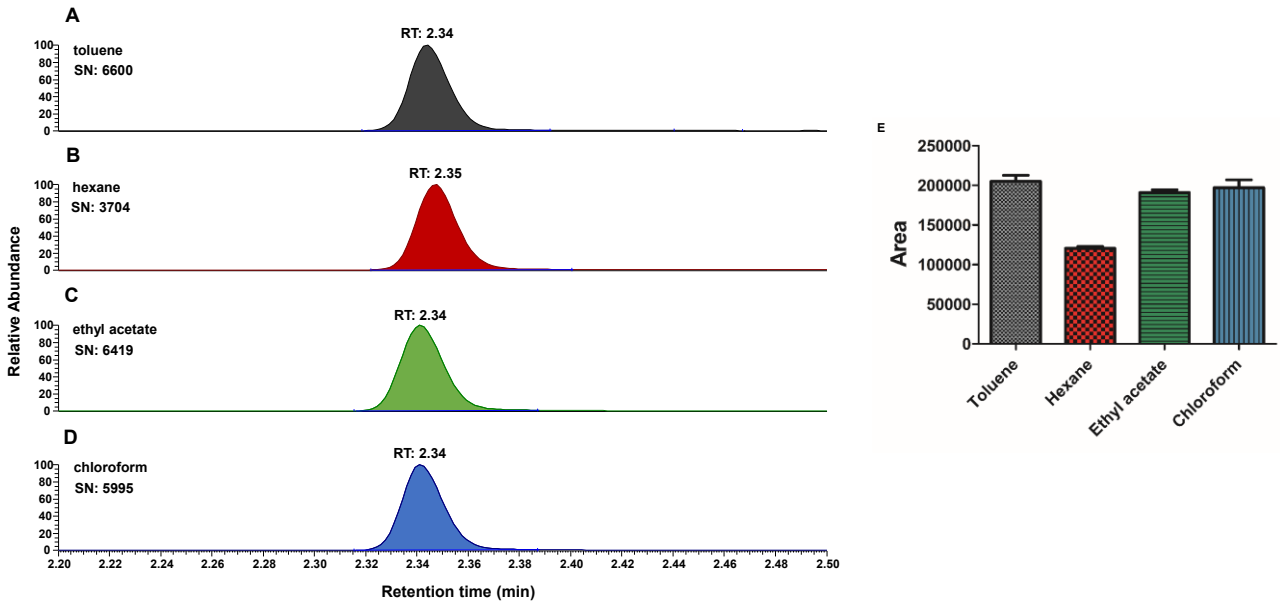

Fig. 20. For the 5. calibration point (11.46 µg/g brain), the extracted ion chromatograms of the **NMD** quantifier ion. Effect of different organic solvents on **NMD** chromatographic behavior (A), hexane (B), ethyl acetate (C), chloroform (D), and obtained peak areas (E).

4.1.3 Validation parameters of targeted UHPLC–MS/MS method

The study of validation parameters is crucial for determining the applicability of the new analytical method and the quality of the results. The new targeted UHPLC-MS/MS method was validated for quantitative analysis of **NMD** in the brain by detailed investigation of recovery, matrix effect,

process efficiency, lower limit of detection (LLOD), limit of linearity, accuracy, precision, carry-over, and stability. The applied validation criteria were determined in accordance with the ICH guideline for the validation of analytical procedures Q2(R1) [92]. **Table S1** summarizes the validation results obtained for **NMD**. The calculated and practical LLOD was determined to be 15 ng/g brain (547 fg injected **NMD** into the column) and was lower than previously reported (30 and 50 ng/g brain) [35, 46]. The study of calibration curve type and weighting showed that a linear approach without weighting yielded the best fit. For the linearity of the calibration curve of five independent calibration series, the concentration range was from 0.023 to 229.2 µg/g brain, and the related coefficient of determination (R^2) was found to be higher than 0.99. The calibration curve covered a wider concentration range than earlier published methods (from a 0.05 up to a 20 µg/g brain) [34, 35, 46, 81]. The obtained bias values passed within the accepted bias of ±20% in LOW and ±15% for MID, and HIGH concentration levels, respectively. The within-run and between-run precision values were below 5 and 10.5% in coefficient of variation (CV). With the high enrichment of **NMD** in the organic toluene phase, the recovery of **NMD** was found to be 96.9–110.6%, which was higher than previously reported [81]. The negative matrix effect (less than 10% of ion suppression) was observed only at the MID concentration level, while it was positive (3.3–12.9% of ion enhancement) for other levels, which indicates the ability of the developed sample preparation procedure to effectively eliminate the endogenous compounds disturbing the ionization of **NMD** from complex brain homogenate. The process efficiency, as a resultant of the recovery and matrix effect values, was in the range of 100.6–109.4%. To obtain valid analytical results, the stability of the targeted compound is an important aspect in tissues, homogenates, and prepared samples. The revealed stability values of **NMD** suggested that no significant analyte loss took place in any of the quality control (QC) samples, suggesting that samples awaiting analysis are stable for up to 3 days in brain homogenate (at 4 °C), one day in the extract form (at 16 °C), one year in tissue (at −80 °C), and after three freeze–thaw cycles. The calculated mean carry-over of **NMD**, determined from **NMD**-free brain samples measured after the highest calibration points, was also found to be negligible (0.07%). Over hundreds of validation runs, no retention time shifting was observed and the retention time of **NMD** was 2.35 ± 0.1 min. The selectivity study confirmed that no significant response attributable to interfering components was observed at the retention time of **NMD** and **NMD-D7** in the blank samples. Overall, the obtained validation parameters certify that our targeted method with the related sample preparation procedure provides a reliable analytical tool to quantify **NMD** in the brain.

4.1.4 Determination of the pharmacokinetic curve of NMD after *in vitro* assays

We set out to explore whether tissue saturation with **NMD** is subject to varying pH conditions. The kinetics of the tissue saturation with **NMD** were characterized at three different pH levels achieved by adjusting the pH of the incubation medium with 1 M of HCl or 1 M of NaOH. The three conditions established were physiological (pH 7.38), acidic (pH 6.50), and alkaline (pH 7.57).

The measured concentration of **NMD** in the brain slice treated for 0.5 min and then rinsed with PBS solution is, according to our assumption, the result of surface adsorption processes. No significant changes were found in adsorbed **NMD** compared to the three pH assays at a 95% confidence level, and the mean concentrations of **NMD** were below 5.5 μg/g brain in each case (**Fig. 21**). The saturation of brain tissues with **NMD** occurs uniformly in 50 min (t_{max}) to reach median **NMD** concentrations of 31.93 (pH 7.38), 46.16 (pH 6.50), and 30.89 μg/g (pH 7.57). Based on the above data, approximately 14% of the total **NMD** content can be assigned to surface binding. This relatively high value might be explained by the strong hydrophobic interaction between the lipophilic **NMD** and the lipid-rich brain tissue. By studying the effect of the brain tissue pH on **NMD** absorption, no significant differences were found in the analysis of variance (ANOVA) analysis conducted to compare the experimental conditions in the time range of 50–60 min (**Table S2**). During the time-dependent examination of **NMD** concentrations during a given pH treatment, no significant differences were found in any experimental arrangements when analyzing the concentrations obtained at 50 and 60 min, as shown in **Fig. 21**. It can be summarized that at all three pH values, the plateau of the kinetic curve is located in the 50–60 min time interval. The statistical analysis of the obtained concentrations confirmed that no chemical degradation of **NMD** was observed as the treatment time progressed.

Overall, the development of a high-throughput targeted LC–MS/MS method and the optimization of the corresponding sample preparation resulted in a validated analytical workflow that was successfully applied to monitor **NMD** saturation in *in vitro* brain tissue samples. In summary, the pharmacokinetic profile indicates that brain tissue saturation with **NMD** occurs within 50 min at 10 μM, independent of pH. **NMD** levels remained stable between 50–60 min across three different pH conditions, while the *in vitro* model also revealed notable adsorption of lipophilic **NMD** to lipid-rich brain tissue.

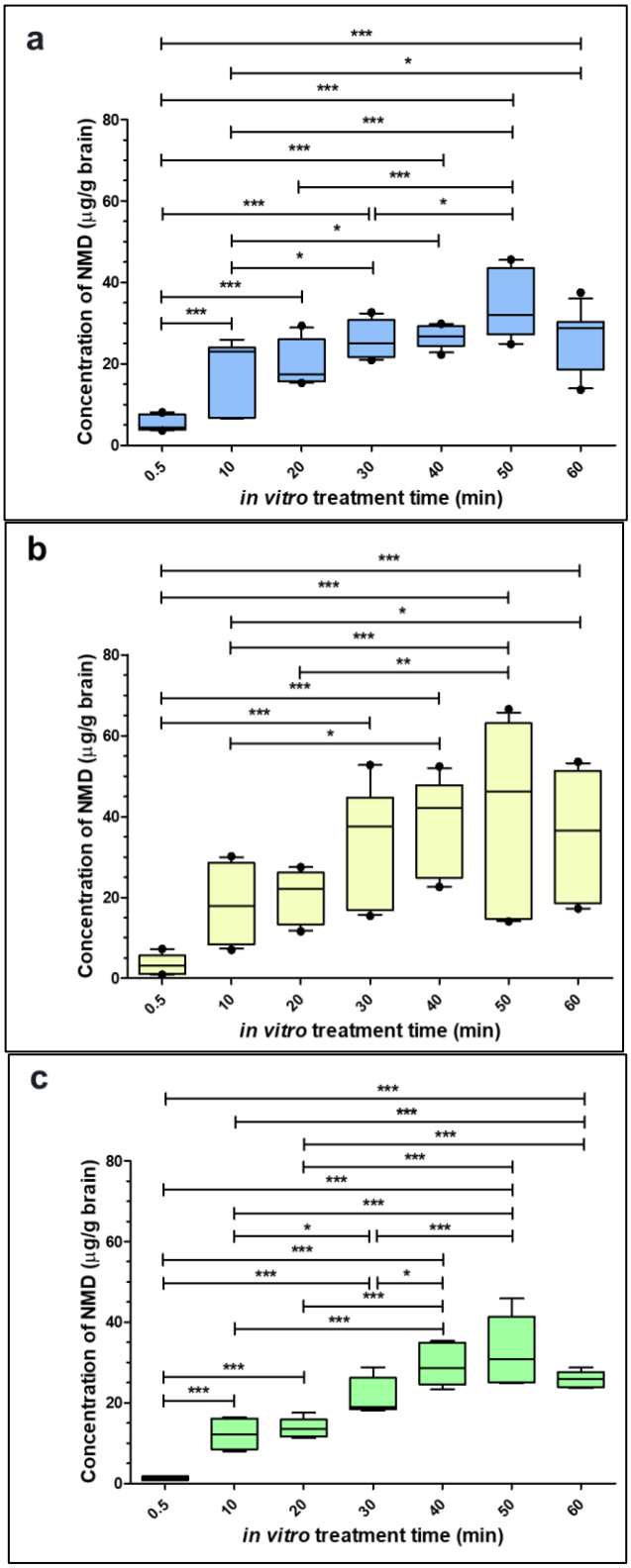

Fig. 21. (A) Pharmacokinetic curve of **NMD** in brain slices (pH: 7.37, n = 3). (B) Pharmacokinetic curve of **NMD** in brain slices (pH: 6.50, n = 3). (C) Pharmacokinetic curve of **NMD** in brain.

4.2 Phenanthrenes

4.2.1 Investigation of phenanthrenes fragmentation behavior

This chapter aims to present the application of UHPLC–MS/HRMS technique in the qualitative and quantitative analysis of phenanthrenes in plant extracts. The first step involved investigating the behavior of phenanthrenes in mass spectrometry. For studying the effect of ESI polarity on the ionization behavior of phenanthrenes, **Compound 3** exhibited significantly higher ionization efficiency in negative ionization mode than in positive ionization mode (**Figs. S4–5**). The ionization of phenanthrenes is more favorable in negative ESI than in positive mode because of the essential presence of phenolic hydroxy group(s) and the lack of a relatively easily protonable functional group. The phenanthrenes ionization behavior in the negative mode is also supported by the reported pKa values of the structurally similar 1-, 2-, 3-, and 4-phenanthrol regioisomers (pKa=11.04, 11.04, 11.00, and 11.82, respectively), which are consistent with phenolate-type ion formation under ESI conditions [93]. Therefore, the negative HESI mode was selected to characterize phenanthrenes by direct infusion with HRMS and MS/HRMS. The fragmentation behavior of phenanthrenes was studied based on their predicted chemical composition obtained with less than 5 ppm accuracy from the obtained MS/HRMS spectra. In the proposed structures of the most abundant fragment ions, the negative charge was assumed to be localized on the phenolate group. These findings further support the formation of stable phenolate-type ions in negative ionization mode.

For the precursor ions of **Compounds 2–4** and **6**, an unusual fragmentation pattern was observed. As the collision energy (CE) increased, new fragment-ion peaks emerged within a 1–9 Da mass range relative to the isolated precursor ion, and adjacent ions differed by 1 Da (**Figs. 22- 25; Table S3**). In the case of **Compound 4**, this characteristic pattern, shown in **Fig. 26A and B,** is described here as an “organ pipe distribution.” The shape of this distribution changed continuously as CE increased. **Figure 26C** further demonstrates the effect of CE on the relative abundance of fragment ions formed via H• loss and other parallel fragmentation pathways. This can be explained by the serial loss of the hydrogen radical (H•), which still resulted in fragment ions with a single negative charge [94].

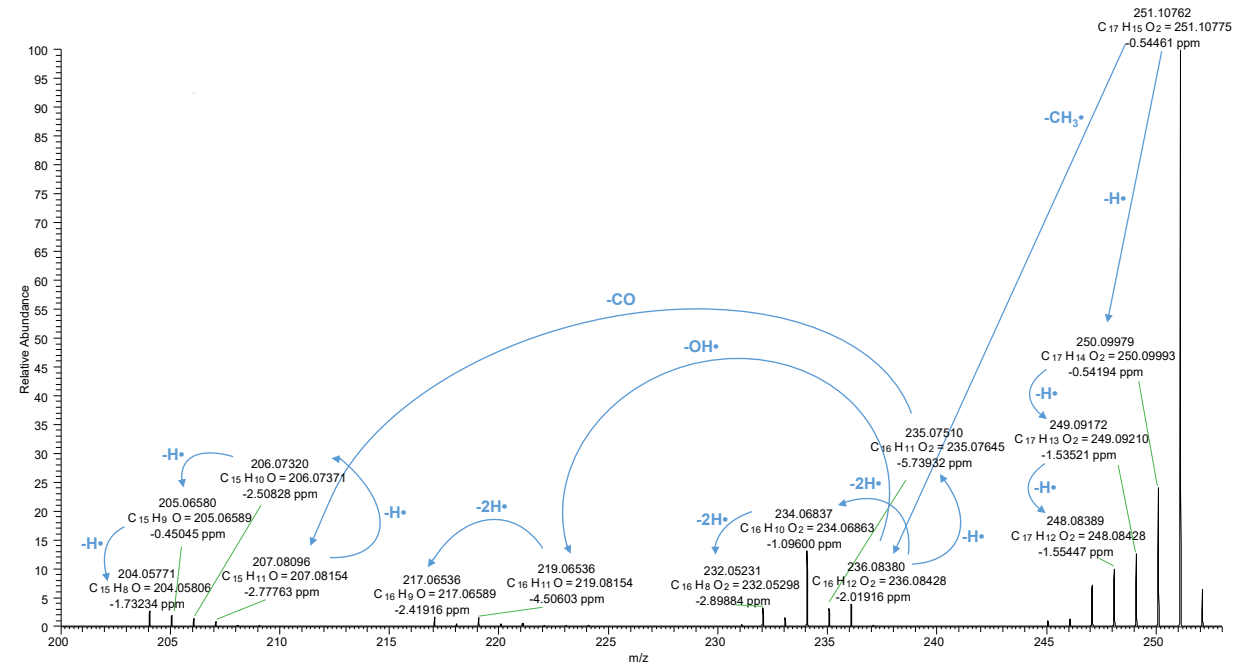

Fig. 22. MS/HRMS (CE range: 10-100 eV) spectrum of **Compound 2** in direct infusion negative HESI mode.

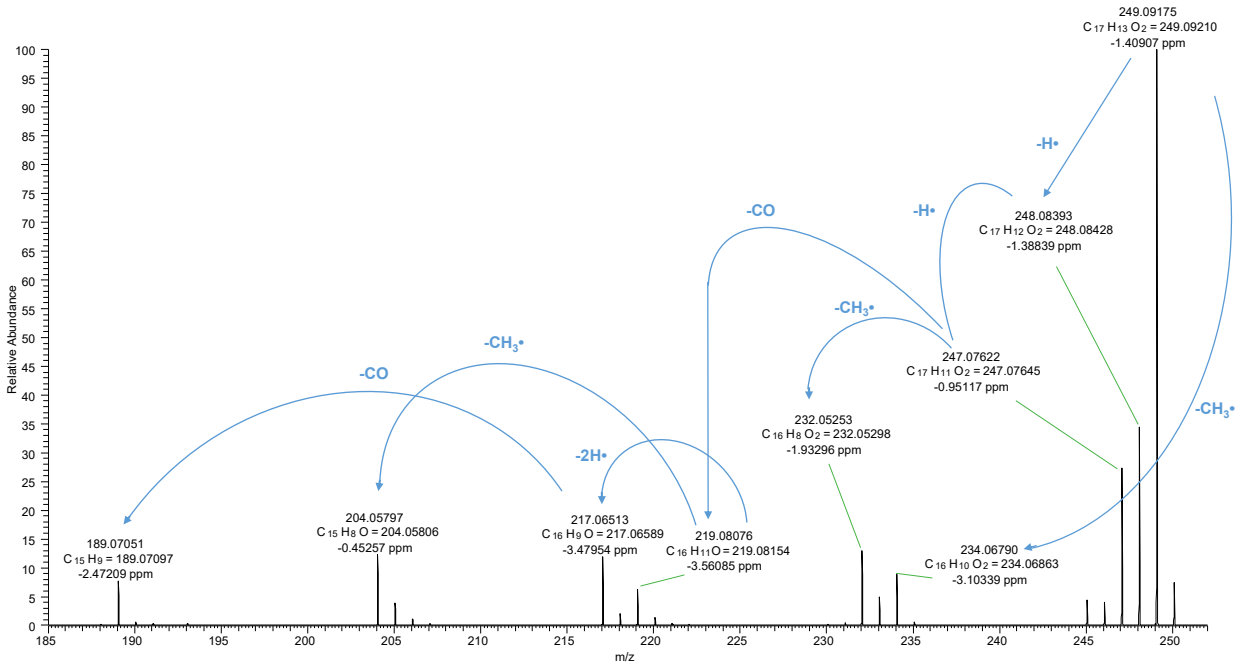

Fig.23. MS/HRMS (CE range: 10-100 eV) spectrum of **Compound 3** in direct infusion negative HESI mode.

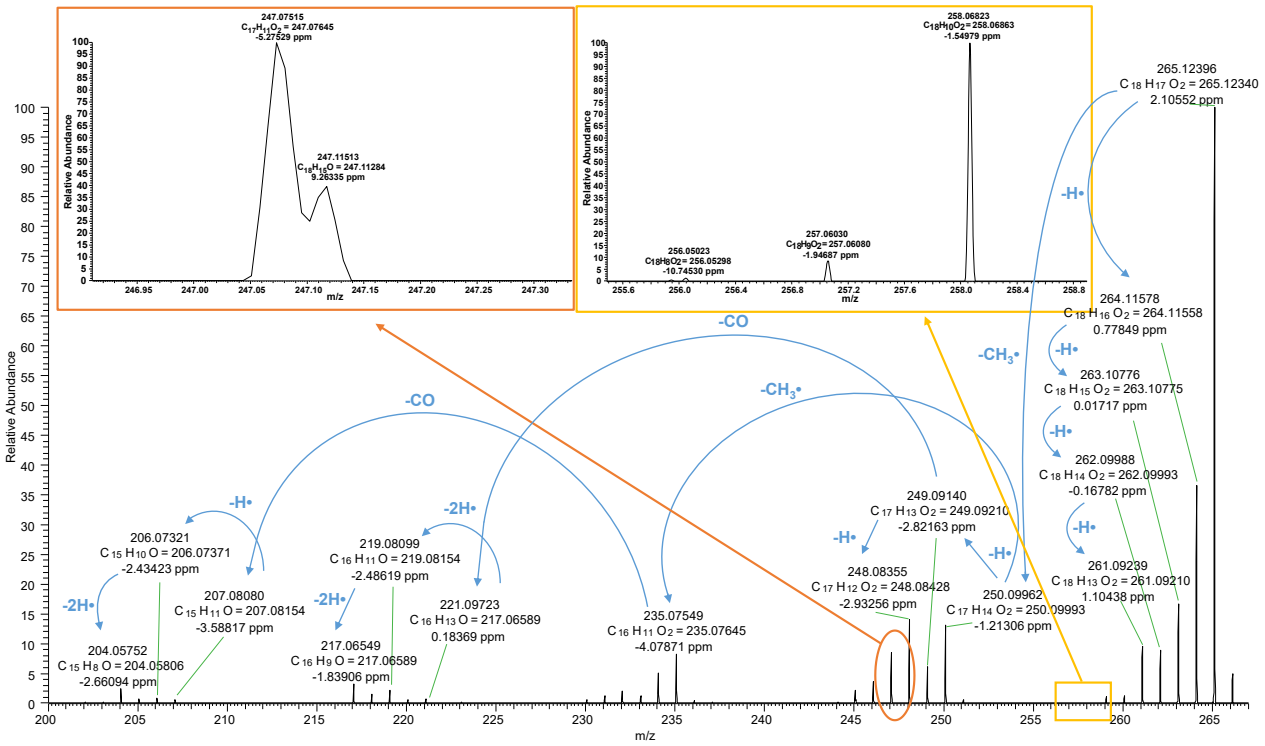

Fig. 24. MS/HRMS (CE range: 10-100 eV) spectrum of **Compound 4** in direct infusion negative HESI mode.

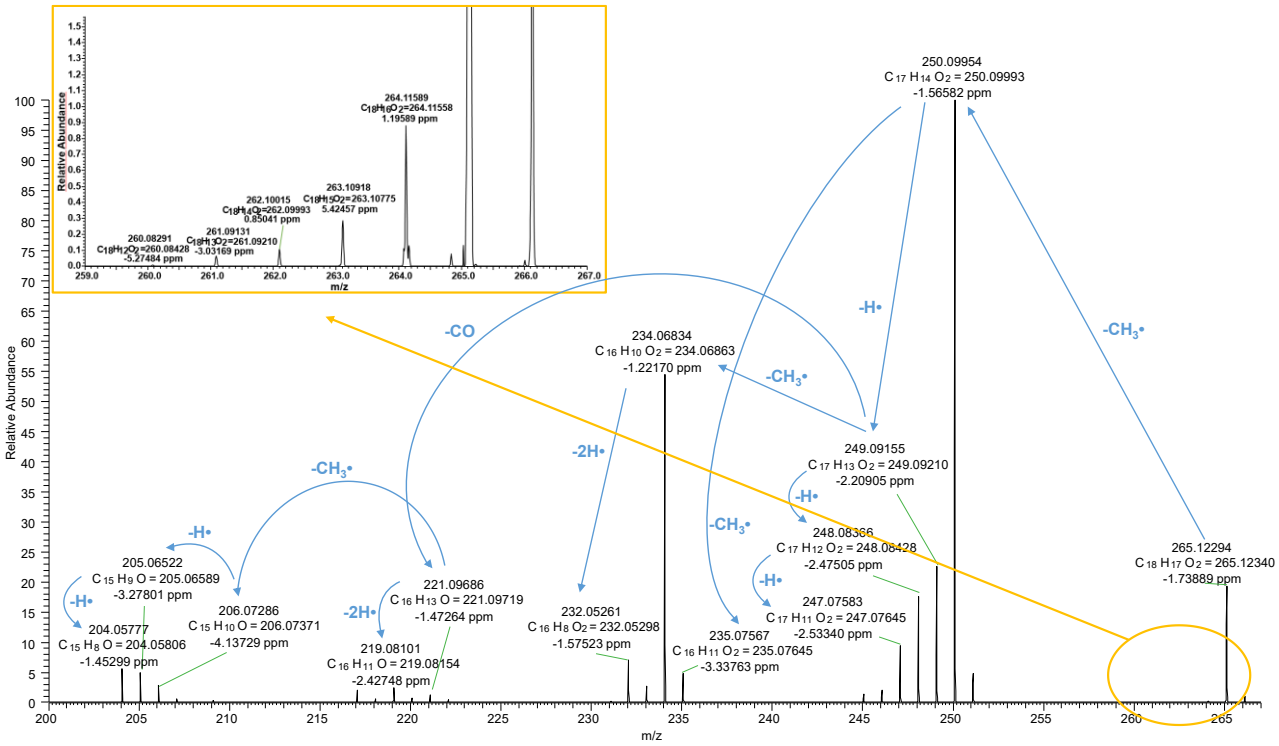

Fig. 25. MS/HRMS (CE range: 10-100 eV) spectrum of **Compound 6** in direct infusion negative HESI mode.

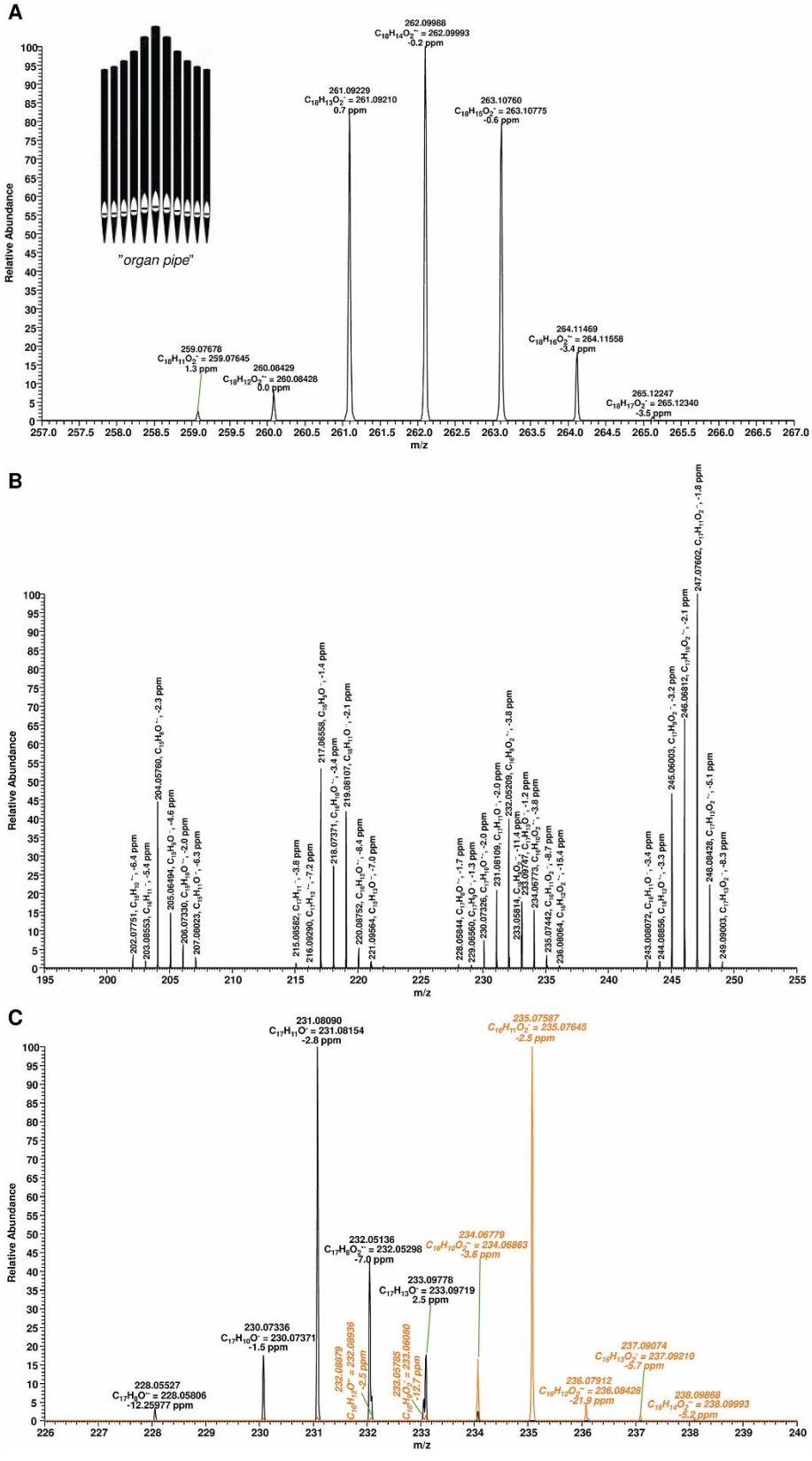

Fig. 26. The "*organ pipe distribution*" of precursor ion (A), fragment ions (B), and overlapped fragment ions (C) of **Compound 4** with related molecular compositions and mass accuracies, obtained by direct infusion HESI-MS/HRMS measurement at 49 (A), 70 (B), 36 (C orange), and 85 (C black) eV labeling molecular composition and mass accuracy.

This fragmentation behavior was also observed in the remaining **Compound 1** and **7** fragment ions but not their precursor ions (**Figs. 27 and 28**). For **Compound 7**, the loss of methyl radical (CH_3•), the produced fragment ions showed the "organ pipe distribution" too. It is assumed that CH_3• exits from the ether bond first, and the produced fragment ion, with a structure similar to negatively charged **Compound 4,** after H• loses. A similar behavior was observed in **Compound 6**, resulting in negatively charged **Compound 2** with an exit of H•, indicating that the methyl radical exits from the ether bond first (**Fig. 25**). The "organ pipe distribution" was also observed for the fragment ions of all investigated phenanthrenes (**Fig. 26B–C**, **Figs. 22–28**). While these fragment ions could be produced by the related 1–9 Da shifted precursor ion–radicals, the fragment ions could also undergo H• loss, yielding the precursor ions of **Compounds 4, 6**, and **7**. For isoflavonoids, the formation of radicals during the fragmentation process was also observed, but without this unique distribution [95].

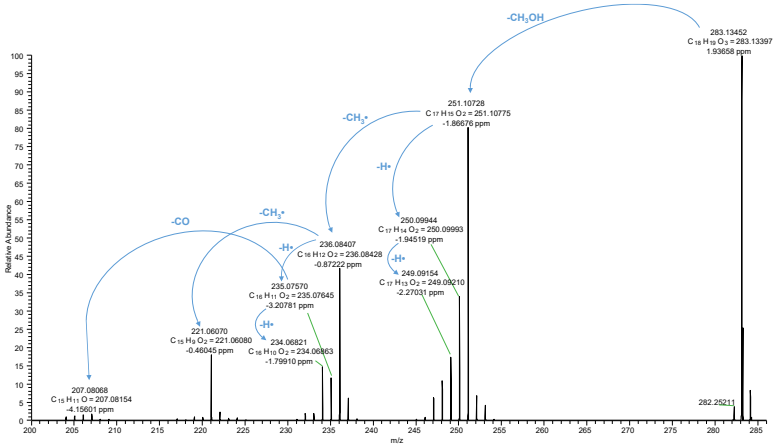

Fig.27. MS/HRMS (CE range: 10-100 eV) spectrum of **Compound 1** obtained in direct infusion negative HESI mode.

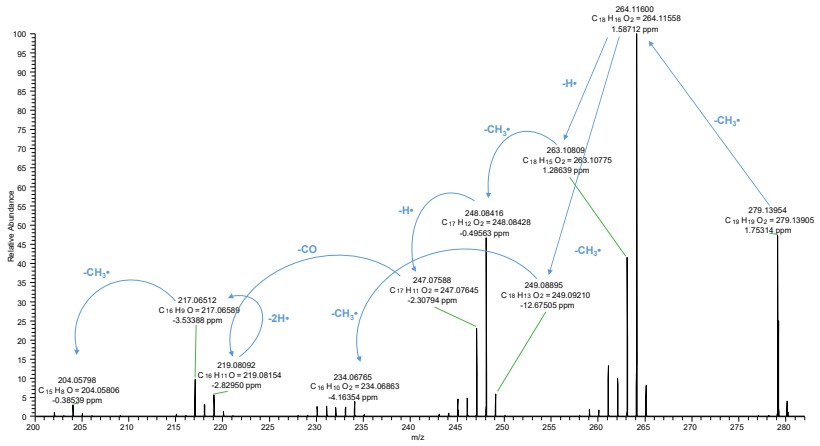

Fig. 28. MS/HRMS (CE range: 10-100 eV) spectrum of **Compound 7** in direct infusion negative HESI mode.

To identify the bonds responsible for the "organ pipe"-like fragmentation distribution of **Compound 2**, quantum chemical calculations were performed using a stepwise approach, enabling the identification of the most likely fragmentation pathway. Initially, the BDEs of X─H (X = C,O) bonds were determined following O(15) deprotonation (refer to **Fig. 29** for atom numbering). The MN15 density functional and 6-31G + (d,p) basis set were utilized [96,97]. The lowest BDE from the mentioned values was applied to detect the initial step with the highest probability along the fragmentation pathway. The identical process was reiterated for the ensuing fragment to determine the second step, and so forth. The BDE values assessed for these subsequent steps are compiled in **Table S4. Fig. 29** presents the minimum BDE values obtained for each calculation, alongside their corresponding bonds (specifically, O(15)─H, C(19)─H, C(7)─H, and C(8)─H). A distribution pattern like the "organ pipe distribution" was also observed for **Compounds 1** and **6**. The calculation results of **Compound 1** BDEs showed that the preferred initial fragmentation pathway involves the elimination of neutral CH3OH (refer to **Fig. 29 and Table S5**). The resulting fragment ions resembled the deprotonated form of **Compound 2**. For **Compound 6**, the first step of its likeliest fragmentation pathway is the loss of a CH3• radical that produces the same remaining fragment, as observed for **Compound 2**, after the loss of an H• radical originally bound to O(15) (refer to **Fig. 29**). To determine the source of the "organ pipe distribution" detected for **Compounds 1** and **6**, the BDE calculations were utilized for **Compound 2** (**Fig. 29**).

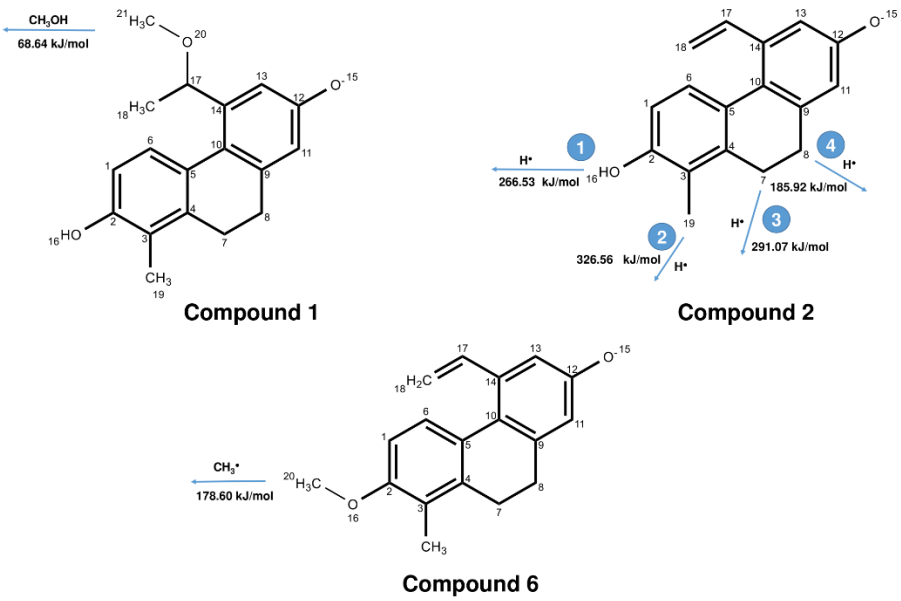

Fig. 29. The initial steps of the likeliest fragmentation pathway of **Compounds 1**, **2,** and **6** derived from the calculated bond dissociation energies after O(15) deprotonation using the MN15 density functional and MN15/6-31G + (d,p) basis set.

Like the alkyl-substituted phenol derivatives, the most abundant fragment ions were formed by *β*-carbon cleavage through methyl radical (15.02348 *m/z*) loss for **Compounds 6** and **7** containing a methyl ether bond (**Fig. 25, Fig. 28**). The presence of an additional double bond in the B ring of **Compound 3** compared to the other compounds resulted in full conjugation of the molecule (**Fig. 11**). The formation of this fully aromatic system can be a force driving the fragmentation process of the investigated phenanthrenes through hydrogen radical loss (**Fig. 29**). The calculated bond lengths following the exit of the four hydrogen radicals support this phenomenon for **Compound 2** (see **Fig. 30**).

As reported for isoflavonoids, this may contribute to forming the most abundant fragment ion with a 45.03459 Da shift from the precursor ion via methyl radical and neutral loss of CH_2O, followed by ring-closing, to provide a completely conjugated condensed ring [98]. For **Compounds 2** and **4**, another fragmentation pathway was more favored (**Fig. 22, Fig.24**). The observed 17.03984 Da decrease might be explained by a methyl radical (15.02348 Da) loss followed by the homolytic cleavage of two carbon–hydrogen bonds, resulting in the exit of 2H• (2 × 1.00782 Da) with a total theoretical mass reduction of 17.03912 Da. For dyes with a structure similar to that of phenanthrene, the 17 Da difference was explained only by the loss of hydroxyl radical (HO•) (theoretical mass of 17.00274 Da) based on low-resolution MS/MS measurement [98]. However, our accurate MS/HRMS results also identified an alternative fragmentation pathway for phenanthrenes. Interestingly, overlapped fragment ions with "organ pipe distribution" appeared at 233 *m/z* with approximately 0.04 *m/z* differences **(Fig. 26-C**). The suggested molecular formulas are $C_{16}H_9O_2^-$ and $C_{17}H_{13}O^-$; the former ion can be formed by $2CH_3$• and 2H• exit from **Compound 4** ($C_{18}H_{17}O_2$) precursor ion, while the latter structure can be explained by H_2O and CH_3• cleavage, which are confirmed by the presence of overlapped 247.07515 *m/z* ($C_{18}H_{17}O_2^-$–CH_3•–3 H•) and 247.11513 *m/z* ($C_{18}H_{17}O_2^-$–H_2O) peaks (**Fig. 24**). Interestingly, the formation of the quantifier ions of Compounds 1 and 5 triggered different fragmentation behaviors. For **Compound 1**, the 32.02640 Da mass loss resulted from the exit of neutral MeOH (32.02621 Da) through homolytic or heterolytic dissociation, resulting in a new double bond (**Fig. 27**). This observed deviation compared to **Compound 6** (phenol ether group) might be explained by the position of the ether bond (**Fig.11**). The oxygen of the ether group in **Compound 1** is attached to a secondary sp3 carbon atom. Thus, the radical or carbocation formed by either homolytic or heterolytic cleavage can be stabilized more efficiently compared to when the ether group is linked to the sp2 hybridized carbon atom. Moreover, forming a new double bond to extend the existing conjugation system works as a driving force of the mechanism. For **Compound 5**, the observed 20.02701 Da loss can be attributed to the exiting groups HO• and 3 × H• in the case of the assumed homolytic bond breakage (**Fig. 31**). According to our

theory, the driving force of this fragmentation is the development of full conjugation of the resulting structure. Certainly, another mechanism might also occur that involves heterolytic bond rupture. The homolytic dissociation mechanism might be energetically favored due to aromatic ring stabilization. While the radical fragment ions often have even m/z values, the fragment anions of phenanthrenes have odd m/z values. For instance, the radical loss of a radical gave an anion, and vice versa. For targeted UHPLC-MS/HRMS analysis of phenanthrenes, the selection of appropriate transitions for quantitation (quantifier ion) and confirmation (qualifier ion) was based on spectra obtained via CE collision energy optimization (**Fig. 11**).

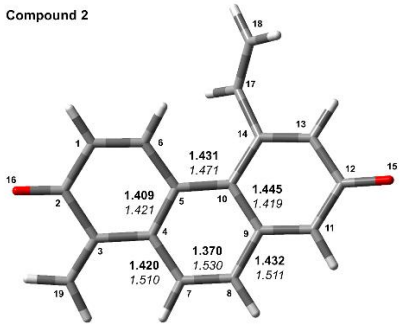

Fig. 30. The calculated bond lengths for the B ring of negatively charged (on O(15)) **Compound 2** (italic) and its fragment ion (bold) that were obtained by the exit of the four H radicals according to the proposed fragmentation pathway of the parent compound (see **Fig. 22**). The optimized chemical structures were calculated using MN15 density functional and MN15/6-31G + (d,p) basis set. The bond length values are shown in Angstrom.

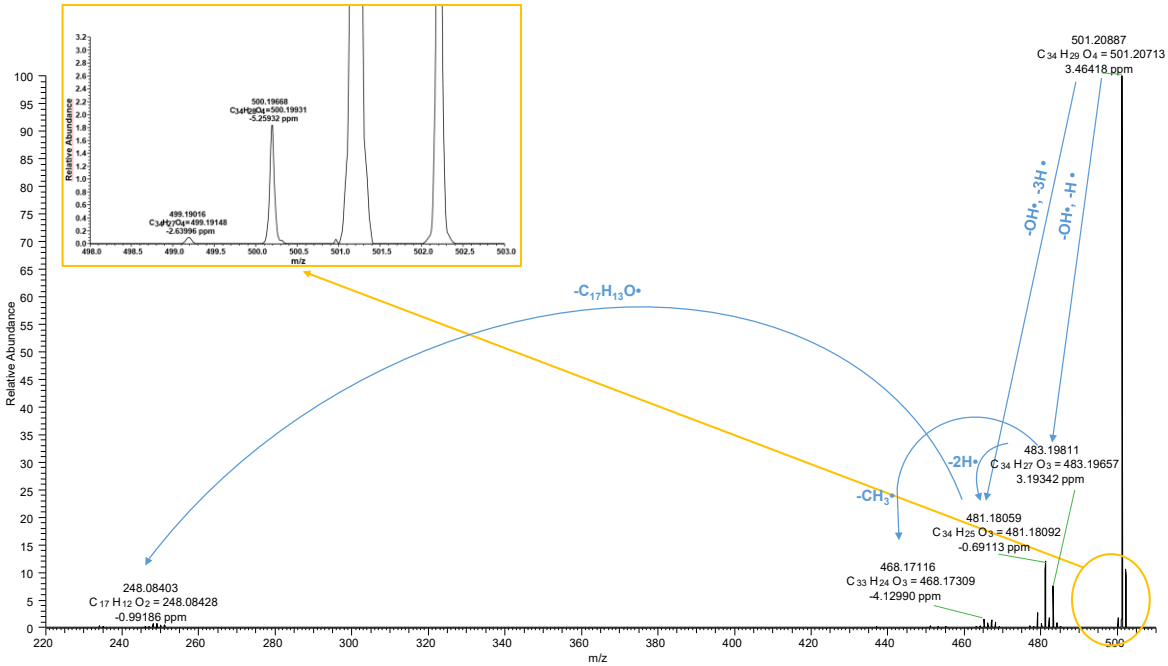

Fig. 31. MS/HRMS (CE range: 10-100 eV) spectrum of **Compound 5** in direct infusion negative HESI mode.

4.2.2 UHPLC-MS/HRMS analysis of phenanthrenes

In the method development, maintaining the total run time below 15 min was considered an important aspect besides suitable separation. To study the chromatographic behavior of structurally similar phenanthrenes, narrow-bore columns (2.1 mm) with lengths of 50, 100, and 150 mm were tested. The applied gradient program started with 30 % ACN and reached 100 % ACN within 3.5 min, followed by column washing and equilibration. To avoid the peak broadening effect of the injected volume, a uniform 2 µL of 5 µM standard mixture was injected. A flow rate of 0.4 mL and a column temperature of 50 °C were selected to obtain appropriate retention of the targeted analytes. By setting the initial UHPLC conditions, the HESI source was optimized for phenanthrenes using a flow-injection procedure with a T-mixer. For the HESI-MS/HRMS detection of phenanthrenes, the quantifier ions were monitored during method development.

Relative to the 100-mm-length column, the highest retentions were observed on the HSS T3 column, while the use of Kinetex Biphenyl provided the lowest retention times (**Fig. S6–10**). **Compounds 7** and **6** eluted with the highest retention times, probably due to the presence of a single phenolic hydroxyl group compared with other phenanthrenes having 2 or 4 aromatic hydroxy groups. For instance, even for **Compound 5**, a dimer of **Compound 2** containing six rings, lower retention times were observed than for **Compounds 7** and **6** highlighting the importance of phenolic hydroxyl groups for the retention mechanism. For **Compound 1**, the presence of a 1-methoxyethyl group instead of a vinyl group at C-5 afforded the lowest retention. Steric hindrance between the analyte and solid phase may have triggered this observation. Baseline separation was achieved for all phenanthrenes except for **Compounds 2** and **3**, which differed in only one double bond. To improve the separation, phenanthrenes were investigated on Accucore C30 with a 150 mm column. As expected, higher retention with improved resolution was obtained with the C18 columns compared with the C18 columns. Interestingly, for C30, the narrowest chromatographic peak width was observed despite a longer column and higher retention (**Fig. S11**). To shorten the analysis time, a 50 mm PFP column was tested using the same gradient. Besides the expected lower retention time, the separation efficiency was significantly lower without peak width improvement (**Fig. S12**). To obtain better chromatographic parameters, Accucore C30 was selected for further chromatographic optimization. By slight modification of the gradient program, baseline separation within 4 min was obtained for targeted phenanthrenes, except for **Compounds 2** and **3** (**Fig. 32**). The internal standard semisynthetic phenanthrene (**IS**) eluted in the middle of the analysis time (RT = 3 min).

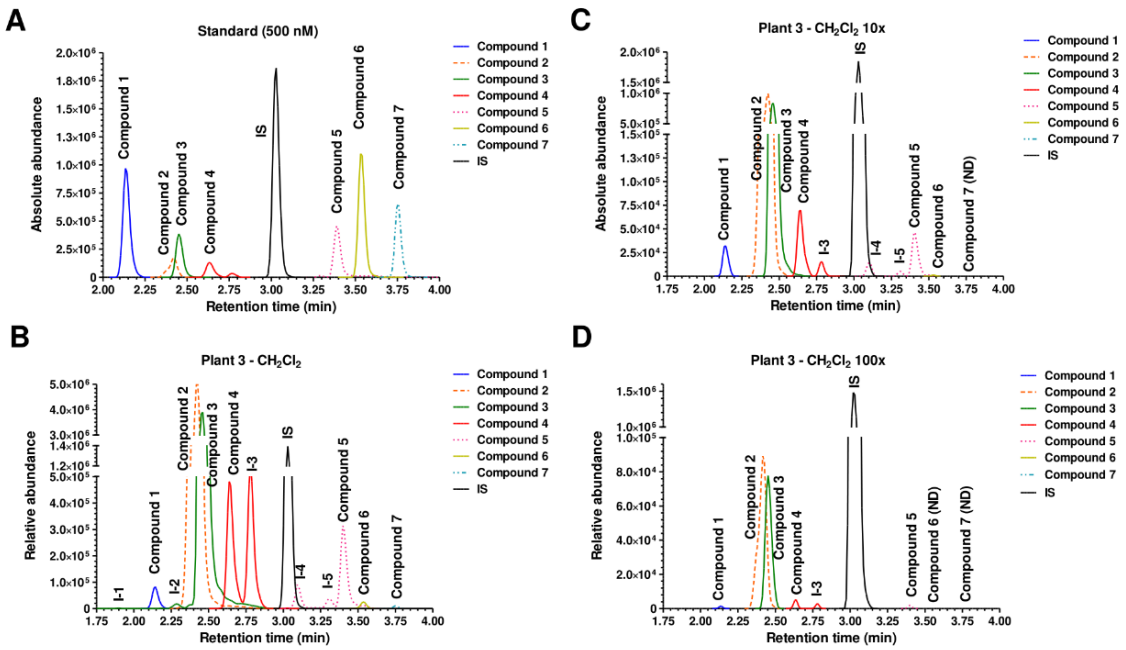

Fig. 32. Extracted ion chromatogram of targeted phenanthrenes and their isomers in (A) 500 nM calibration sample, (B) 0.1 mg/mL CH_2Cl_2 fraction from Plant 3, (C) tenfold- and (D) hundredfold-diluted CH_2Cl_2 fraction of Plant 3 obtained by UHPLC–MS/HRMS method.

4.2.3 Obtained validation parameters of targeted UHPLC–MS/HRMS method

The investigation of the validation parameters is crucial for the applicability of the new method from a quantitative aspect. For the quantitation of phenanthrenes, the developed UHPLC-MS/HRMS method was validated by determining the limit of linearity, limit of detection (LOD), lower limit of quantitation (LLOQ), accuracy, precision, carry-over, and retention stability. The obtained validation results are summarized in **Table S6**. The limits of linearities were found to be in the concentration range from 10 to 5000 nM for **Compounds 1, 3**, and **6** while 25-5000 nM for **Compounds 2, 4, 5**, and **7**. The coefficients of determination (R^2) were greater than or equal to 0.99 in all cases. The linear 1 x-1 weighting calibrations were used, except for **Compound 5**. The calculated LODs yielded a concentration range of 4.65–16.03 nM. The obtained bias values fell within the accepted ±20 % bias range at LOW, MID, and HIGH concentration levels. The precision and accuracy values were below 20% (1.4–16.4%) in the coefficient of variation (CV). To obtain valid analytical results, the stability of the targeted compound is an important aspect of the prepared samples. The one-day autosampler stability obtained at three concentrations confirmed that analyte losses were below 20%. The contributions of MeOH and CH_2Cl_2 extracts for the matrix effects of targeted analytes were comparable at the three dry extract concentrations in the LLOQ, LOW, MID, and HIGH concentration levels investigated (see **Table S7**). Repeated freezing and thawing up to 5

cycles did not affect the targeted analyte concentrations. The carry-over values of phenanthrenes obtained by injections of blank samples after the highest calibration points were below 0.001%. The retention time shifting was < 0.2 min. In summary, the validation parameters obtained demonstrate that our UHPLC-MS/HRMS method is an efficient analytical tool for quantifying phenanthrenes.

4.2.4 Quantitation of phenanthrenes in *Juncus compressus*

As an application of the developed analytical method, all seven phenanthrenes were quantified in *J. compressus*. The semi-targeted approach was applied to identify additional phenanthrene isomers beyond the targeted analytes. The fragment ions were PRM-monitored for each standard in the 1.5–5 min time range. Due to the relatively low scan rate of the applied Orbitrap instrument, two PRM methods were used to obtain the required scan numbers. One of them was optimized for quantifier ions, while the other for qualifier ions. The former provided information for quantitation, while the latter was used for confirmation of given analytes.

By this semi-targeted approach, five new isomers were identified, namely I-1, I-2 (isomers of **Compound 3**), I-3 (isomer **Compound 6** or **Compound 4**), as well as I-4 and I-5, the isomers of **Compound 5**. The obtained MS/HRMS spectra compared with the related standard are illustrated in (**Fig. S13-31**). According to the obtained MS/HRMS spectra of new isomers, the precursor ions I-1, I-2, and I-3 showed the "organ pipe distribution" and lack of 15 Da loss indicated the presence of two phenolic groups. The comparison of MS/HRMS spectra of I-3, **Compound 4** (two phenolic groups), and **Compound 6** (one phenolic group) reveals the structural similarity between I-3 and **Compound 4**. The fragmentation patterns of I-4 and I-5 were found to be in agreement with **Compound 5**, suggesting the existence of free phenolic groups.

Given the wide concentration range of the targeted phenanthrenes, a dilution series approach was used to quantify the targeted analytes. The minor components **Compounds 1, 6**, and **7** were quantified in the 0.1 mg/mL dry extract (MeOH) samples, while the concentrations of **Compounds 2** and **3** were determined in the samples diluted tenfold and hundredfold. The obtained quantitative results are summarized in **Table 1**. The comparison of the phenanthrene concentration (nmol g-1) in MeOH and CH_2Cl_2 extracts affirmed that the latter provided higher enrichment for **Compounds 1-5**. However, **Compound 6** and **Compound 7**, containing a methylether group instead of a phenolic hydroxyl group, exhibited higher enrichment in the MeOH phase assuming their better solubility in the polar protic organic solvent. Additionally, no significant differences were observed in concentration values normalized to plant dry weight between the two extracts, except when the phenanthrene content of the MeOH extract was close to or below the detection limit. The **Compound 2** was represented in the highest concentration in the plants, especially in Plant 1 and

Plant 3, with values over 2300 nmol g-1. This value is significantly higher when compared to those in Plants 2, 4, and 5 (**Fig S32**). **Compound 3** was the second most abundant (~ 1000 nmol g^{-1}) phenanthrenes in Plants 1 and 3 which, again, is a significant difference in comparison with the other Plants. Considering the other examples of the concentration scale, **Compound 1** was quantified in the undiluted CH_2Cl_2 extracts of Plants 1, 3, and 5 at 4.15, 4.73, and 3.10 nmol g-1, respectively. According to the ANOVA analysis of quantitative data, 3 groups with similar phenanthrene profiles can be distinguished: Plants 1–3, Plants 2–4, and Plant 5, based on their geographical location (**Fig. S32**). In summary, the structural background underlying the distinctive fragmentation behavior, "organ pipe distribution", of phenanthrenes, was elucidated. Moreover, the newly developed UHPLC–MS/HRMS method enabled the identification of additional phenanthrene isomers. Considering the high concentration range of the targeted phenanthrenes, the dilution series approach was successfully applied for their quantitation in methanolic and CH_2Cl_2 extracts. Based on ANOVA evaluation of the quantitative data, three distinct groups with similar phenanthrene profiles were identified—Plants 1–3, Plants 2–4, and Plant 5—reflecting their geographical locations (**Table 1, Fig. S32**).

Table 1. The obtained phenanthrenes concentrations in the measured samples and the dried plants from methanol and dichloromethane fractions.

Location	Sample	Fraction	Dilution	Compound 1		Compound 2		Compound 3		Compound 4		Compound 5		Compound 6		Compound 7	
				nmol L^{-1} in measured sample	nmol g^{-1} dried plant	nmol L^{-1} in measured sample	nmol g^{-1} dried plant	nmol L^{-1} in measured sample	nmol g^{-1} dried plant	nmol L^{-1} in measured sample	nmol g^{-1} dried plant	nmol L^{-1} in measured sample	nmol g^{-1} dried plant	nmol L^{-1} in measured sample	nmol g^{-1} dried plant	nmol L^{-1} in measured sample	nmol g^{-1} dried plant
Békéscsaba	**Plant 1**	**MeOH**	-	< LLOQ	**< LLOQ**	2233	**3591**	804.8	**1295**	215.5	**347.4**	63.29	**101.3**	70.65	**114.2**	127.8	**205.8**
			10x	-	-	174.2	2801	66.11	1063	-	-	-	-	< LOD	< LOD	< LOD	< LOD
			100x	-	-	-	-	< LOD	< LOD	-	-	-	-	-	-	-	-
		CH_2Cl_2	-	34.83	**4.150**	ULOQ	ULOQ	ULOQ	ULOQ	2308	**273.7**	608.5	**72.09**	< LOD	**< LOD**	-	**-**
			10x	-	-	2156	**2557**	776.5	**920.7**	225.4	267.3	58.24	69.01	-	-	-	-
			100x	-	-	195.2	2312	70.41	834.9	-	-	-	-	-	-	-	-
Kiszombor	**Plant 2**	**MeOH**	-	-	-	316.2	**453.3**	105.5	**150.6**	-	-	< LLOQ	**< LLOQ**	33.99	**48.77**	37.55	**54.51**
			10x	-	-	< LLOQ	< LLOQ	< LOD	< LOD	-	-	-	-	-	-	-	-
			100x	-	-	-	-	-	-	-	-	-	-	-	-	-	-
		CH_2Cl_2	-	< LOD	**< LOD**	ULOQ	ULOQ	987.6	**120.4**	215.9	**26.31**	165.7	**20.22**	< LOD	**< LOD**	-	**-**
			10x	< LOD	< LOD	351.2	**427.9**	111.0	135.2	< LLOQ	< LLOQ	< LLOQ	< LLOQ	-	-	-	-
			100x	-	-	<LLOQ	<LOQ	< LOD	< LOD	-	-	-	-	-	-	-	-
Hódmező-vásárhely	**Plant 3**	**MeOH**	-	< LOD	**< LOD**	2153	**3572**	833.0	**1382**	313.4	**519.3**	66.89	**111.2**	139.3	**230.6**	394.8	**655.3**
			10x	-	-	215.7	3578	79.10	1312	-	-	-	-	< LLOQ	< LLOQ	34.34	569.0
			100x	-	-	< LLOQ	< LLOQ	< LOD	< LOD	-	-	-	-	-	-	< LOD	< LOD
		CH_2Cl_2	-	45.83	**4.733**	ULOQ	ULOQ	ULOQ	ULOQ	3361	**345.9**	749.8	**77.18**	< LLOQ	**< LLOQ**	< LLOQ	**< LLOQ**
			10x	< LLOQ	< LLOQ	ULOQ	ULOQ	983.2	**1012**	295.3	303.9	76.30	78.51	< LOD	< LOD	-	-
			100x	< LOD	< LOD	294.6	**3031**	109.7	1129	< LLOQ	< LLOQ	< LOD	< LOD	-	-	-	-
Szeged	**Plant 4**	**MeOH**	-	-	-	485.1	**772.4**	249.5	**398.1**	< LLOQ	**< LLOQ**	< LOD	**< LOD**	41.23	**65.29**	69.02	**109.9**
			10x	-	-	< LLOQ	< LOQ	< LLOQ	< LLOQ	-	-	-	-	< LOD	< LOD	-	-
			100x	-	-	-	-	-	-	-	-	-	-	-	-	-	-
		CH_2Cl_2	-	< LLOQ	**< LLOQ**	ULOQ	ULOQ	3207	**277.2**	763.0	**65.94**	208.3	**17.98**	< LOD	**< LOD**	-	**-**
			10x	-	-	773.4	**668.4**	412.3	356.3	71.77	62.06	< LLOQ	< LLOQ	-	-	-	-
			100x	-	-	78.43	677.9	38.02	328.6	-	-	-	-	-	-	-	-
Iván	**Plant 5**	**MeOH**	-	< LOD	**< LOD**	1149	**1257**	407.4	**445.1**	64.77	**71.09**	< LLOQ	**< LLOQ**	286.5	**313.9**	304.5	**333.6**
			10x	-	-	114.6	1253	40.18	439.7	-	-	-	-	28.69	313.9	< LLOQ	< LLOQ
			100x	-	-	-	-	< LOD	< LOD	-	-	-	-	-	-	-	-
		CH_2Cl_2	-	43.28	**3.103**	ULOQ	ULOQ	4114	**296.9**	709.0	**51.16**	547.7	**39.55**	< LLOQ	**< LLOQ**	-	**-**
			10x	< LLOQ	< LLOQ	1452.3	**1048**	491.1	354.4	83.99	60.62	54.06	39.04	< LOD	< LOD	-	-
			100x	-	-	154.2	1112	51.26	369.9	-	-	-	-	-	-	-	-

5. Summary

In this work, a fast and targeted UHPLC–MS/MS method, together with a liquid–liquid extraction procedure, was developed, validated, and applied for the sensitive and selective quantitation of nimodipine (**NMD**) in brain tissue within a total run time of 5 min. The method required only a small amount of brain tissue and yielded higher recovery values than previously reported analytical methods for brain analysis. Quantitation of **NMD** was performed using matrix-matched external calibration with internal standard normalization by **NMD-D7**. The developed method was successfully applied to monitor **NMD** concentrations in acute brain slice preparations, which serve as an experimental model of cerebral ischemia.

To the best of our knowledge, this was the first study to investigate the pharmacokinetics of **NMD** in acute rat brain slice preparations using a targeted UHPLC–MS/MS method. The pharmacokinetic profile showed that brain tissue saturation with NMD was reached within 50 min at a concentration of 10 μM, independent of tissue pH under the *in vitro* conditions used. In addition, **NMD** concentrations remained unchanged between 50 and 60 min at the three investigated pH values. In addition to tissue uptake, the experimental model also showed notable adsorption of the lipophilic **NMD** to lipid-rich brain tissue.

These findings may also be relevant for the targeted delivery of **NMD** to ischemic brain tissue. In previous work, pH-sensitive nanoparticles were shown to be a promising strategy for the selective delivery of **NMD** to tissue at risk of ischemic injury. The present results further support this concept by demonstrating that the acidic tissue environment characteristic of cerebral ischemia does not impair **NMD** uptake into nervous tissue. Overall, one of the main outcomes of this study was the development of an efficient analytical method for **NMD** determination that may be useful not only in research but also in toxicological and forensic applications. In addition, the ionization and fragmentation behavior of seven phenanthrenes was investigated using negative-ion MS/HRMS spectra. Negative electrospray ionization provided higher ionization efficiency than positive mode for these compounds, most likely because the negative charge was preferentially localized on the phenolic group. For **Compounds 1–5**, the MS/HRMS data indicated the presence of two phenolic groups in the precursor ions, and the resulting fragment ions displayed characteristic fragmentation patterns resembling “organ pipe distributions” with increasing collision energy. This behavior could be explained by consecutive hydrogen radical losses, leading to fragment ions carrying a single negative charge. The proposed fragmentation pathways and the origin of this unusual behavior were further supported by quantum chemical calculations. Furthermore, a semi-targeted UHPLC–MS/HRMS method was developed, validated, and applied for the sensitive and selective

quantitation of seven phenanthrenes in plant extracts within a total run time of 11 min. Among the investigated analytes, **Compound 2** and **Compound 3** were the major representatives, whereas **Compound 1** was present at the lowest concentration. In general, phenanthrenes were enriched in the CH_2Cl_2 fraction compared with the MeOH fraction, except for **Compounds 6** and **7**. Another important outcome of this study was the evaluation of the quantitative data by ANOVA, which revealed a phenanthrene fingerprint of *Juncus compressus* extracts associated with geographical origin.

6. References

[1] Li W, Zhang J, Tse FLS. Handbook of LC-MS Bioanalysis: Best Practices, Experimental Protocols, and Regulations. Hoboken (NJ): John Wiley & Sons; 2013.

[2] Pandey S, Pandey P, Tiwari G, Tiwari R. Bioanalysis in drug discovery and development. Pharm Methods. 2010;1(1):14–24. doi:10.4103/2229-4708.72273.

[3] Xu RN, Fan L, Rieser MJ, El-Shourbagy TA. Recent advances in high-throughput quantitative bioanalysis by LC-MS/MS. J Pharm Biomed Anal. 2007;44(2):342–355.

[4] Yuan L, Aubry AF, Ji QC. A simple, effective approach for rapid development of high-throughput and reliable LC-MS/MS bioanalytical assays. Bioanalysis. 2016;8(17):1809–1822.

[5] Peng J, Tang F, Zhou R, Xie X, Li S, Xie F, et al. New techniques of on-line biological sample processing and their application in the field of biopharmaceutical analysis. Acta Pharm Sin B. 2016;6(6):540–551.

[6] Snyder LR, Kirkland JJ, Dolan JW. Introduction to Modern Liquid Chromatography. 3rd ed. Hoboken (NJ): Wiley; 2010.

[7] Fekete S, Schappler J, Veuthey J-L, Guillarme D. Current and future trends in UHPLC. TrAC Trends Anal Chem. 2014;63:2–13.

[8] Loos G, Van Schepdael A, Cabooter D. Quantitative mass spectrometry methods for pharmaceutical analysis. Philos Trans A Math Phys Eng Sci. 2016 Oct 28;374(2079):20150366. doi: 10.1098/rsta.2015.0366.

[9] Fenn JB, Mann M, Meng CK, Wong SF, Whitehouse CM. Electrospray ionization for mass spectrometry of large biomolecules. Science. 1989;246(4926):64–71. doi:10.1126/science.2675315.

[10] Kebarle P, Verkerk UH. Electrospray: from ions in solution to ions in the gas phase, what we know now. Mass Spectrom Rev. 2009;28(6):898–917. doi:10.1002/mas.20247.

[11] Douglas DJ. Linear quadrupoles in mass spectrometry. Mass Spectrom Rev. 2009;28(6):937–960. doi:10.1002/mas.20249.

[12] Yost RA, Enke CG. Triple quadrupole mass spectrometry for direct mixture analysis and structure elucidation. Anal Chem. 1979;51(12):1251–1264. doi:10.1021/ac50048a002.

[13] Hu Q, Noll RJ, Li H, Makarov A, Hardman M, Cooks RG. The Orbitrap: a new mass spectrometer. J Mass Spectrom. 2005;40(4):430–443. doi:10.1002/jms.856.

[14] Peterson AC, Russell JD, Bailey DJ, Westphall MS, Coon JJ. Parallel reaction monitoring for high resolution and high mass accuracy quantitative, targeted proteomics. Mol Cell Proteomics. 2012;11(11):1475–1488. doi:10.1074/mcp.O112.020131.

[15] Rauniyar N. Parallel reaction monitoring: a targeted experiment performed using high resolution and high mass accuracy mass spectrometry. Int J Mol Sci. 2015;16(12):28566–28581. doi:10.3390/ijms161226120.

[16] International Council for Harmonisation of Technical Requirements for Pharmaceuticals for Human Use. ICH guideline M10 on bioanalytical method validation and study sample analysis. 2022.

[17] Carlson AP, Hänggi D, Macdonald RL, Shuttleworth CW. Nimodipine reappraised: an old drug with a future. Curr Neuropharmacol. 2020;18(1):65–82.

[18] Ikawa F, Michihata N, Matsushige T, Abiko M, Ishii D, Oshita J, et al. In-hospital mortality and poor outcome after surgical clipping and endovascular coiling for aneurysmal subarachnoid hemorrhage using nationwide databases: a systematic review and meta-analysis. Neurosurg Rev. 2020;43(2):655–667.

[19] Caylor MM, Macdonald RL. Pharmacological prevention of delayed cerebral ischemia in aneurysmal subarachnoid hemorrhage. Neurocrit Care. 2024;40:159–169.

[20] Frank R, Bari F, Menyhárt Á, Farkas E. Comparative analysis of spreading depolarizations in brain slices exposed to osmotic or metabolic stress. BMC Neurosci. 2021;22:1–10.
[21] Menyhárt Á, Frank R, Farkas AE, Süle Z, Varga VÉ, Nyúl-Tóth Á, et al. Malignant astrocyte swelling and impaired glutamate clearance drive the expansion of injurious spreading depolarization foci. J Cereb Blood Flow Metab. 2022;42(4):584–599.
[22] Back T, Hoehn M, Mies G, Busch E, Schmitz B, Kohno K, et al. Penumbral tissue alkalosis in focal cerebral ischemia: relationship to energy metabolism, blood flow, and steady potential. Ann Neurol. 2000;47(4):485–492.
[23] Katsura K, Asplund B, Ekholm A, Siesjö BK. Extra- and intracellular pH in the brain during ischaemia, related to tissue lactate content in normo- and hypercapnic rats. Eur J Neurosci. 1992;4(2):166–176.
[24] Menyhárt Á, Zölei-Szénási D, Puskás T, Makra P, Tóth OM, Szepes BÉ, et al. Spreading depolarization remarkably exacerbates ischemia-induced tissue acidosis in the young and aged rat brain. Sci Rep. 2017;7(1):1154.
[25] Remzső G, Németh J, Varga V, Kovács V, Tóth-Szűki V, Kaila K, et al. Brain interstitial pH changes in the subacute phase of hypoxic-ischemic encephalopathy in newborn pigs. PLoS One. 2020;15(5):e0233851.
[26] Pignataro G, Simon RP, Xiong ZG. Prolonged activation of ASIC1a and the time window for neuroprotection in cerebral ischaemia. Brain. 2007;130(1):151–158.
[27] Jang IS, Nakamura M, Kubota H, Noda M, Akaike N. Extracellular pH modulation of excitatory synaptic transmission in hippocampal CA3 neurons. J Neurophysiol. 2020;123(6):2426–2436.
[28] Tombaugh GC, Sapolsky RM. Evolving concepts about the role of acidosis in ischemic neuropathology. J Neurochem. 1993;61(3):793–803.
[29] Tóth OM, Menyhárt Á, Frank R, Hantosi D, Farkas E, Bari F. Tissue acidosis associated with ischemic stroke to guide neuroprotective drug delivery. Biology (Basel). 2020;9(12):460. doi:10.3390/biology9120460.
[30] Maurer HH, Arlt JW. Screening procedure for detection of dihydropyridine calcium channel blocker metabolites in urine as part of a systematic toxicological analysis procedure for acidic compounds by gas chromatography-mass spectrometry after extractive methylation. J Anal Toxicol. 1999;23(2):73–80.
[31] Soons PA, Roosemalen MCM, Breimer DD. Enantioselective determination of felodipine and other chiral dihydropyridine calcium entry blockers in human plasma. J Chromatogr B Biomed Sci Appl. 1990;528:343–356.
[32] Watari N, Mizumura J, Higuchi S. Simultaneous microdetermination of nicardipine and its pyridine metabolite in body fluids by capillary column gas chromatography with electron-capture detection. J Chromatogr B Biomed Sci Appl. 1990;530:438–446. doi:10.1016/S0378-4347(00)82347-6.
[33] Mück WM. Enantiospecific determination of nimodipine in human plasma by liquid chromatography-tandem mass spectrometry. J Chromatogr A. 1995;712(1):45–53.
[34] Zhang Q, Jiang X, Wu C. Distribution of nimodipine in brain following intranasal administration in rats. Acta Pharmacol Sin. 2004;25(4):522–527.
[35] Dan Y, Jia Z, Rui L, Zhi H, Jin S. Liquid chromatographic method for determination of free and niosome-entrapped nimodipine in mouse plasma and different tissues. Anal Lett. 2008;41(4):533–542.
[36] López JA, Martínez V, Alonso RM, Jiménez RM. High-performance liquid chromatography with amperometric detection applied to the screening of 1,4-dihydropyridines in human plasma. J Chromatogr A. 2000;870(1–2):105–114.
[37] Isse FA, Le T, Mahmoud SH. Enantioselective assay of nimodipine in human plasma using liquid chromatography-tandem mass spectrometry. Biomed Chromatogr. 2021;35(2):e4971.
[38] Zhou Y, Ma C, Wang Y, Zhang QM, Zhang YY, Fu J, et al. High-performance liquid chromatographic separation of thirteen drugs collected in Chinese Pharmacopoeia 2010 on cellulose ramification chiral stationary phase. J Pharm Anal. 2012;2(1):48–55.
[39] Wang W, Li P, Wu F, Wang Z, Zhang T. Development and optimization of a supercritical fluid chromatography tandem mass spectrometry method for the high-throughput determination of nimodipine in beagle plasma. J Sep Sci. 2019;42(12):2179–2186.
[40] Wang W, Li P, Fang M, Li X, Zhang Y, Zhang T. SFC-MS/MS method for simultaneous determination of nimodipine and 3-n-butylphthalide in beagle plasma: application to pharmacokinetic interaction study. Bioanalysis. 2020;12(21):1509–1519.

[41] Mueller CA, González ABB, Weinmann W. Screening for dihydropyridine calcium channel blockers in plasma by automated solid-phase extraction and liquid chromatography/tandem mass spectrometry. J Mass Spectrom. 2004;39(6):639–646.
[42] Qiu F, Chen X, Li X, Zhong D. Determination of nimodipine in human plasma by a sensitive and selective liquid chromatography-tandem mass spectrometry method. J Chromatogr B. 2004;802(2):291–297.
[43] Zuo J, Cai R, An Y, Tang H. Simultaneous quantification of five stereoisomeric hexoses in nine biological matrices using ultra-high performance liquid chromatography with tandem mass spectrometry. J Anal Test. 2020;4:249–256.
[44] Bai YL, Hong ZD, Zhang TY, Cai BD, Zhang YZ, Feng YQ. A method for simultaneous determination of 14 carbonyl-steroid hormones in human serum by ultra-high performance liquid chromatography-tandem mass spectrometry. J Anal Test. 2020;4:1–12. doi:10.1007/s41664-020-00120-5.
[45] Wang C, Lu X, Li L, Zhang R, Shi T, Li S. Microdialysis combined with liquid chromatography-tandem mass spectrometry for the determination of nimodipine in the guinea pig hippocampus. J Chromatogr B. 2016;1017–1018:226–232.
[46] Li F, Fei Q, Mao D, Si Q, Dai M, Ma Q, Zhang H, Bai L, He N. Comparative pharmacokinetics of nimodipine in rat plasma and tissues following intraocular, intragastric, and intravenous administration. AAPS PharmSciTech. 2020;21:234.
[47] Kovács A, Vasas A, Hohmann J. Natural phenanthrenes and their biological activity. Phytochemistry. 2008;69(5):1084–1110.
[48] Tóth B, Hohmann J, Vasas A. Phenanthrenes: a promising group of plant secondary metabolites. J Nat Prod. 2018;81(3):661–678.
[49] Kúsz N, Stefkó D, Barta A, et al. Juncaceae species as promising sources of phenanthrenes: antiproliferative compounds from Juncus maritimus Lam. Molecules. 2021;26(4):999.
[50] Bús C, Kúsz N, Jakab G, et al. Phenanthrenes from Juncus compressus Jacq. with promising antiproliferative and anti-HSV-2 activities. Molecules. 2018;23(8):2085.
[51] Tóth B, Liktor-Busa E, Urbán E, Csorba A, Jakab G, Hohmann J, Vasas A. Antibacterial screening of Juncaceae species native to the Carpathian Basin against resistant strains and LC-MS investigation of phenanthrenes responsible for the effect. Fitoterapia. 2016;115:69–73.
[52] Percie du Sert N, Hurst V, Ahluwalia A, Alam S, Avey MT, Baker M, Browne WJ, Clark A, Cuthill IC, Dirnagl U, Emerson M, Garner P, Holgate ST, Howells DW, Karp NA, Lazic SE, Lidster K, MacCallum CJ, Macleod M, Pearl EJ, Petersen OH, Rawle F, Reynolds P, Rooney K, Sena ES, Silberberg SD, Steckler T, Würbel H. The ARRIVE guidelines 2.0: updated guidelines for reporting animal research. J Cereb Blood Flow Metab. 2020;40(9):1769–1777.
[53] Menyhárt Á, Farkas AE, Varga DP, Frank R, Tóth R, Bálint AR, Makra P, Dreier JP, Bari F, Krizbai IA, Farkas E. Large-conductance Ca2+-activated potassium channels are potently involved in the inverse neurovascular response to spreading depolarization. Neurobiol Dis. 2018;119:41–52.
[54] Matuszewski BK, Constanzer ML, Chavez-Eng CM. Strategies for the assessment of matrix effect in quantitative bioanalytical methods based on HPLC-MS/MS. Anal Chem. 2003;75(13):3019–3030.
[55] Liu W, Wang R, Hu F, Wu P, Huang T, Fizir M, He H. Novel mixed hemimicelles based on nonionic surfactant-imidazolium ionic liquid and magnetic halloysite nanotubes as efficient approach for analytical determination. Anal Bioanal Chem. 2018;410:7357–7371.
[56] U.S. Food and Drug Administration. Bioanalytical Method Validation: Guidance for Industry [Internet]. 2018 [cited 2024 Apr 22]. Available from: https://www.fda.gov/files/drugs/published/Bioanalytical-Method-Validation-Guidance-for-Industry.pdf
[57] DiLabio GA, Pratt DA, LoFaro AD, Wright JS. Theoretical study of X-H bond energetics (X = C, N, O, S): application to substituent effects, gas phase acidities, and redox potentials. J Phys Chem A. 1999;103:1653–1661. doi:10.1021/jp984369a.
[58] Ji L, Faponle AS, Quesne MG, Sainna MA, Zhang J, Franke A, Kumar D, van Eldik R, Liu W, de Visser SP. Drug metabolism by cytochrome P450 enzymes: what distinguishes the pathways leading to substrate hydroxylation over desaturation? Chem Eur J. 2015;21:9083–9092. doi:10.1002/chem.201500329.
[59] St John PC, Guan Y, Kim Y, Kim S, Paton RS. Prediction of organic homolytic bond dissociation enthalpies at near chemical accuracy with sub-second computational cost. Nat Commun. 2020;11:2328. doi:10.1038/s41467-020-16201-z.
[60] Vessecchi R, Julião Zocolo G, Rubio Gouvea D, Hübner F, Cramer B, Rodrigues de Marchi MR, Humpf H-U, Lopes NP. Re-examination of the anion derivatives of isoflavones by radical fragmentation in negative

electrospray ionization tandem mass spectrometry: experimental and computational studies. Rapid Commun Mass Spectrom. 2011;25:2020–2026. doi:10.1002/rcm.5075.
[61] Meißner R, Feketeova L, Bayer A, Postler J, Limão-Vieira P, Denifl S. Positive and negative ions of the amino acid histidine formed in low-energy electron collisions. J Mass Spectrom. 2019;54:802–816. doi:10.1002/jms.4427.
[62] Lorenz Y, Gutiérrez A, Ferrer M, Engeser M. Bond dissociation energies of metallo-supramolecular building blocks: insight from fragmentation of selectively self-assembled heterometallic metallo-supramolecular aggregates. Inorg Chem. 2018;57:7346–7354. doi:10.1021/acs.inorgchem.8b00930.
[63] Ruttkies C, Schymanski EL, Wolf S, Hollender J, Neumann S. MetFrag relaunched: incorporating strategies beyond in silico fragmentation. J Cheminform. 2016;8:3. doi:10.1186/s13321-016-0115-9.
[64] Yu HS, He X, Li SL, Truhlar DG. MN15: a Kohn-Sham global-hybrid exchange-correlation density functional with broad accuracy for multi-reference and single-reference systems and noncovalent interactions. Chem Sci. 2016;7:5032–5051. doi:10.1039/C6SC00705H.
[65] Ditchfield R, Hehre WJ, Pople JA. Self-consistent molecular-orbital methods. IX. An extended Gaussian-type basis for molecular-orbital studies of organic molecules. J Chem Phys. 1971;54:724–728. doi:10.1063/1.1674902.
[66] Frisch MJ, Trucks GW, Schlegel HB, Scuseria GE, Robb MA, Cheeseman JR, et al. Gaussian 16, Revision B.01. Wallingford (CT): Gaussian, Inc.; 2016.
[67] Alayoubi A, Aqueel MS, Cruz CN, Ashraf M, Zidan AS. Application of *in vitro* lipolysis for the development of oral self-emulsified delivery system of nimodipine. Int J Pharm. 2018;553(1–2):441–453.
[68] Zhao Y, Zhai D, Chen X, Yu Q, He H, Sun Y, Gao Z, Wang L, Wang H, Han D, Ji H. Determination of nimodipine in human plasma by HPLC-ESI-MS and its application to a bioequivalence study. J Chromatogr Sci. 2010;48(2):81–85.
[69] Zhang X, Zhai S, Zhao R, Ouyang J, Li X, Baeyens WRG. Determination of cilnidipine, a new calcium antagonist, in human plasma using high-performance liquid chromatography with tandem mass spectrometric detection. Anal Chim Acta. 2007;600(1–2):142–146.
[70] Di Rago M, Saar E, Rodda LN, Turfus S, Kotsos A, Gerostamoulos D, Drummer OH. Fast targeted analysis of 132 acidic and neutral drugs and poisons in whole blood using LC-MS/MS. Forensic Sci Int. 2014;243:35–43.
[71] Pereira AS, Bicalho B, Ilha JO, De Nucci G. Analysis of dihydropyridine calcium channel blockers using negative ion photoionization mass spectrometry. J Chromatogr Sci. 2008;46(1):35–41.
[72] Fu C, Wu Q, Zhang Z, Xia Z, Liu Z, Lu H, Wang Y, Huang G. Development of a sensitive and rapid UHPLC-MS/MS method for simultaneous quantification of nine compounds in rat plasma and application in a comparative pharmacokinetic study after oral administration of Xuefu Zhuyu decoction and nimodipine. Biomed Chromatogr. 2020;34(9):e4872.
[73] Dvorácskó S, Körmöczi T, Sija É, Bende B, Weiczner R, Varga T, Ilisz I, Institóris L, Kereszty ÉM, Tömböly C, Berkecz R. Focusing on the 5F-MDMB-PICA, 4F-MDMB-BICA synthetic cannabinoids and their primary metabolites in analytical and pharmacological aspects. Toxicol Appl Pharmacol. 2023;470:116548.
[74] Vogeser M, Seger C. Pitfalls associated with the use of liquid chromatography-tandem mass spectrometry in the clinical laboratory. Clin Chem. 2010;56(8):1234–1244.
[75] Stokvis E, Rosing H, Beijnen JH. Stable isotopically labeled internal standards in quantitative bioanalysis using liquid chromatography/mass spectrometry: necessity or not? Rapid Commun Mass Spectrom. 2005;19(3):401–407. doi:10.1002/rcm.1790.
[76] Mindt S, Tokhi U, Hedtke M, Groß H, Hänggi D. Mass spectrometry-based method for quantification of nimodipine and glutamate in cerebrospinal fluid: pilot study with patients after aneurysmal subarachnoid haemorrhage. J Clin Pharm Ther. 2020;45:81–87.
[77] Nirogi RVS, Kandikere VN, Maurya S, Mudigonda K, Boosi R. Liquid chromatographic electrospray tandem mass spectrometric method for the quantification of nimodipine in human plasma. Die Pharmazie. 2006;61(10):828–834.
[78] Zhao T, Jiang W, Zhen X, Jin C, Zhang Y, Li H. QuEChERS-based approach to the extraction of five calcium channel blockers from plasma determined by UPLC-MS/MS. Molecules. 2023;28(2):671.
[79] Prajapat MD, Patel NJ, Bariya A, Patel SS, Butani SB. Formulation and evaluation of self-emulsifying drug delivery system for nimodipine, a BCS class II drug. J Drug Deliv Sci Technol. 2017;39:59–68.

[80] Zhang DM, He ZW, Liu XD, Li Y, Xie L, Wang GJ, Liu L. In vivo and *in vitro* studies on the effect of Huang-Lian-Jie-Du-Tang on nimodipine transport across rat blood-brain barrier. J Pharm Pharmacol. 2010;59(12):1733–1738.
[81] Wu C, Liao Q, Yao M, Xu X, Zhou Y, Hou X, Xie Z. Effect of natural borneol on the pharmacokinetics and distribution of nimodipine in mice. Eur J Drug Metab Pharmacokinet. 2014;39:17–24.
[82] Mohamed S, Riva R, Contin M. Simple and validated UHPLC-MS/MS analysis of nimodipine in plasma and cerebrospinal fluid of patients with subarachnoid haemorrhage. J Chromatogr B. 2016;1028:94–99.
[83] Riekes MK, Rauber GS, Kuminek G, Tagliari MP, Cardoso SG, Stulzer HK. Determination of nimodipine in the presence of its degradation products and overall kinetics through a stability-indicating LC method. J Chromatogr Sci. 2013;51(6):511–516.
[84] do Nascimento DF, de Moraes MO, Bezerra FAF, Pontes AV, Uchoa CRA, de Moraes RA, Osório Leite I, de Melo Santana GS, Macedo Santana AP, e Silva Leite ALA, Pedrazzoli Júnior J, de Moraes MEA. Determination of nimodipine in plasma by HPLC-MS/MS and pharmacokinetic application. Braz J Pharm Sci. 2010;46:665–677.
[85] Berkecz R, Tömösi F, Körmöczi T, Szegedi V, Horváth J, Janáky T. Comprehensive phospholipid and sphingomyelin profiling of different brain regions in mouse model of anxiety disorder using online two-dimensional (HILIC/RP)-LC/MS method. J Pharm Biomed Anal. 2018;149:308–317.
[86] Sheen J, Ho Y. A discharge adaptor interface for use in liquid chromatography/mass spectrometry. Rapid Commun Mass Spectrom. 2011;25(24):3675–3682.
[87] DrugBank. Toluene DrugBank [Internet]. [cited 2024 Feb 15]. Available from: https://hmdb.ca/metabolites/HMDB0029596
[88] HMDB. Ethyl acetate HMDB [Internet]. [cited 2024 Feb 15]. Available from: https://hmdb.ca/metabolites/HMDB0029596
[89] HMDB. Chloroform HMDB [Internet]. [cited 2024 Feb 15]. Available from: https://hmdb.ca/metabolites/HMDB0029596
[90] HMDB. Hexane HMDB [Internet]. [cited 2024 Feb 15]. Available from: https://hmdb.ca/metabolites/HMDB0029600
[91] Masumoto K, Takeyasu A, Oizumi K, Kobayashi T. Studies of novel 1,4-dihydropyridine Ca antagonist CS-905. I. Measurement of partition coefficient (logP) by high-performance liquid chromatography (HPLC). Yakugaku Zasshi. 1995;115(3):213–220.
[92] European Medicines Agency. ICH harmonised tripartite guideline: validation of analytical procedures: text and methodology Q2(R1) [Internet]. 2005 [cited 2024 Feb 14]. Available from: https://database.ich.org/sites/default/files/Q2%28R1%29%20Guideline.pdf
[93] Bruice PY, Bruice TC, Selander HG, Yagi H, Jerina DM. Comparative mechanisms of reaction of K-region and non-K-region arene oxides of phenanthrene. J Am Chem Soc. 1974;96:6814–6815. doi:10.1021/ja00828a073.
[94] Vessecchi R, Julião Zocolo G, Rubio Gouvea D, Hübner F, Cramer B, Rodrigues de Marchi MR, Humpf H-U, Lopes NP. Re-examination of the anion derivatives of isoflavones by radical fragmentation in negative electrospray ionization tandem mass spectrometry: experimental and computational studies. Rapid Commun Mass Spectrom. 2011;25:2020–2026. doi:10.1002/rcm.5075.
[95] Tchoumtchoua J, Njamen D, Mbanya JC, Skaltsounis A-L, Halabalaki M. Structure-oriented UHPLC-LTQ Orbitrap-based approach as a dereplication strategy for the identification of isoflavonoids from Amphimas pterocarpoides crude extract. J Mass Spectrom. 2013;48:561–575. doi:10.1002/jms.3167.
[96] Yu HS, He X, Li SL, Truhlar DG. MN15: a Kohn-Sham global-hybrid exchange-correlation density functional with broad accuracy for multi-reference and single-reference systems and noncovalent interactions. Chem Sci. 2016;7:5032–5051. doi:10.1039/C6SC00705H.
[97] Ditchfield R, Hehre WJ, Pople JA. Self-consistent molecular-orbital methods. IX. An extended Gaussian-type basis for molecular-orbital studies of organic molecules. J Chem Phys. 1971;54:724–728. doi:10.1063/1.1674902.
[98] Lech K, Fornal E. A mass spectrometry-based approach for characterization of red, blue, and purple natural dyes. Molecules. 2020;25:3223. doi:10.3390/molecules251432

Acknowledgment

I would like to express my sincere gratitude to my supervisor, **Dr. Róbert Berkecz**, for his continuous support, guidance, and encouragement throughout my PhD years. I am deeply grateful for his kindness, patience, and professional insight.

My sincere thanks also go to the head of the Institute of Pharmaceutical Analysis, Professor **Dr. István Ilisz**, for his kind support and valuable input. I would also like to thank **all former and present members of the Institute of Pharmaceutical Analysis** for being my second family in Hungary.

A special thanks goes to **Dr. Mihály Dernovics** for allowing me to be part of his remarkable work. My gratitude is also extended to **all co-authors involved in this work**.

On a personal level, I am deeply grateful to **all my friends in Hungary and Syria.**

My deepest gratitude goes to **my parents**, who have supported me since day one and blessed my journey with their prayers, love, and unwavering belief in me. I am profoundly grateful to my beloved sister, **Aliaa Ali**, for her art, her thoughts, and her constant encouragement. I am equally grateful to my brother, **Engineer Ali Ali**, who has supported me throughout my life, encouraged me to come to Hungary, and stood by me during the darkest days. My sincere thanks also go to my dear sisters-in-law, **Alaa and Maha Ismael**, for their support and kind hearts.

My special thanks go to the newest and cutest member of our family, my nephew **Aram**, who brought so much light and joy into our lives. I wish you a very happy and beautiful life, **Aram**.

I am also deeply thankful to my large family, including my grandmother, uncles, aunts, and cousins on both sides of the family, especially my lovely **Naya** and her brother.

Finally, I dedicate this work to the souls watching over us from the sky: to the memory of my grandfather, who passed away during my stay in Hungary; to the memory of my other beloved grandfather; and to the memory of my beloved grandmother, who passed away last year before she had the chance to congratulate me.

Project no. TKP2021-EGA-32 has been implemented with the support provided by the Ministry of Innovation and Technology of Hungary from the National Research, Development and Innovation Fund, financed under the TKP2021-EGA funding scheme. This work was supported by National Research, Development, and Innovation Office-NKFIH through projects: National Laboratory of Translational Neuroscience (NLTN) Neurodevelopmental disorders" "Adult nervous system disorders" (RRF-2.3.1-21-2022-00011).

Appendix

Fig. S1. CE optimization of **NMD** in positive ESI mode. The most abundant fragment ion is a quantifier ion (343 *m/z* with CE 11 V), and the second most intense fragment ion is a qualifier ion (301 *m/z* with CE 25 V), and additional fragmentations.

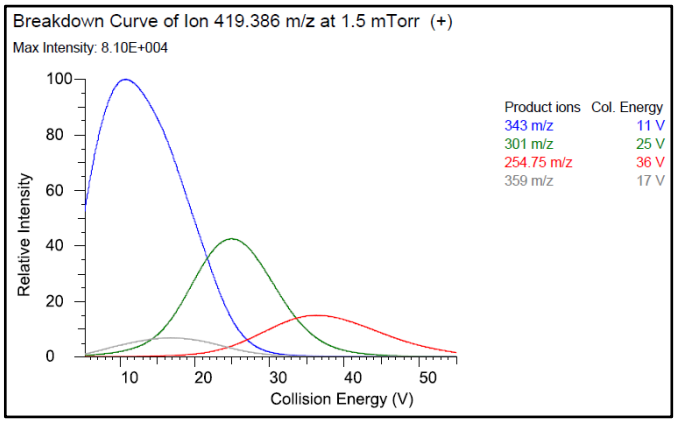

Fig S2. CE optimization of **NMD-D7** in positive ESI mode. The most abundant fragment ion is a quantifier ion (350 *m/z* with collision energy 13 V), and the second most intense fragment ion is a qualifier ion (302 *m/z* with collision energy 26 V), and additional fragmentations.

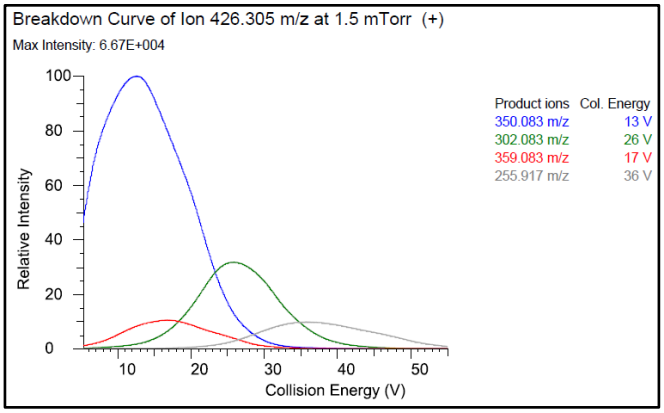

Fig. S3. CE optimization of **NMD** in negative ESI mode. The most abundant fragment ion is a quantifier ion (122 *m/z* with collision energy 20 V), and the second most intense fragment ion is a qualifier ion (294 *m/z* with collision energy 18 V), and additional fragmentations.

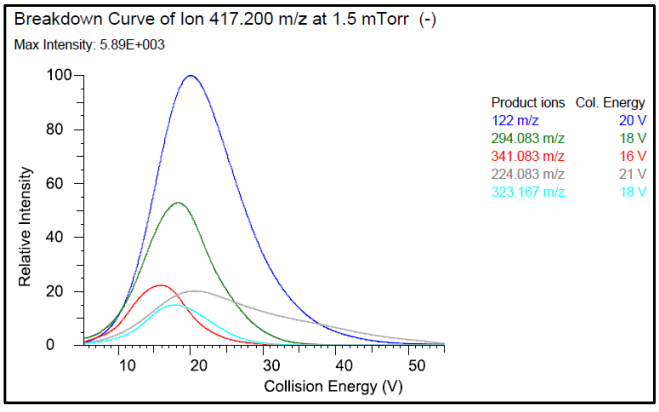

Table S1. Main validation parameters of the UHPLC-MS/MS method for quantitation of **NMD** in the rat brain.

Validation parameters	Criteria range [45]	Brain
R^2	> 0.99	0.9927
Limit of linearity (µg/g brain)	0.023-229.241	0.023-229.24
LOD (µg/g)	n.d.	0.015
Bias "LOW" (Δ%)	≤ 20	19.7
Bias MID (Δ%)	≤ 15	8.2
Bias HIGH (Δ%)	≤ 15	11.6
Within-run precision LOW (%CV)	≤ 15	2.8, 4.6, 1.2
Within-run precision MID (%CV)	≤ 15	3.0, 1.4, 4.2
Within-run precision HIGH (%CV)	≤ 15	1.9, 0.7, 0.7
Between-run precision LOW (%CV)	≤ 15	7.9
Between-run precision MID (%CV)	≤ 15	10.4
Between-run precision HIGH (%CV)	≤ 15	5.6
3 day stability LOW (Δ%)	≤ 15	1.9
3 day stability MID (Δ%)	≤ 15	2.2
3 day stability HIGH (Δ%)	≤ 15	-0.9
Autosampler stability at 4 °C LOW (Δ%)	≤ 15	-1.2
Autosampler stability at 4 °C MID (Δ%)	≤ 15	6.8
Autosampler stability at 4 °C HIGH (Δ%)	≤ 15	-0.9
1 year stability at -80 °C '20 min' at 7.38 pH (Δ%)	≤ 15	-10.0
1 year stability at -80 °C '20 min' at 6.50 pH (Δ%)	≤ 15	-5.2
1 year stability at -80 °C '20 min' at 7.57 pH (Δ%)	≤ 15	-11.5
3 cycle freeze-thaw LOW	≤ 15	-10.6
3 cycle freeze-thaw MID	≤ 15	1.7

3 cycle freeze-thaw HIGH	≤ 15	-1.2
Recovery LOW (%)	n.d.	96.9
Recovery MID (%)	n.d.	110.6
Recovery HIGH (%)	n.d.	98.7
Matrix effect LOW (Δ%)	±15	12.9
Matrix effect MID (Δ%)	±15	-9.0
Matrix effect HIGH (Δ%)	±15	3.3
Process efficiency LOW (%)	n.d.	109.4
Process efficiency MID (%)	n.d.	100.6
Process efficiency HIGH (%)	n.d.	102.0
Selectivity (analyte interference)	≤ 10%	< 10%
Carry-over (%)	≤ 0.5	< 0.1%
Retention stability (min)	2.30 - 2.40	2.35 ± 0.01

Table S2. Mean comparisons test results (ANOVA with Bonferroni correction for multiple comparisons) of obtained **NMD** concentration values at three pH. (* $p < 0.05$, ** $p < 0.01$, *** $p < 0.001$)

Bonferroni's Multiple Comparison Test	Mean Diff.	t	Significant? P < 0.05?	Summary	95% CI of diff
0.5 min					
7.38 vs 6.50	1.952	2.309	No	ns	-0.2170 to 4.121
7.38 vs 7.57	4.084	4.555	Yes	***	1.783 to 6.384
6.50 vs 7.57	2.132	2.378	No	ns	-0.1686 to 4.432
10 min					
7.38 vs 6.50	-0.3525	0.1110	No	ns	-8.420 to 7.715
7.38 vs 7.57	5.644	1.590	No	ns	-3.376 to 14.66
6.50 vs 7.57	5.997	1.689	No	ns	-3.023 to 15.02
20 min					
7.38 vs 6.50	-0.3994	0.1436	No	ns	-7.416 to 6.617
7.38 vs 7.57	0.7366	0.2648	No	ns	-6.280 to 7.753
6.50 vs 7.57	1.136	0.4083	No	ns	-5.881 to 8.153

30 min					
7.38 vs 6.50	-8.121	2.067	No	ns	-18.15 to 1.906
7.38 vs 7.57	4.408	0.9162	No	ns	-7.872 to 16.69
6.50 vs 7.57	12.53	2.604	Yes	*	0.2487 to 24.81
40 min					
7.38 vs 6.50	-10.93	3.371	Yes	**	-19.21 to -2.655
7.38 vs 7.57	-2.728	0.7890	No	ns	-11.55 to 6.097
6.50 vs 7.57	8.205	2.284	No	ns	-0.9659 to 17.38
50 min					
7.38 vs 6.50	-7.607	1.267	No	ns	-22.87 to 7.654
7.38 vs 7.57	1.449	0.2158	No	ns	-15.61 to 18.51
6.50 vs 7.57	9.056	1.349	No	ns	-8.006 to 26.12
60 min					
7.38 vs 6.50	-9.731	2.343	No	ns	-20.28 to 0.8223
7.38 vs 7.57	0.1626	0.03502	No	ns	-11.64 to 11.96
6.50 vs 7.57	9.894	2.131	No	ns	-1.905 to 21.69

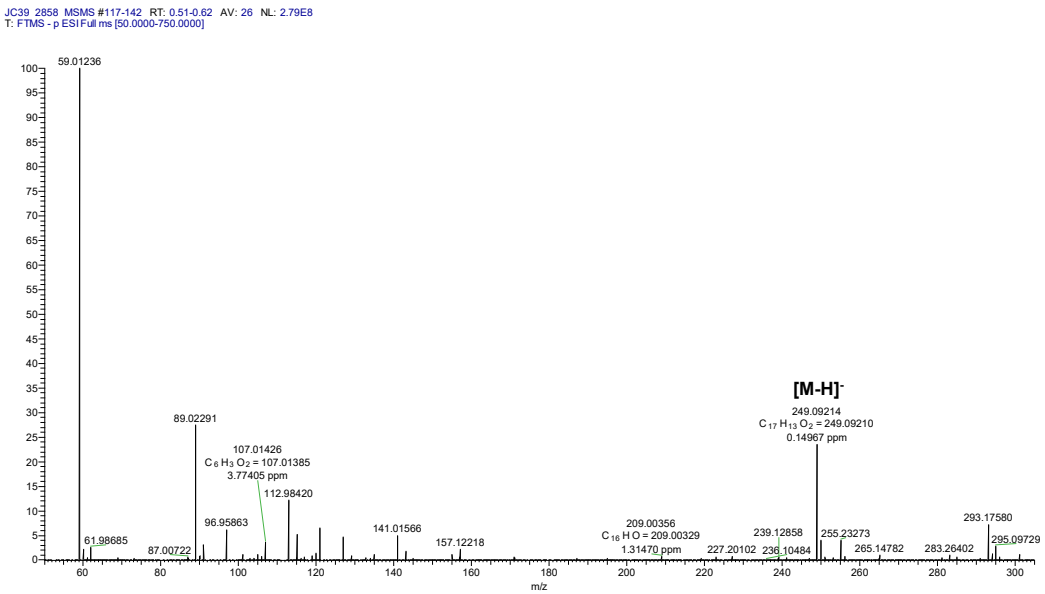

Fig. S4. HRMS spectrum of **Compound 3** obtained by direct infusion HRMS-HRMS measurement in negative mode.

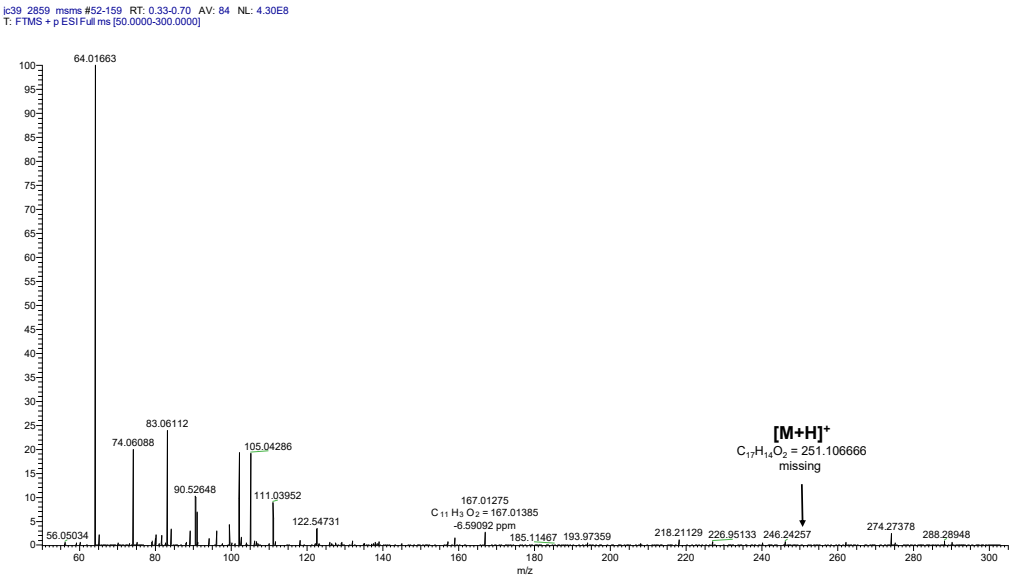

Fig. S5. HRMS spectrum of **Compound 3** obtained by direct infusion HESI-HRMS measurement in positive mode

Table S3. Maximum mass difference obtained for precursor ions via H radical loss

Compound	**Difference / Da**
1	1
2	6
3	4
4	9
5	2
6	5
7	1

Table S4. The calculated bond dissociation energies (BDE) of the homolytic cleavage of X— H bonds (X=C,O) of **Compound 2** after the deprotonation of O(15) using the MN15 density functional and the MN15/6-31G+(d,p) basis set. The 'BDE Step 1-4' columns show the BDE values used to identify the first four steps of the most likely fragmentation pathway. The BDE of the most likely cleavage is shown in bold at each step. The numbering of atoms of **Compound 2** is shown in **Fig. 33** BDE values are presented in kJ/mol.

	BDE Step 1	BDE Step 2	BDE Step 3	BDE Step 4
C(1)—H	459.8	504.8	471.3	456.7
C(6)—H	461.8	474.2	446.1	439.4
C(7)—H	354.1	369.4	**291.1**	453.6
C(8)—H	369.1	362.7	359.1	**185.9**
C(11)—H	469.9	505.8	471.1	500.4
C(13)—H	469.2	502,1	469.1	494.0
O(17)—H	419.5	415.4	414.7	411.0
O(16)—H	**266.5**	-	-	-
C(18)—H	463.8	543.7	464.6	523.2
C(19)—H	371.0	**362.6**	462.9	482.1

Table S5. The calculated bond dissociation energies (BDE) of the homolytic cleavage of X— H bonds (X=C,O) of Compound 1 and Compound 6 after the deprotonation of O(15) using the MN15 density functional and the MN15/6-31G+(d,p) basis set. The standard reaction enthalpies of two other fragmentations are also listed in the last two lines. These are the homolytic cleavage of O(16)—CH_3 bond in Compound 6 and the fragmentation [Compound 1]→[Compound 1-CH_3OH] + CH_3OH. The values presented here were used to identify the first step of the most likely fragmentation pathway. The BDE of the most likely cleavage is shown in bold. The numbering of atoms of Compound 6 and Compound 1 is shown in Fig. 4. BDE values are presented in kJ/mol.

	Compound 6	Compound 1
C(1)—H	461.5	464.9
C(6)—H	460.9	463.2
C(7)—H	356.7	356.7
C(8)—H	369.1	370.5
C(11)—H	470.0	469.5
C(13)—H	469.2	461.4
O(16)—H	-	272.8

O(17)—H	419.7	379.2
C(18)—H	463.8	421.2
C(19)—H	369.9	370.5
O(16)—CH_3	**178.6**	-
[Compound 1]→[Compound 1-CH_3OH]+ CH_3OH	-	**68.6**

Table S6. Main validation parameters of UHPLC-MS/HRMS method.

	Compounds						
	Comp. 1	**Comp. 2**	**Comp. 3**	**Comp. 4**	**Comp. 5**	**Comp. 6**	**Comp. 7**
Linearity range (nM)	10-5000	25-5000	10-5000	25-5000	25-5000	10-5000	25-5000
Regression model	linear	linear	linear	linear	quadratic	linear	linear
Transformation	no	no	no	no	no	no	no
Weight	1/x	1/x	1/x	1/x	equal	1/x	1/x
Forced through origin	yes	yes	yes	yes	yes	yes	yes
R^2	0.995	0.996	0.993	0.990	0.997	0.993	0.994
LOD (nM)	4.65	13.47	7.78	16.03	15.39	7.72	10.12
LLOQ (nM)	10.00	25.00	10.00	25.00	25.00	10.00	25.00
Carry-over (%)	< 0.001	< 0.001	< 0.001	< 0.001	< 0.001	< 0.001	< 0.001
Inter-day stability LLOQ	-2.2	-5.7	4.8	-19.5	2.6	-9.7	-5.3
Inter-day stability „Low”	-6.2	-1.9	-1.2	-18.5	-6.7	12.6	-6.4
Inter-day stability „Mid” (%)	3.5	-13.8	4.8	-1.5	3.1	-10.5	-4.9
Inter-day stability „High”	-10.1	-3.4	0.2	3.9	5.3	0.3	-1.8
Accuracy LLOQ (%)	100.4	80.9	83.2	72.1	89.0	81.8	81.8
Accuracy „Low” (%)	105.3	90.2	111.8	72.2	105.5	97.3	91.1
Accuracy „Mid” (%)	96.7	92.5	103.4	95.5	125.3	95.7	85.7
Accuracy „High” (%)	98.3	96.7	105.4	96.6	97.3	105.8	105.7
Precision LLOQ (%CV)	14.0	11.7	11.1	15.2	8.3	3.6	15.0
Precision „Low” (%CV)	14.0	9.0	9.4	14.5	4.3	3.3	4.8
Precision „Mid” (%CV)	9.6	7.9	9.9	1.9	1.4	9.0	6.6
Precision „High” (%CV)	5.8	2.7	7.6	8.7	4.2	8.9	8.3
Retention stability (min)	2.14 ± 0.02	2.42 ± 0.02	2.45 ± 0.01	2.63 ± 0.02	3.39 ± 0.01	3.53 ± 0.01	3.75 ±

Com=Compound

Table S7 Results of matrix effect (%).

mg/mL	concentration level	extraction	Compound 1	Compound 2	Compound 3	Compound 4	Compound 5	Compound 6	Compound 7
0.001	LLOQ	MeOH	97.8	98.3	89.7	93.5	86.0	99.0	98.5
	LOW		103.7	84.7	98.3	81.6	83.8	88.8	91.9
	MID		127.0	119.6	132.4	121.2	125.3	115.0	120.0
	HIGH		110.3	82.2	93.5	87.8	94.6	77.7	79.6
	LLOQ	CH_2Cl_2	102.3	103.5	113.1	102.9	92.7	98.3	99.2
	LOW		92.1	90.9	102.1	77.3	83.1	80.8	82.6
	MID		131.2	136.8	139.1	120.6	127.5	123.4	130.5
	HIGH		95.1	92.8	95.7	82.1	93.0	81.9	84.3
0.01	LLOQ	MeOH	93.0	90.2	88.6	81.5	86.4	79.5	82.1
	LOW		105.9	95.4	98.3	86.3	86.5	84.4	87.4
	MID		146.3	153.4	146.0	134.3	154.5	146.5	151.0
	HIGH		104.3	87.3	91.8	74.3	98.0	74.7	76.4
	LLOQ	CH_2Cl_2	103.9	104.3	106.8	85.5	105.5	88.0	92.4
	LOW		98.3	102.1	111.2	87.0	103.0	85.0	93.0
	MID		128.8	122.2	122.5	114.8	121.8	123.7	123.9
	HIGH		99.4	94.3	103.2	87.9	101.4	87.0	86.8
0.1	LLOQ	MeOH	103.8	112.5	125.3	108.9	107.9	101.9	106.5
	LOW		97.7	117.2	118.3	99.3	97.7	98.8	103.4
	MID		100.6	106.2	106.6	96.1	98.1	103.2	103.8
	HIGH		97.6	96.8	94.9	93.1	96.3	97.0	100.7
	LLOQ	CH_2Cl_2	83.7	123.6	56.3	88.5	91.0	92.1	85.9
	LOW		87.0	132.0	121.8	75.8	84.9	83.8	82.6
	MID		122.2	115.7	121.6	111.0	99.8	145.1	143.9
	HIGH		74.1	84.0	69.7	70.6	76.1	82.2	82.2

Figure S6 . UHPLC-MS/HRMS chromatograms of phenanthrenes using ACQUITY UPLC HSS C18 SB (100 x 2.1 mm, 1.8 µm) column.

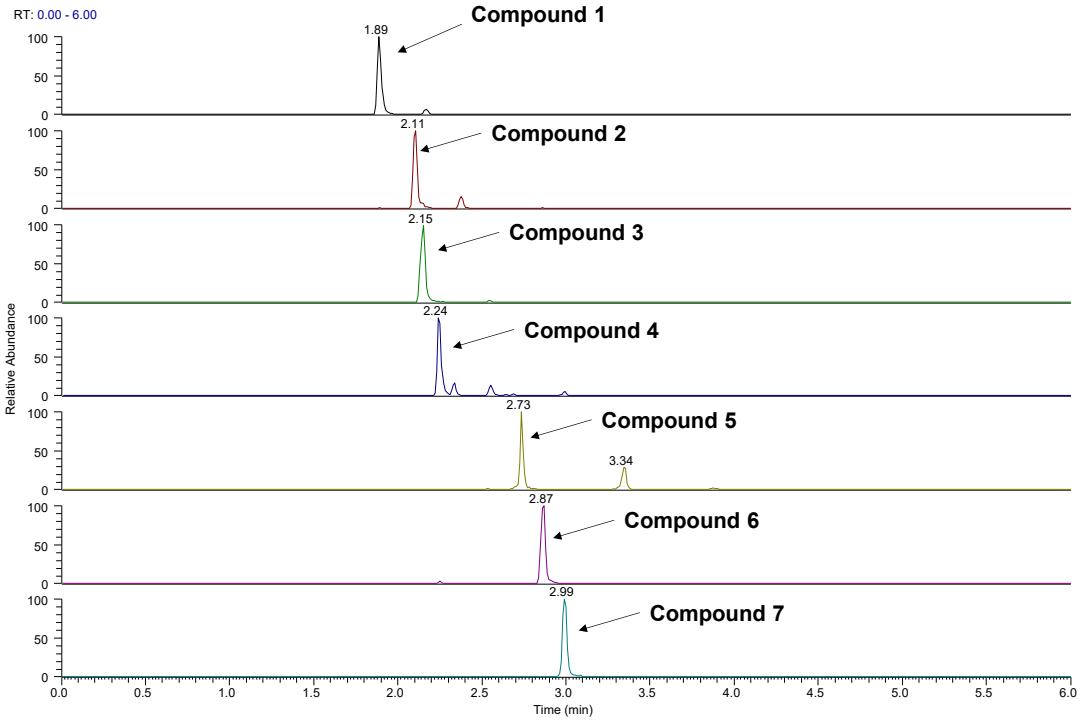

Figure S7. UHPLC-MS/HRMS chromatograms of phenanthrenes on an ACQUITY UPLC BEH C18 (100 x 2.1 mm, 1.7 µm) column.

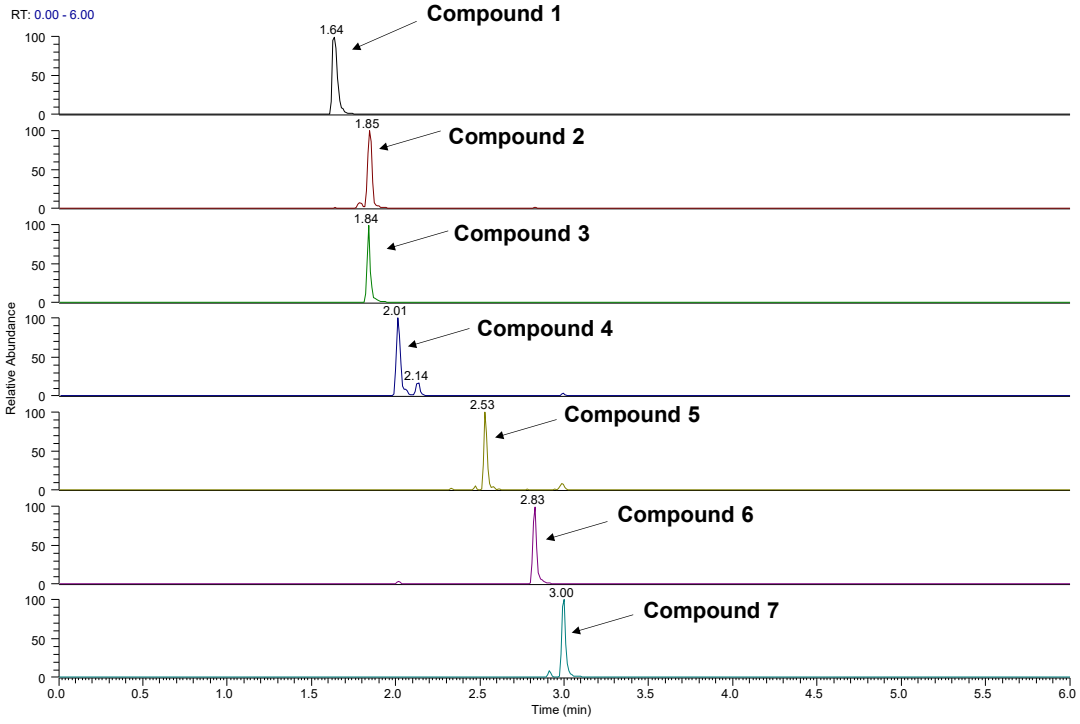

Figure S8. UHPLC-MS/HRMS chromatograms of phenanthrenes using ACQUITY UPLC HSS T3 (100 x 2.1 mm, 1.8 µm) column.

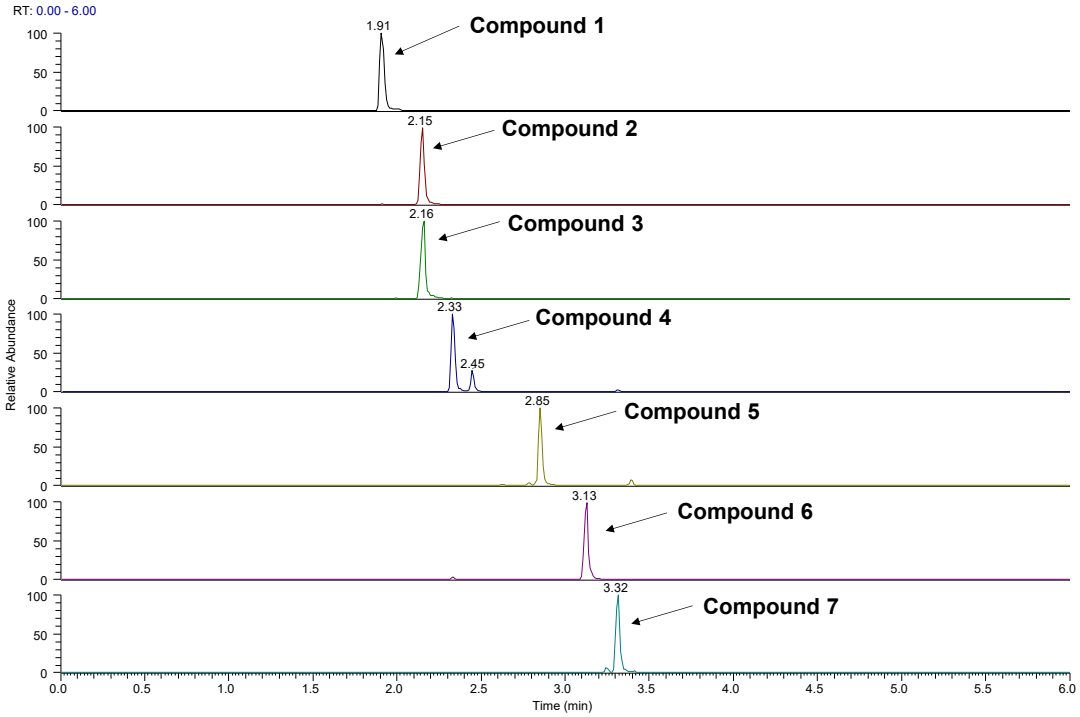

Figure S9. UHPLC-MS/HRMS chromatograms of phenanthrenes using Kinetex C18 (100 x 2.1 mm, 2.6 µm) column.

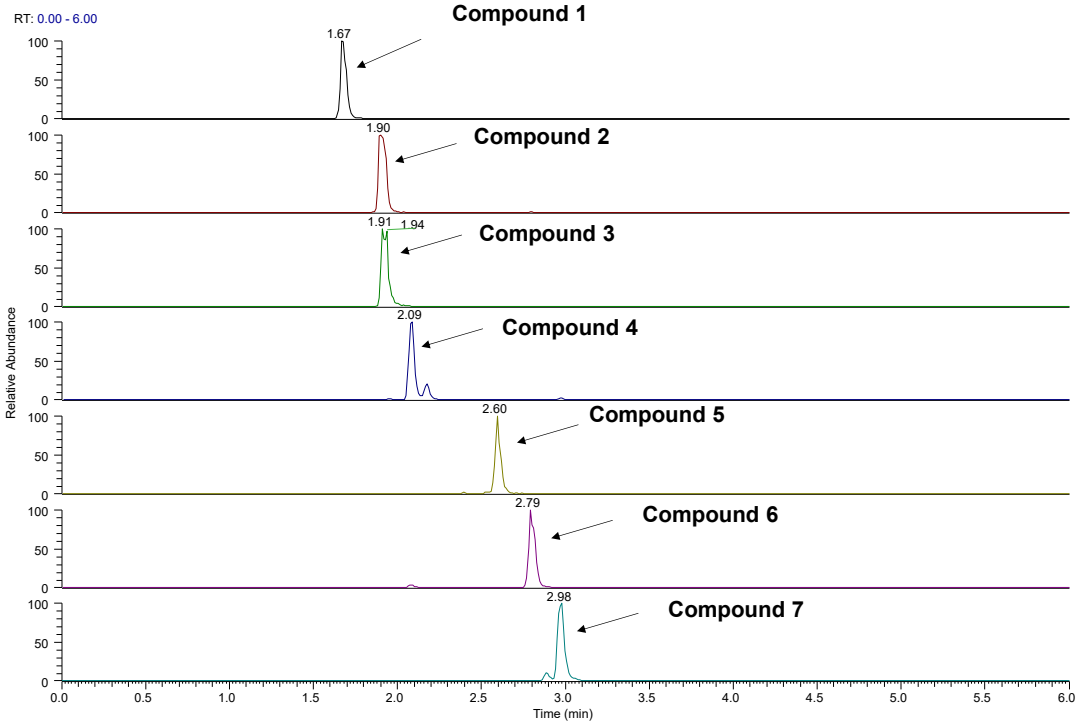

Figure S10. UHPLC-MS/HRMS chromatograms of phenanthrenes using Kinetex Biphenyl (100 x 2.1 mm, 2.6 µm) column.

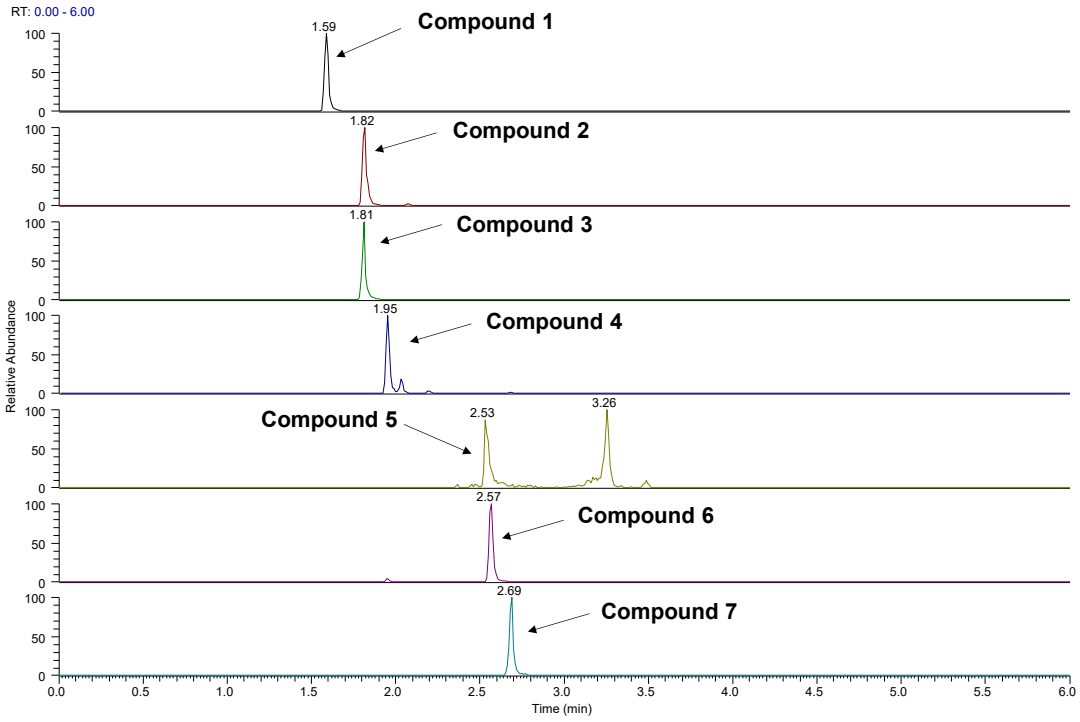

Figure S11. UHPLC-MS/HRMS chromatograms of phenanthrenes using Accucore C30 (150 x 2.1 mm, 2.6 µm) column.

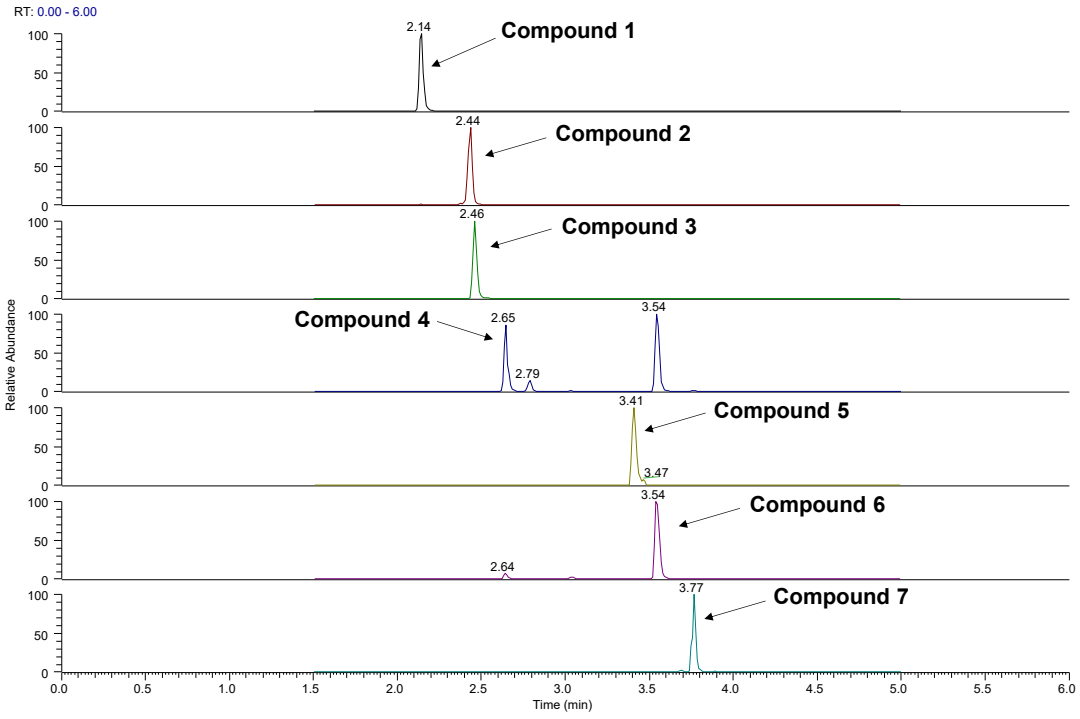

Figure S12. UHPLC-MS/HRMS chromatograms of phenanthrenes using Kinetex PFP (50 x 2.1 mm, 1.7 µm) column.

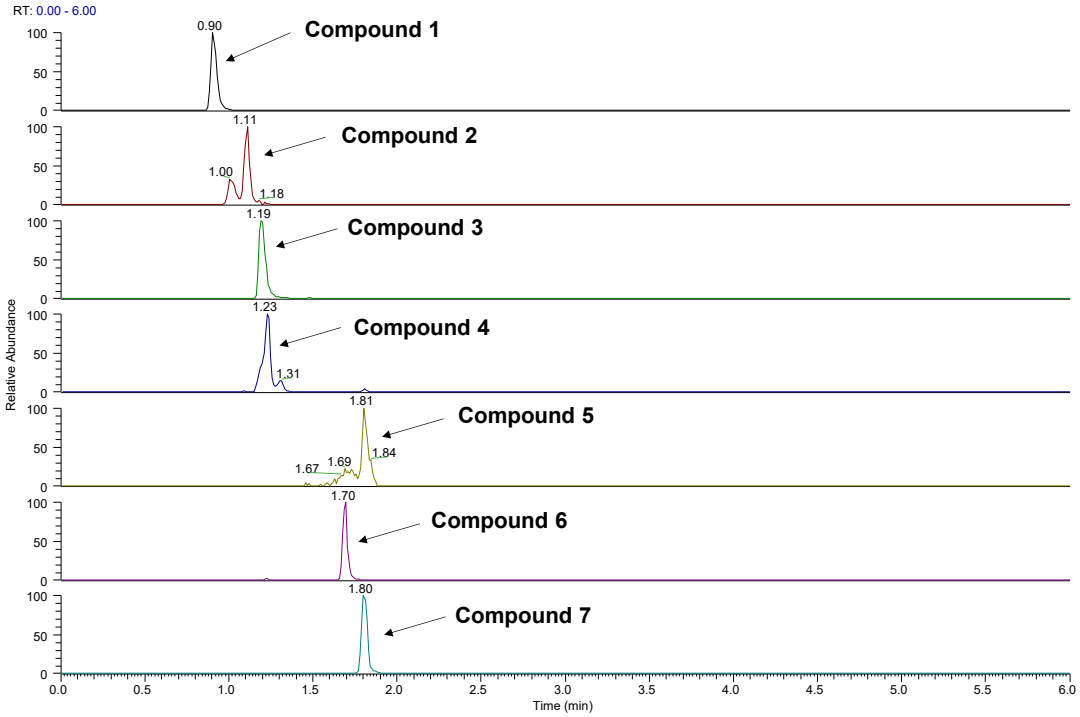

Figure S13. MS/HRMS spectra obtained for newly identified isomers (A: **I-1**, RT: 1.89 min; B: **I-2**, RT: 2.28 min) in the CH_2Cl_2 fraction of **Plant 3** compared to **Compound 3** (C, RT: 2.45 min) at 53 collision energy.

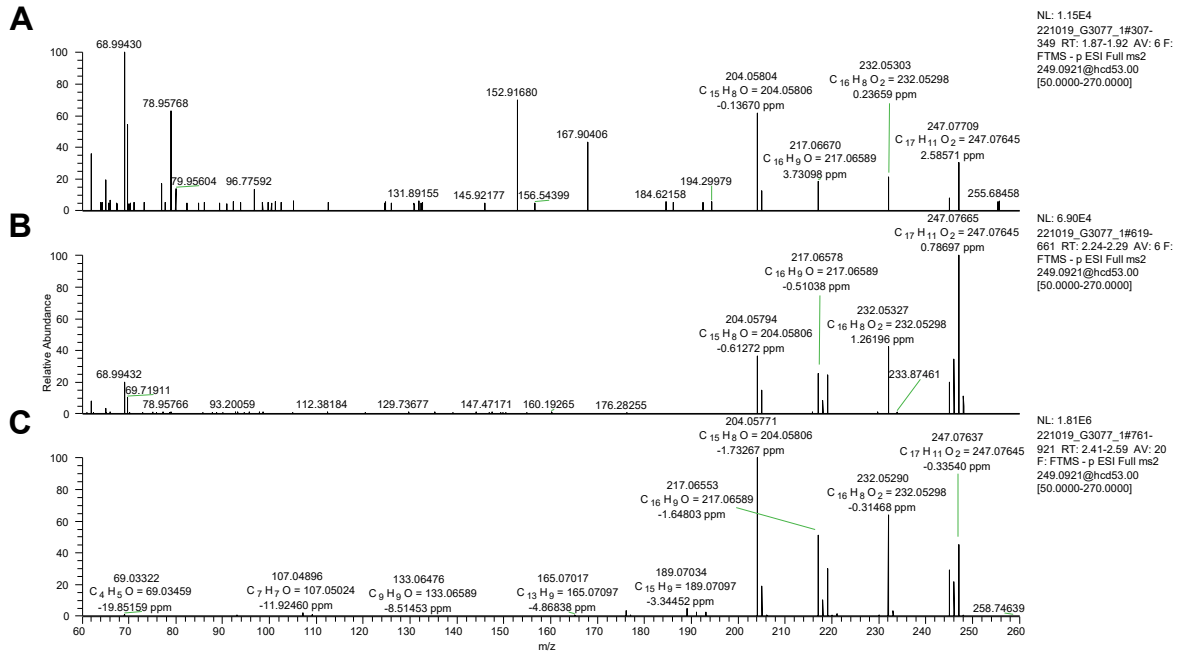

Figure S14. MS/HRMS spectrum obtained for newly identified isomer (A: **I-2**, RT: 2.28 min) in the CH_2Cl_2 fraction of **Plant 1** compared to **Compound 3** (B, RT: 2.45 min) at 53 collision energy.

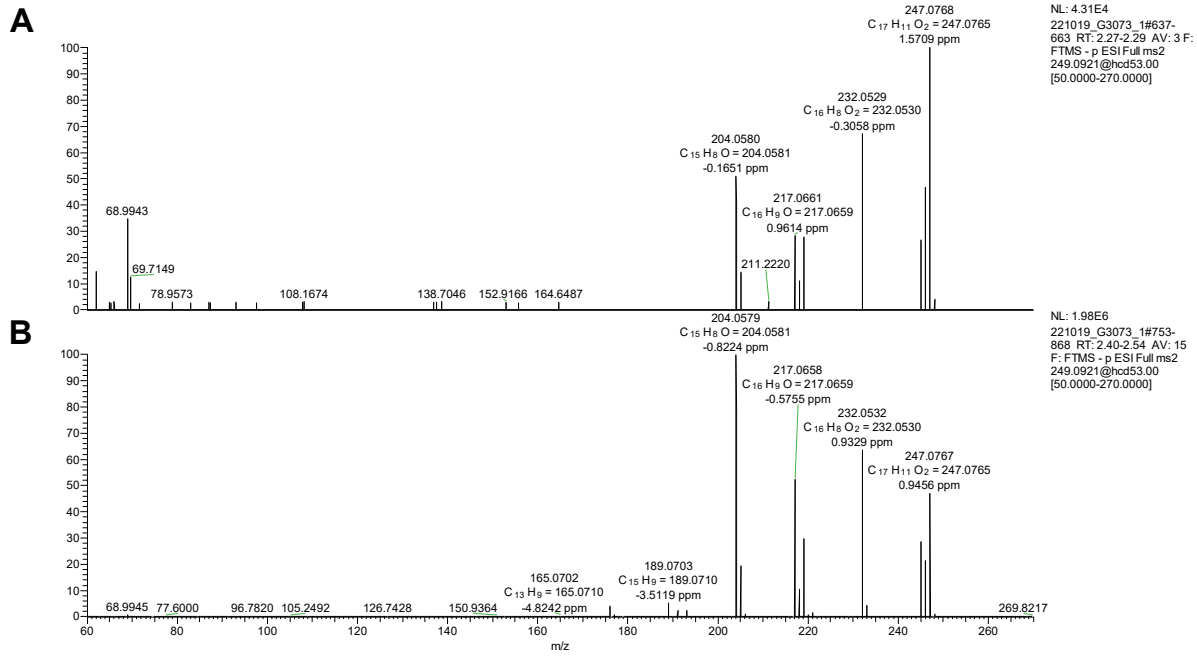

Figure S15. MS/HRMS spectra of newly identified isomers (A: **I-1**, RT: 1.89 min; B: **I-2**, RT: 2.28 min) in the CH_2Cl_2 fraction of **Plant 5** compared to **Compound 3** (C, RT: 2.45 min) at 53 collision energy.

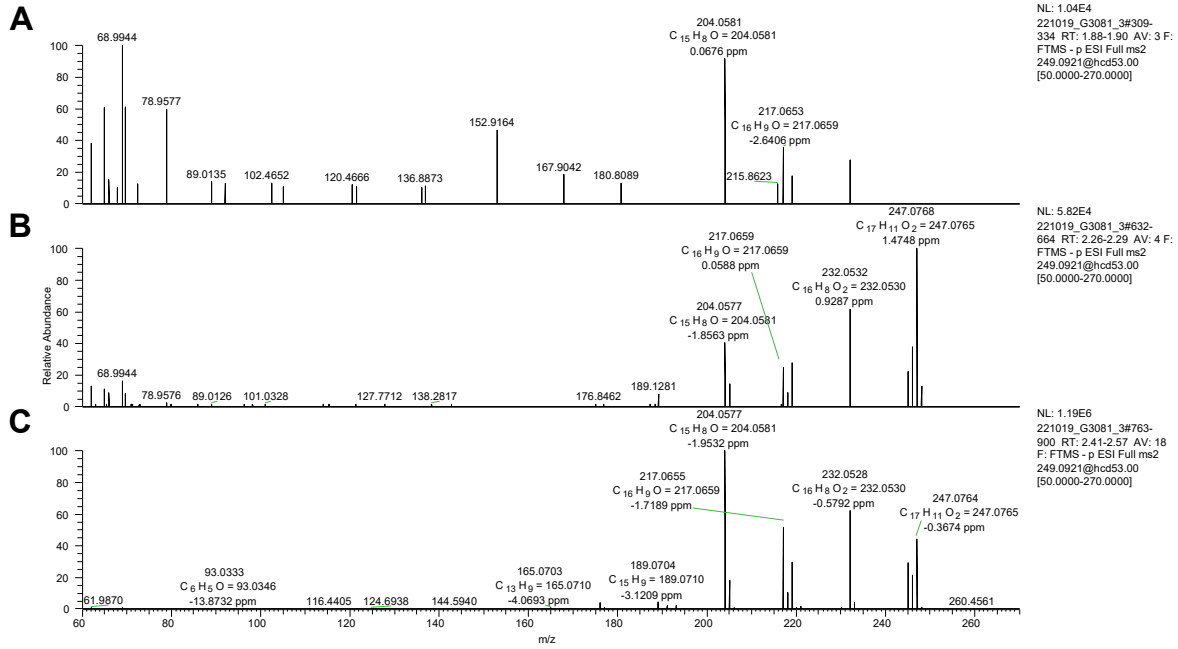

Figure S16. MS/HRMS spectrum of newly identified isomer (A: **I-3**, RT: 2.78 min) in the MeOH fraction of **Plant 1** compared to **Compound 4** (B, RT: 2.63 min) and **Compound 6** (C, RT: 3.53 min) at 44 collision energy.

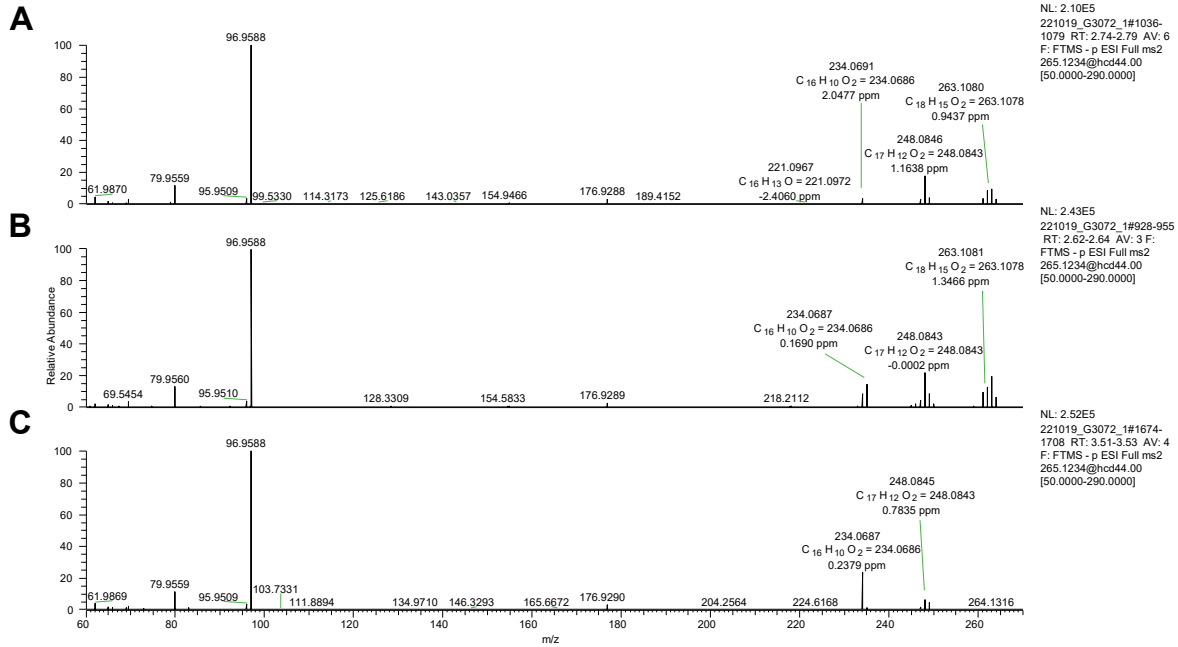

Figure S17. MS/HRMS spectrum of newly identified isomer (A: **I-3**, RT: 2.78 min) in the CH_2Cl_2 fraction of **Plant 1** compared to **Compound 4** (B, RT: 2.63 mint) at 44 collision energy.

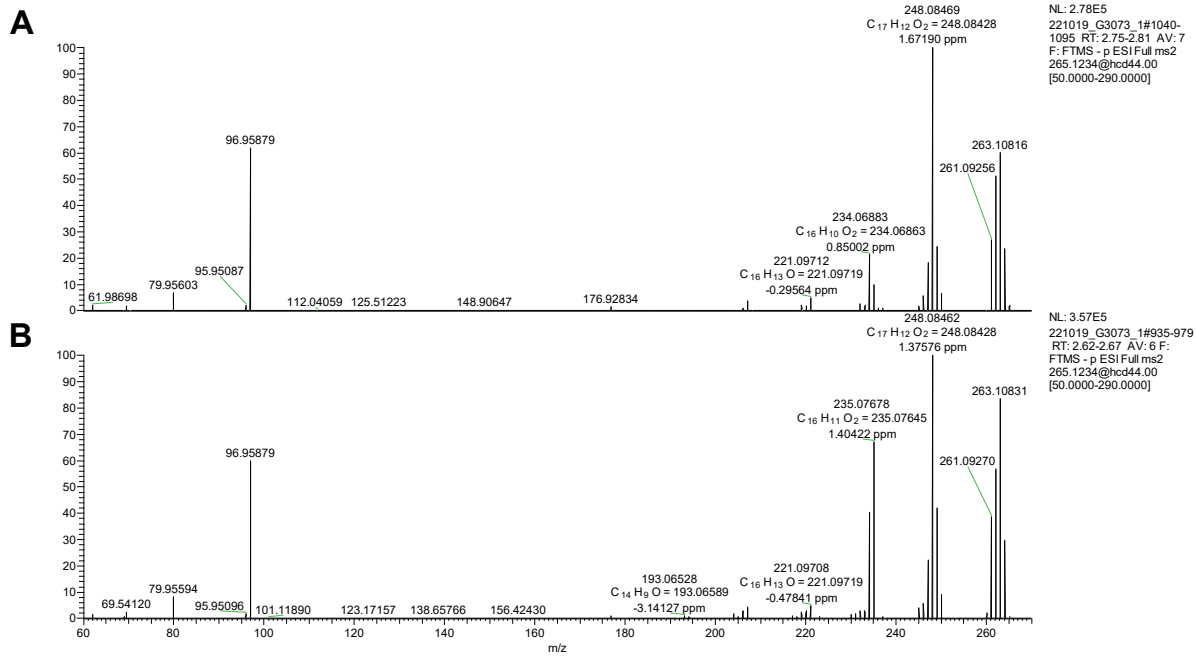

Figure S18. MS/HRMS spectrum of newly identified isomer (A: **I-3**, RT: 2.78 min) in the CH_2Cl_2 fraction of **Plant 2** compared to **Compound 4** (B, RT: 2.63 min) at 44 collision energy.

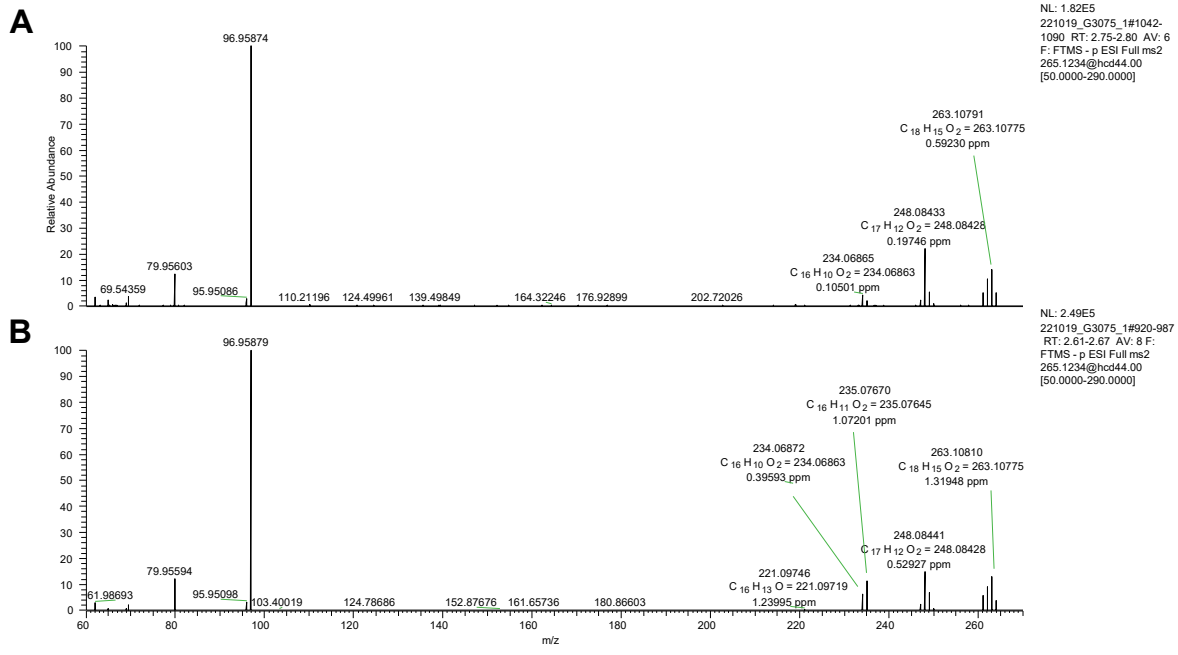

Figure S19. MS/HRMS spectrum of newly identified isomer (A: **I-3**, RT: 2.78 min) in the MeOH fraction of **Plant 3** compared to **Compound 4** (B, RT: 2.63 min) and **Compound 6** (C, RT: 3.53 min) at 44 collision energy.

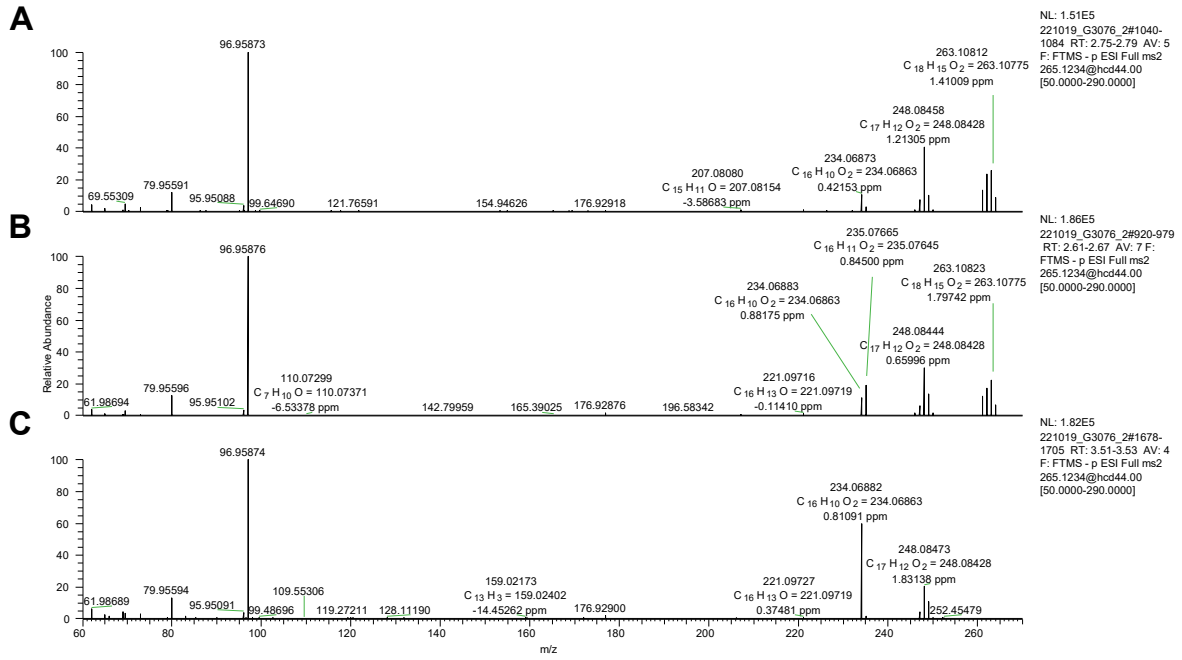

Figure S20. MS/HRMS spectrum of newly identified isomer (A: **I-3**, RT: 2.78 min) in the CH_2Cl_2 fraction of **Plant 3** compared to **Compound 4** (B, RT: 2.63 min) at 44 collision energy.

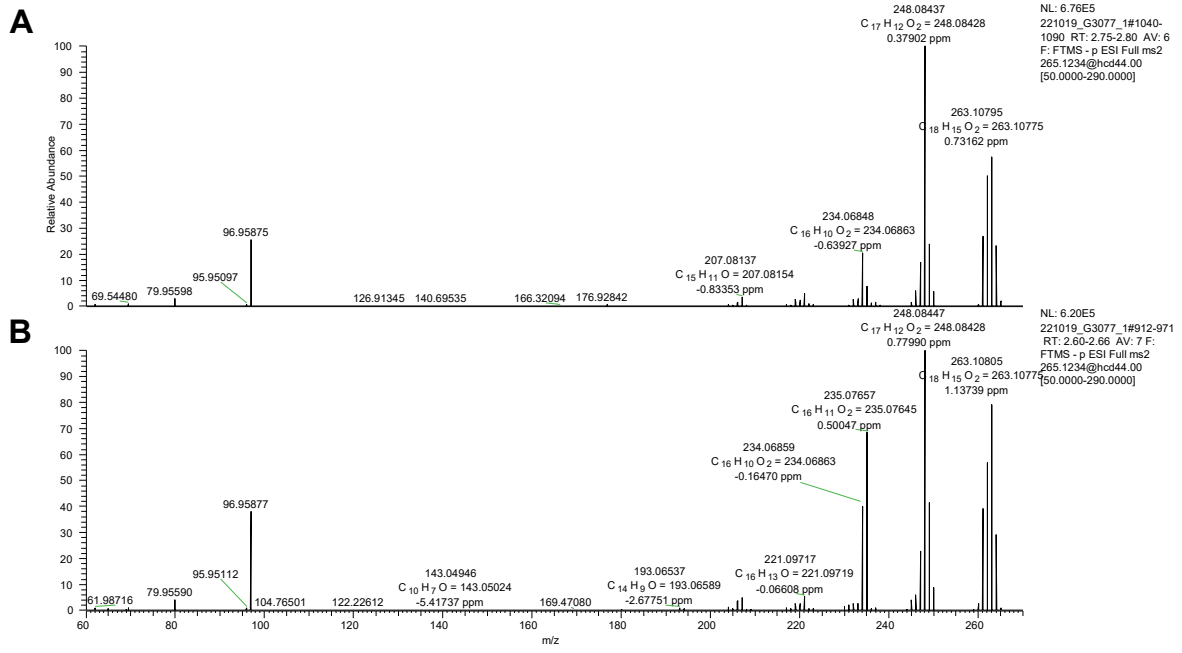

Figure S21. MS/HRMS spectrum of newly identified isomer (A: **I-3**, RT: 2.78 min) in the MeOH fraction of **Plant 4** compared to **Compound 4** (B, RT: 2.63 min) and **Compound 6** (C, RT: 3.53 min) at 44 collision energy.

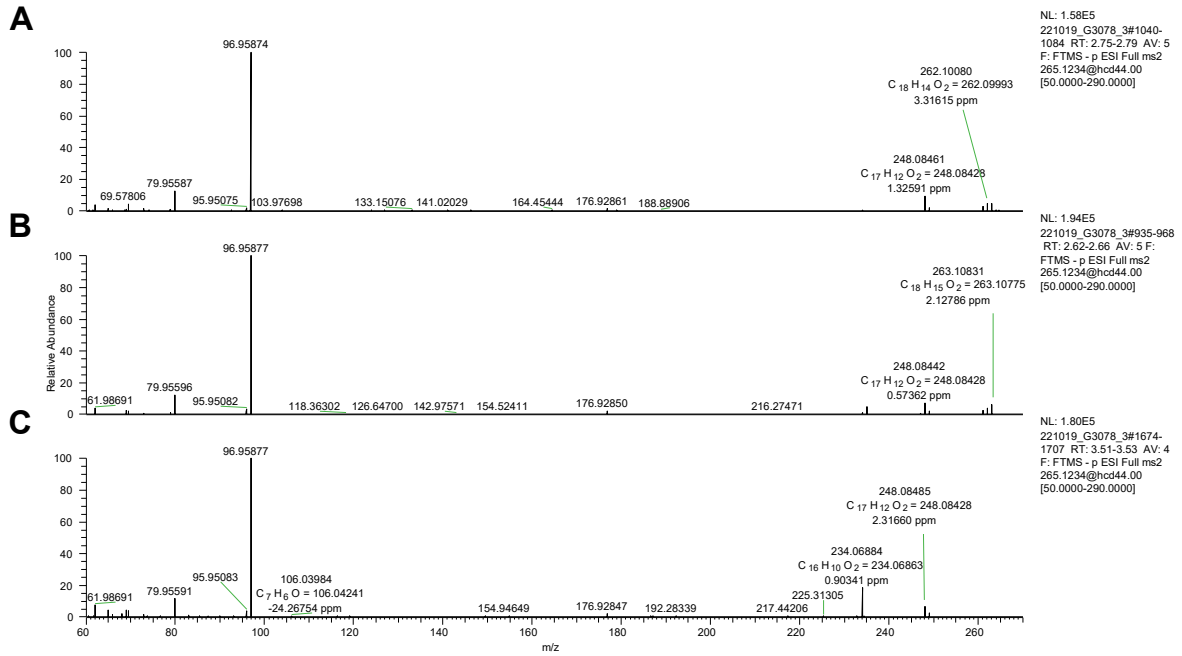

Figure S22. MS/HRMS spectrum of newly identified isomer (A: **I-3**, RT: 2.78 min) in the CH_2Cl_2 fraction of **Plant 4** compared to **Compound 4** (B, RT: 2.63 min) at 44 collision energy.

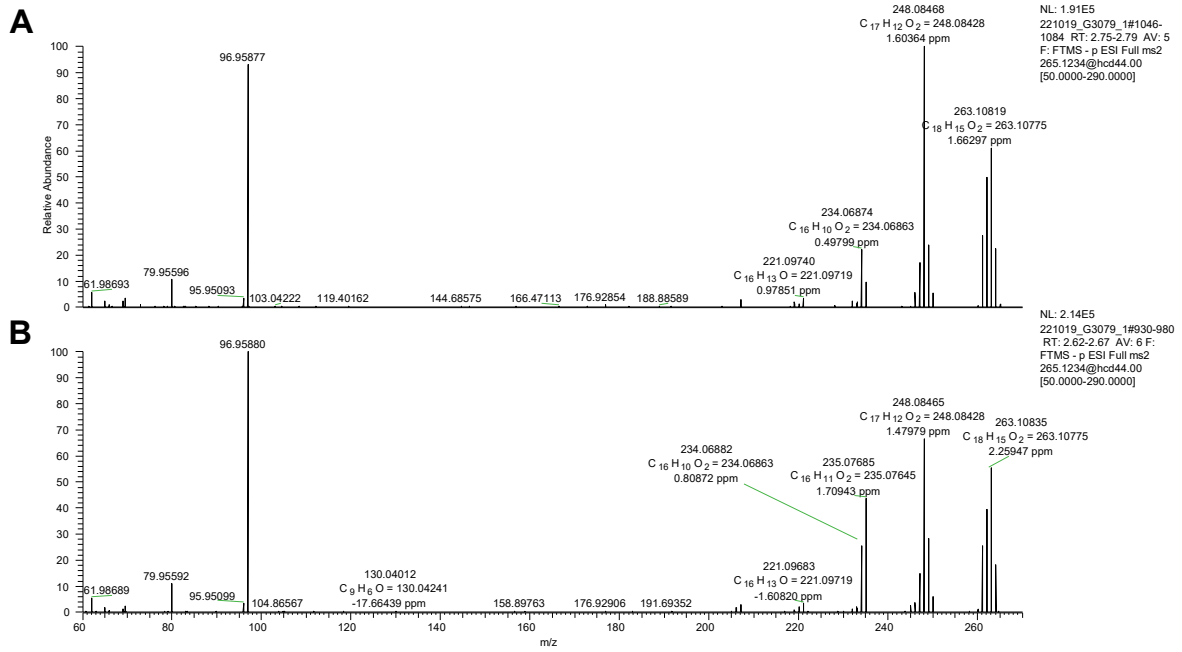

Figure S23. MS/HRMS spectrum of newly identified isomer (A: **I-3**, RT: 2.78 min) in the MeOH fraction of **Plant 5** compared to **Compound 4** (B, RT: 2.63 min) and **Compound 6** (C, RT: 3.53 min) at 44 collision energy.

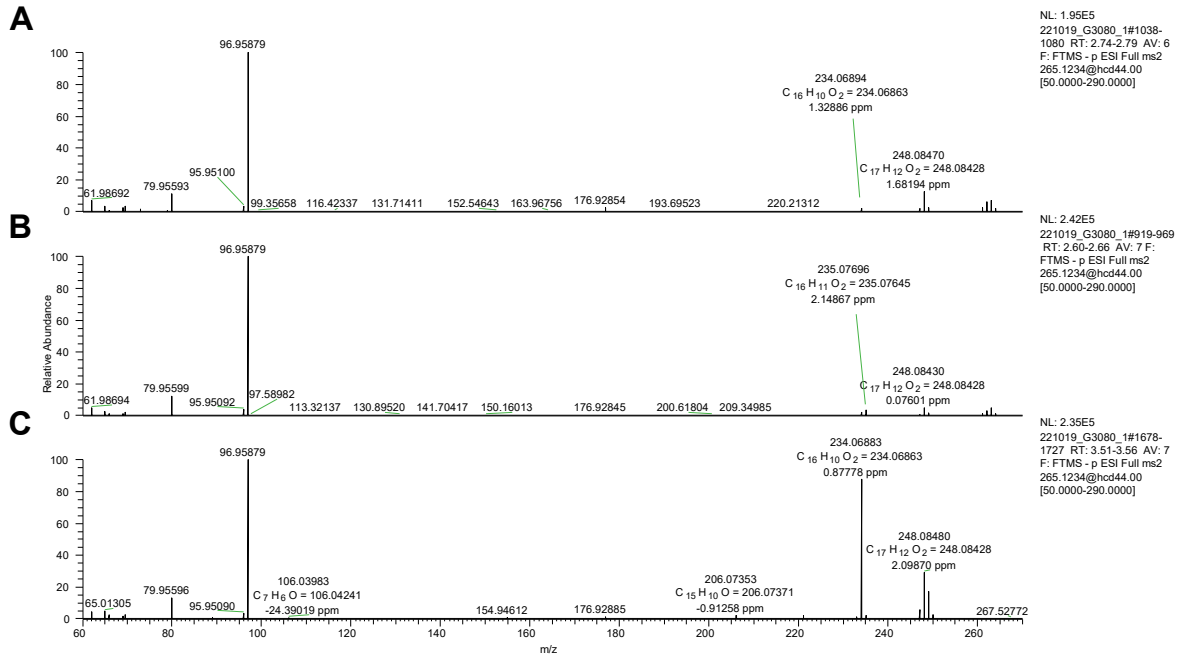

Figure S24. MS/HRMS spectrum of newly identified isomer (A: **I-3**, RT: 2.78 min) in the CH_2Cl_2 fraction of **Plant 5** compared to **Compound 4** (B, RT: 2.63 min) and **Compound 6** (C, RT: 3.53 min) at 44 collision energy.

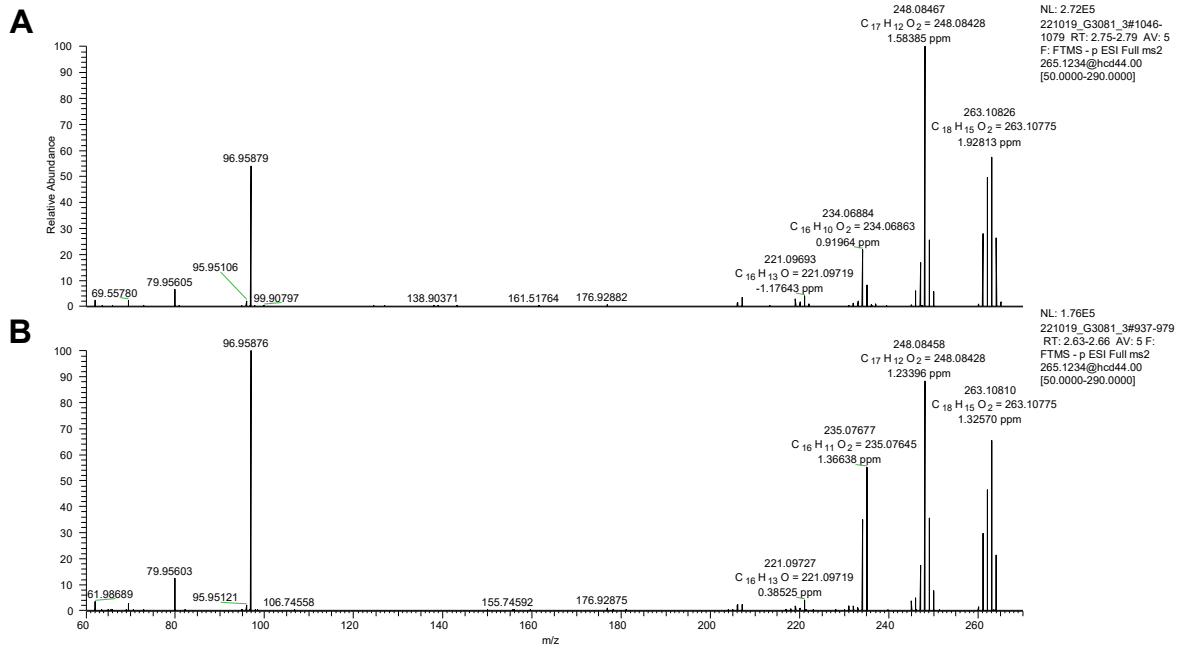

Figure S25. MS/HRMS spectrum of newly identified isomer (A: **I-4**, RT: 3.08 min) in the MeOH fraction of **Plant 1** compared to **Compound 5** (C, RT: 3.39 min) at 48 collision energy.

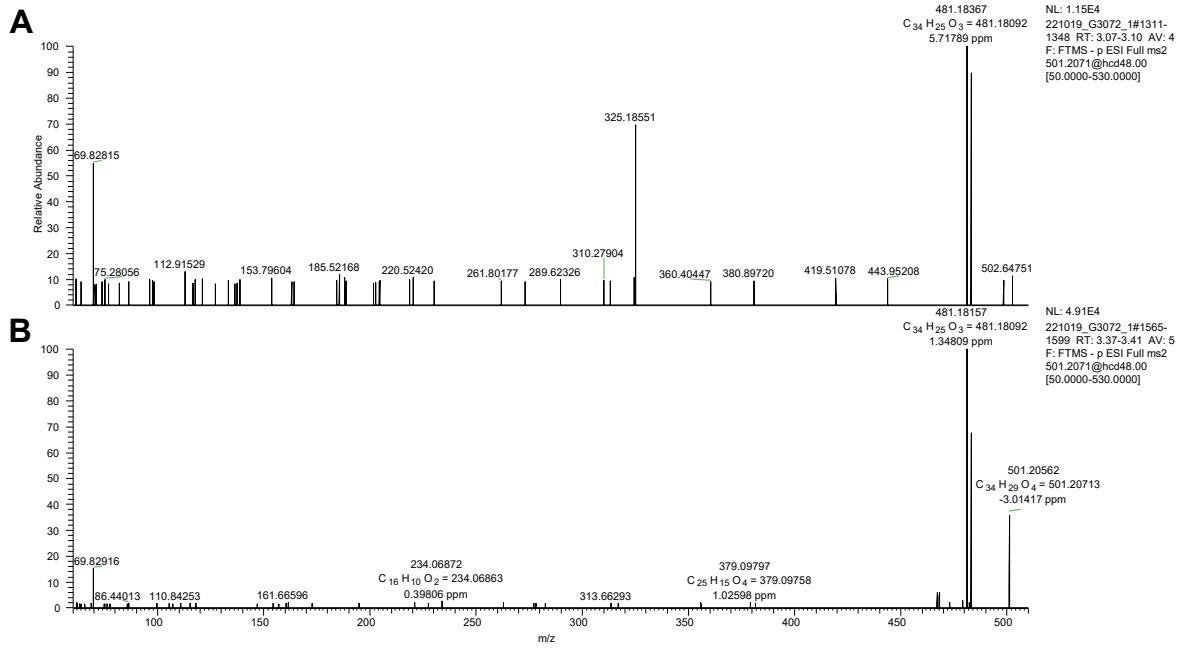

Figure S26. MS/HRMS spectra of newly identified isomers (A: **I-4**, RT: 3.08 min; B: **I-5**, RT: 3.30 min) in the CH_2Cl_2 fraction of **Plant 1** compared to **Compound 5** (C, RT: 3.39 min) at 48 collision energy.

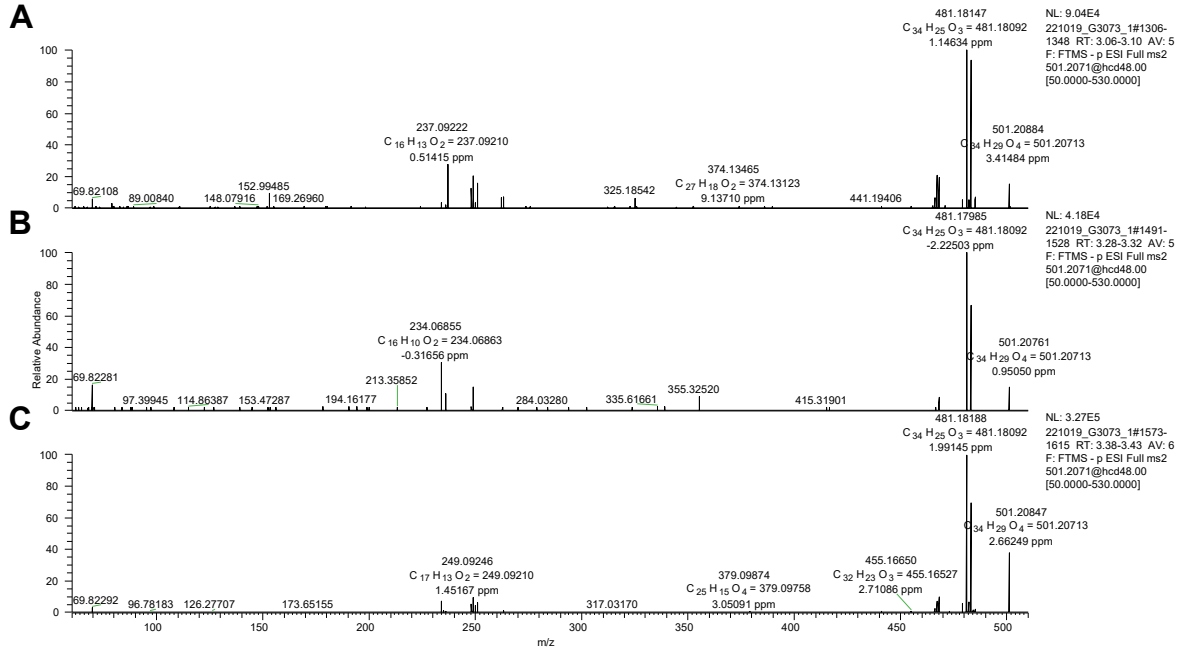

Figure S27. MS/HRMS spectra of newly identified isomers (A: **I-4**, RT: 3.08 min; B: **I-5**, RT: 3.30 min) in the CH_2Cl_2 fraction of **Plant 2** compared to **Compound 5** (C, RT: 3.39 min) at 48 collision energy.

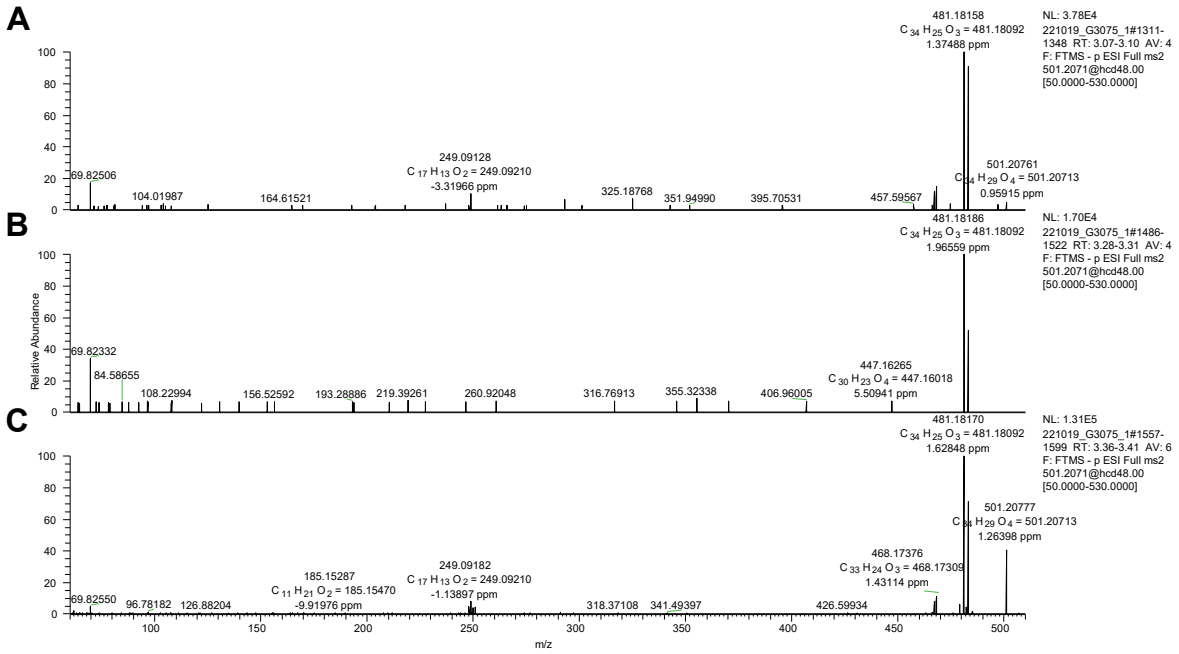

Figure S28. MS/HRMS spectrum of newly identified isomer (A: **I-4**, RT: 3.08 min) in the MeOH fraction of **Plant 3** compared to **Compound 5** (B, RT: 3.39 min) at 48 collision energy.

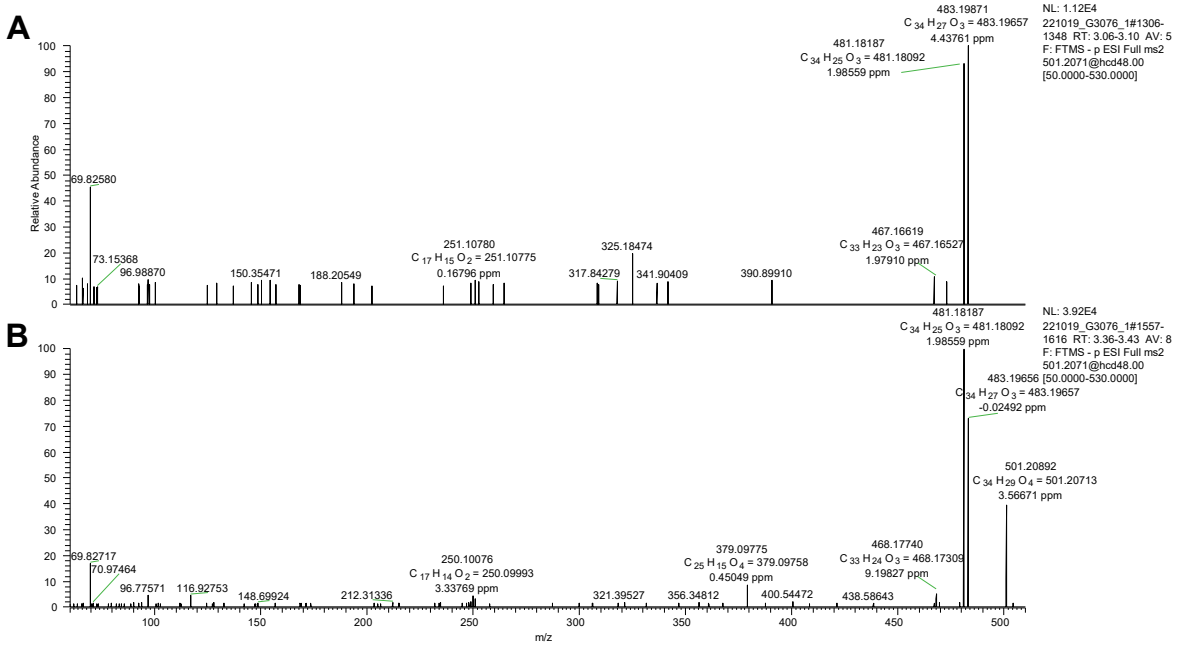

Figure S29. MS/HRMS spectra of newly identified isomers (A: **I-4**, RT: 3.08 min; B: **I-5**, RT: 3.30 min) in the CH_2Cl_2 fraction of **Plant 3** compared to **Compound 5** (C, RT: 3.39 min) at 48 collision energy.

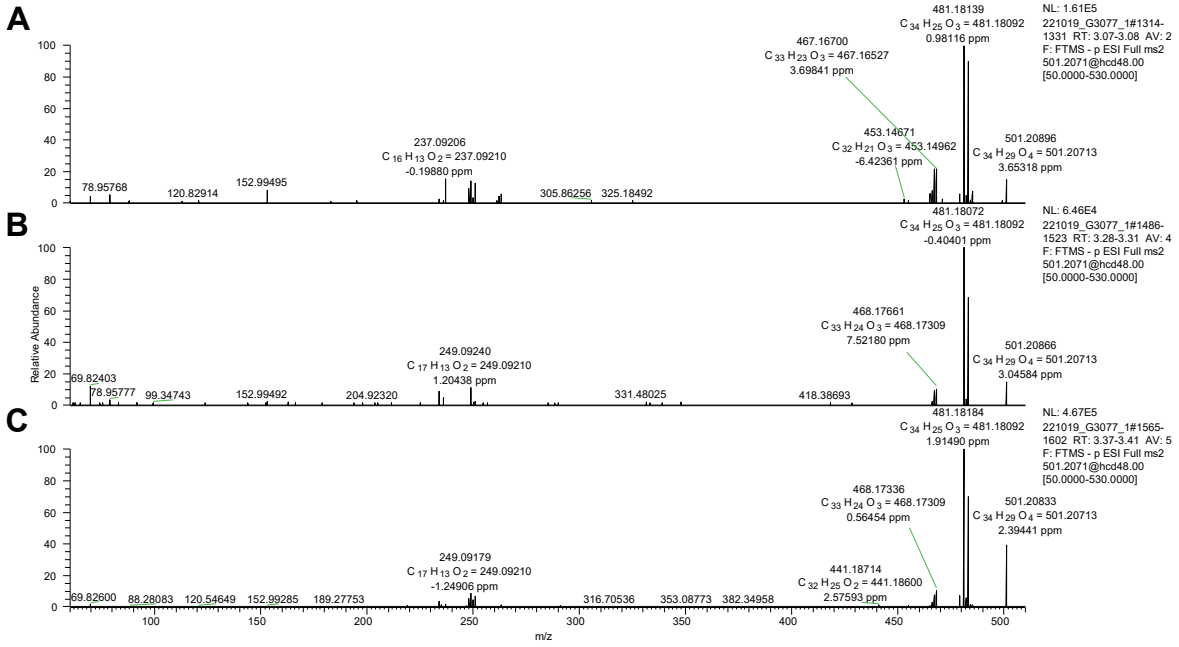

Figure S30. MS/HRMS spectra of newly identified isomers (A: **I-4**, RT: 3.08 min; B: **I-5**, RT: 3.30 min) in the CH_2Cl_2 fraction of **Plant 4** compared to **Compound 5** (C, RT: 3.39 min) at 48 collision energy.

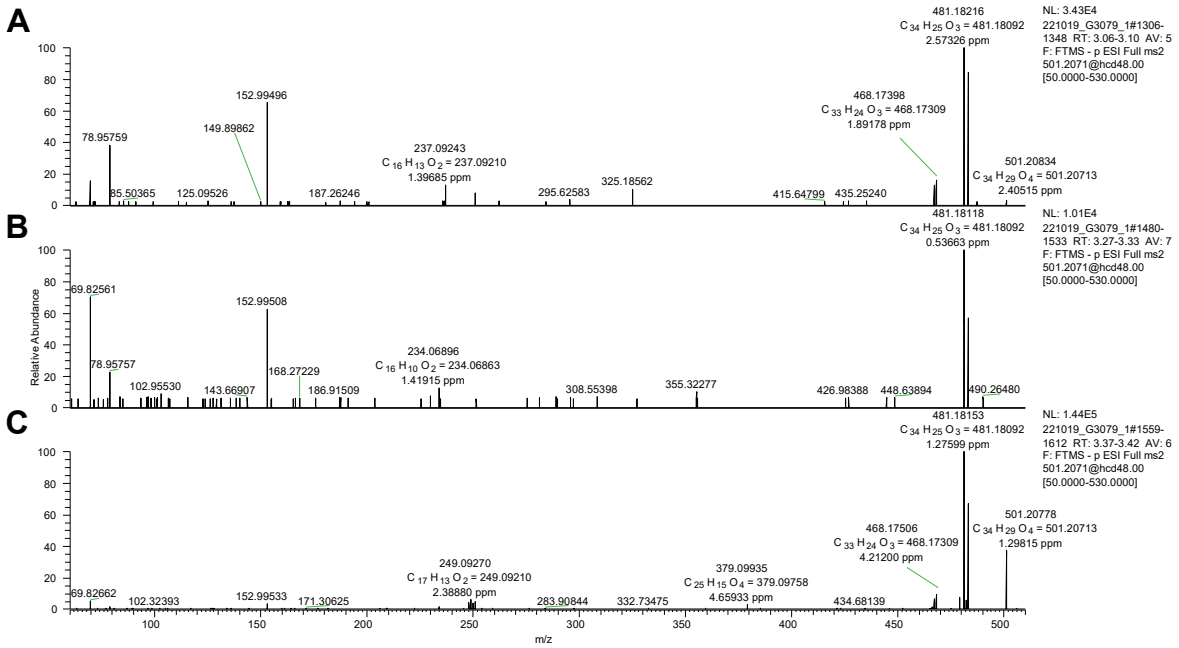

Figure S31. MS/HRMS spectra of newly identified isomers (A: **I-4**, RT: 3.08 min; B: **I-5**, RT: 3.30 min) in the CH_2Cl_2 fraction of **Plant 5** compared to **Compound 5** (C) at 48 collision energy.

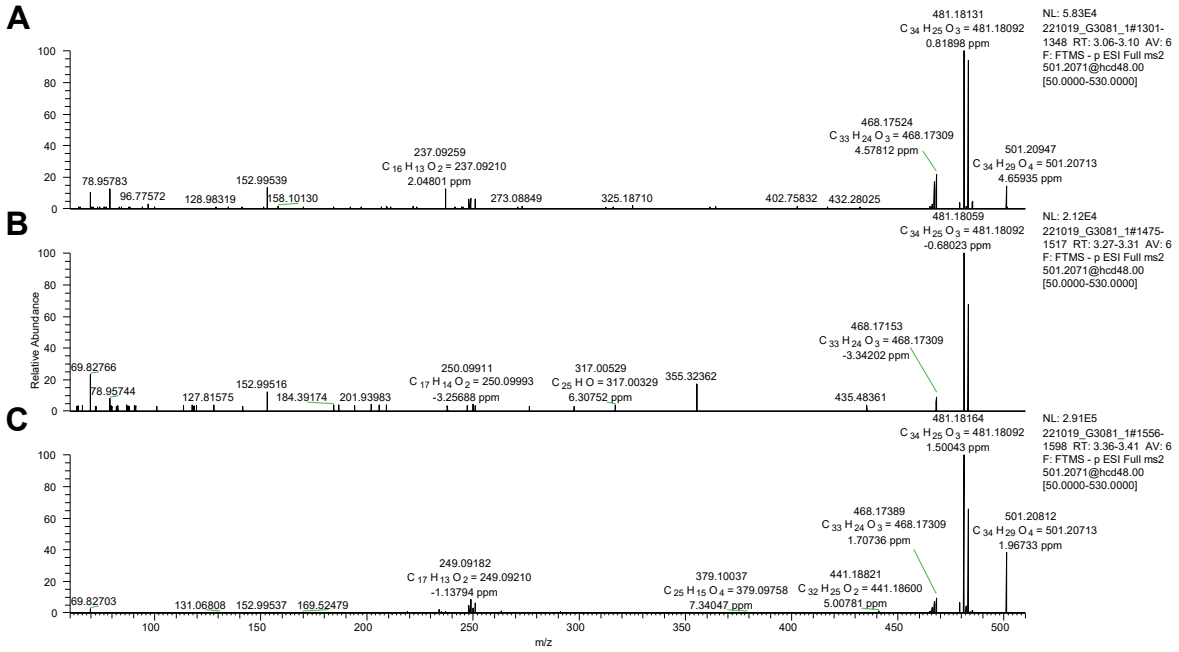

Figure S32. One-way ANOVA statistical analysis (Bonferroni's post hoc test) of phenanthrenes concentration of plant samples obtained from MeOH[1] and CH_2Cl_2[2] fractions (* P≤0.05; ** P≤0.01; ***P≤0.001